INAUGURAL-DISSERTATION

zur
Erlangung der Doktorwürde

der
Naturwissenschaftlich-Mathematischen
Gesamtfakultät

der
Ruprecht-Karls-Universität
Heidelberg

vorgelegt von

Dipl.-Phys. Johann Heinrich Bollmann

aus Bremen

Tag der mündlichen Prüfung: 4. Juli 2001

Die Kalziumempfindlichkeit der Überträgerstoff-Ausschüttung in einer glutamatergen Synapse des Zentralnervensystems

Gutachter: **Prof. Dr. Bert Sakmann**
Prof. Dr. Christoph Cremer

DISSERTATION

submitted to the
Combined Faculties for the Natural Sciences and for Mathematics

of the
Rupertus Carola University of
Heidelberg, Germany
for the degree of
Doctor of Natural Sciences

Calcium sensitivity of neurotransmitter release in a glutamatergic synapse of the central nervous system

presented by

Diplom-Physicist Johann Heinrich Bollmann

born in Bremen/Germany

Heidelberg, July 4th, 2001

Referees: **Prof. Dr. Bert Sakmann**
Prof. Dr. Christoph Cremer

Calcium sensitivity of neurotransmitter release in a glutamatergic synapse of the central nervous system

During chemical synaptic transmission, the presynaptic action potential couples to the biochemical release process by the opening of Ca^{2+} channels and Ca^{2+}-dependent activation of a release sensor that triggers the release of transmitter. Here, the dependence of transmitter release on the intracellular Ca^{2+} concentration ($[Ca^{2+}]$) was determined in a glutamatergic calyx-type synapse in slices of the rat brainstem by UV-induced Ca^{2+} uncaging. Because of the fast speed of glutamatergic synapses, an electrophysiological setup was combined with a rapid fluorescence detection system and a short-pulsed UV laser in order to both evoke and measure uniform $[Ca^{2+}]$ elevations on a fast time scale.

A homogeneous rise in the presynaptic $[Ca^{2+}]$ to 1 µM resulted in a clearly measurable increase in release. The peak release rates depended on presynaptic $[Ca^{2+}]$ with more than the fourth power. A $[Ca^{2+}]$ jump to 30 µM or more depleted the releasable vesicle pool in less than 0.5 ms. A kinetic model was devised to quantify the release rate-$[Ca^{2+}]$ relation measured in this synapse type. A comparison with action potential evoked release in the same synapses suggested that a brief elevation of $[Ca^{2+}]$ to less than 10 µM would be sufficient to reproduce the physiological release pattern. In summary, the Ca^{2+} sensitivity of synaptic transmitter release is, at least in some synapses, higher than previously thought.

Die Kalziumempfindlichkeit der Überträgerstoff-Ausschüttung in einer glutamatergen Synapse des Zentralnervensystems

Der Signalübertragung an chemischen Synapsen liegt ein Kopplungsmechanismus zwischen dem präsynaptischen Aktionspotential und der biochemischen Überträgerstoff-Ausschüttung zu Grunde. Dabei werden Ca^{2+}-Kanäle geöffnet und ein Freisetzungssensor Ca^{2+}-abhängig aktiviert, der schließlich die Überträgerstoff-Ausschüttung auslöst. In der vorliegenden Arbeit wurde die Abhängigkeit der Überträgerstoff-Ausschüttung von der intrazellulären Ca^{2+}-Konzentration ($[Ca^{2+}]$) in einer glutamatergen kelchförmigen Synapse in Stammhirnschnitten der Ratte unter Verwendung photolytischer Ca^{2+}-Freisetzungen gemessen. Um $[Ca^{2+}]$-Sprünge auf einer Zeitskala sowohl hervorrufen als auch messen zu können, die der schnellen Übertragungsgeschwindigkeit von glutamatergen Synapsen vergleichbar ist, wurde ein elektrophysiologischer Messstand mit einem schnellen Fluoreszenzdetektor und einem UV-Kurzpulslaser ausgestattet.

Ein deutlich messbarer Anstieg der Überträgerstoff-Ausschüttung wurde bereits bei einer homogenen Erhöhung der präsynaptischen $[Ca^{2+}]$ von ca. 1 µM beobachtet. Der Spitzenwert der Freisetzungsrate wuchs mit mehr als der vierten Potenz der präsynaptischen $[Ca^{2+}]$-Amplitude. Ein $[Ca^{2+}]$-Sprung von mehr als 30 µM löste die Aktivierung aller zur Fusion unmittelbar bereitstehenden Vesikel innerhalb von 0,5 ms aus. Die in dieser Synapse beobachtete Beziehung zwischen der Freisetzungsrate und der präsynaptischen $[Ca^{2+}]$ wurde mit Hilfe eines kinetischen Modells quantitativ beschrieben. Ein Vergleich der Modellvorhersagen mit Freisetzungsraten, die in denselben Synapsen während eines Aktionspotentials gemessen worden waren, ergab, dass ein kurzer Anstieg der $[Ca^{2+}]$ auf weniger als 10 µM ausreicht, um den physiologischen Freisetzungsverlauf zu erklären. Die synaptische Überträgerstoff-Ausschüttung reagiert somit zumindest in manchen synaptischen Systemen empfindlicher auf Ca^{2+} als bisher angenommen.

Contents

1. Introduction

Emerging from the two-sided nature of electro- and biochemical neural signaling, tools from originally distinct scientific disciplines are often combined to successfully elucidate the underlying mechanisms. In the present study, a biophysical question is approached with a combination of techniques from electrophysiology, fluorescence microscopy and photochemistry. A detailed description of the methods applied is provided in chapters 2 and 3. The present study draws its motivation from a physiological framework, which shall briefly be introduced in the present chapter.

1.1 Fundamental principles of neural signal processing

The nervous system is composed of cells, which are classified into the group of excitable neurons and non-neuronal glia cells. The human brain consists of about 10^{10} - 10^{12} neurons, while the number of glia cells may be more than ten-fold larger. The network properties of nervous systems arise from the neurons' capability to receive information, to process input and to send resulting information to other neurons. This section will briefly describe the electrical and chemical processes that enable neurons to communicate within a network.

1.1.1 Electrical signaling in the neuron

1.1.1.1 *Neurons as structural and functional units of the nervous system*

Neuronal cells represent the basic structural elements of biological networks. The cell boundary is defined by a phospholipid bilayer, the plasma membrane, which hosts numerous proteins such as ion channels and transporters. Thus, a neuron is a closed system that can interact with its environment by exchange of substances, energy and information. Although neurons in the central nervous system exhibit a great morphological diversity, they generally possess similar structural features, which were initially proposed to define the preferred direction of information flow within a neuronal network. A century ago, Ramón y Cajal introduced the concept of 'dynamic polarization', in which a neuron receives electrical excitation via its finely branched dendrites and sends it to other, receiving neurons via its axon (Fig. 1.1). The sending

neuron contacts the receiving cell at specialized connections, the synapses, at which electrical excitation is transmitted either chemically or electrically (*see* section 1.1.2). The soma of the receiving cell integrates the pattern of electrical signals presented by its dendritic tree and, if a threshold is reached, generates an action potential (*see next section*), which travels along the axon and activates synapses to communicate the information to succeeding neurons.

This unidirectional model successfully describes a principal pathway of information processing in biological networks. However, later observations demanded several extensions to the early concept of neural information flow. Firstly, synaptic contacts not only exist in the classical axon-to-dendrite arrangement (*axo-dendritic*), but were found also between the axon and the soma (*axo-somatic*), the two axons (*axo-axonic*) or between the dendrites (*dendro-dendritic*) of connected cells. Moreover, neurons often form reciprocal connections, i.e. the output of the receiving cell is communicated back to the sending neuron (Fig. 1.1 b). Furthermore, the somatic action potential was shown to propagate into the dendritic tree, presenting a feedback signal to the 'receiving' elements of the cell (Stuart and Sakmann, 1994). Finally, dendrites probably function as independent integrating units of synaptic activity and may generate local regenerative signals (Larkum et al., 1999).

1.1.1.2 *Neuronal excitability: resting and action potentials*

In biological neural networks, information is encoded and communicated as changes in the membrane potential. The functional basis of potential changes are the properties of the plasma membrane, which is impermeable to ion movement in its purely lipid phase, but possesses numerous proteinaceous ion channels and ion transporters that mediate ion fluxes across the membrane. Ion channels form an aqueous pore, through which ions can diffuse passively. The pore opening may be gated by the surrounding ionic environment, by the membrane potential or by specific ligands. Transporters carry ions actively, i.e. requiring consumption of chemical energy, across the membrane and generate concentration gradients between the intra- and extracellular space. Typical concentration gradients are ($[ion]_{int}$ / $[ion]_{ext}$): 12 mM / 145 mM for Na^+, 155 mM / 4 mM for K^+, 10^{-4} mM / 1.5 mM for Ca^{2+} and 4 mM / 123 mM for Cl^- (Dudel et al., 1996). The concentration gradients give rise to passive ion transport through open ion channels. Since most of the time the permeability for K^+ is higher than for Na^+, a dynamic equilibrium state evolves that is close to the Nernst potential for the concentration gradient of K^+. This equilibrium potential is termed the resting potential and usually ranges between -60 and -90 mV in neurons.

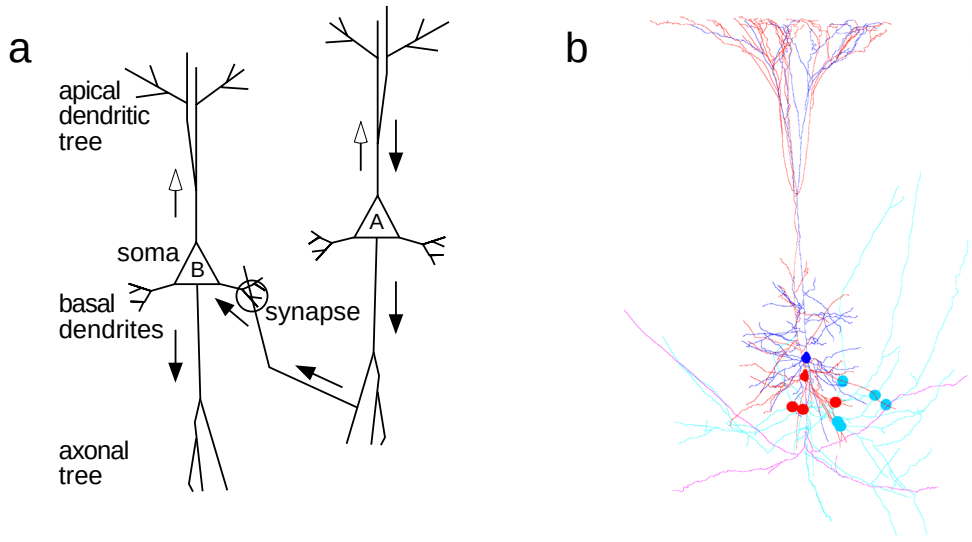

Fig. 1.1: Neural signal processing. (**a**) Schematic representation of two pyramidal neurons, connected by an axo-dendritic synapse. Preferred direction of signal propagation indicated by *solid arrows*. Input from dendrites is integrated at the soma of neuron A. Suprathreshold excitation generates an action potential, which travels along the axon and activates the synapse at the basal dendrite of neuron B. If the integrated input at the soma of neuron B exceeds a threshold, an action potential is initiated, which propagates into the axonal tree of B. Concurrently, somatic action potential initiation leads to a feedback signal in the dendritic tree, the back-propagating action potential (*open arrows*). (**b**) Light-microscopic reconstruction of two reciprocally connected pyramidal neurons (*blue and red, respectively*). Discs indicate synaptic contacts. Image kindly provided by Dr. O. Ohana.

Electrical activity in a neuron is characterized by the initiation and propagation of 'action potentials', which are stereotypic all-or-none events, being the elementary units of neuronal information processing. The action potential is generated by the self-amplifying opening of Na^+ channels if the membrane is depolarized above a threshold potential of approximately –50 mV. The membrane potential rapidly rises towards the Nernst potential for Na^+ of about +70 mV due to the increased Na^+ permeability. The rise to positive potentials peaks at ca. 40 mV and is invariably terminated by the rapid inactivation of the Na^+ channels and by the delayed opening of K^+ channels, which initiates the repolarization towards the resting potential. Neuronal action potentials typically last one millisecond or less, and the triggering of a second action potential requires the transition of inactivated Na^+ channels into the resting closed state, which may last a few milliseconds. Because of this refractory period, the rate at which neurons can 'fire' action potentials is limited to 100-1000 Hz. Generally, action potentials are triggered at the soma or axon hillock owing to its high Na^+ channel density, which admits a brief and strong depolarizing Na^+ current once the summed

synaptic potentials exceed the activation threshold. The action potential travels from the initiation site along the axon towards the nerve terminals by local membrane depolarization and Na^+ channel activation. Due to the Na^+ channel inactivation, action potentials are not reflected.

1.1.2 Synapses

Synapses are contact sites between two neurons at which electrical activity is transmitted from one neuron to the other. At a synapse, the plasma membranes of the connected neurons are separated by a narrow cleft of ca. 20 nm thickness. During synaptic transmission, the excited, 'presynaptic' neuron activates the transmission process and sends a signal to the 'postsynaptic' neuron, either in terms of a chemical transmitter substance (chemical synapse) or in terms of an ionic current through membrane spanning, conducting elements (electrical synapse).

A chemical synapse is characterized by pre- and postsynaptic membrane specializations; the presynaptic 'active zone' is a region of electron dense material close to the presynaptic membrane and contains clusters of small vesicles (30 –50 nm in diameter) filled with the transmitter substance (Fig. 1.2). Voltage-dependent Ca^{2+} channels located in or near the active zone mediate local increases in presynaptic $[Ca^{2+}]$ near the vesicles. The 'postsynaptic density' is an electron dense thickening of the postsynaptic membrane, which contains ion-permeable receptor channels that are gated by the transmitter substance.

During synaptic transmission, the presynaptic active zone is depolarized and voltage-dependent Ca^{2+} channels are opened by an incoming action potential. The resultant local $[Ca^{2+}]$ elevation triggers the fusion of vesicles with the presynaptic membrane. Transmitter released from the vesicles rapidly diffuses across the synaptic cleft and activates the opening of postsynaptic 'ionotropic' receptors, thus changing the postsynaptic permeability for selected ion species. Fast chemical transmission occurs within a time window of less than a millisecond from the arrival of the presynaptic action potential to the start of the postsynaptic electrical response.

Chemical synapses can be excitatory or inhibitory, depending on the transmitter and postsynaptic receptor channel types. Excitatory synapses use transmitters such as acetylcholine or glutamate, which activate cation-selective receptor channels. The influx of cations (Na^+, Ca^{2+}) results in a depolarization of the postsynaptic compartment and increases the probability that the postsynaptic neuron fires an action potential. The evoked, transient depolarization is called an 'excitatory postsynaptic

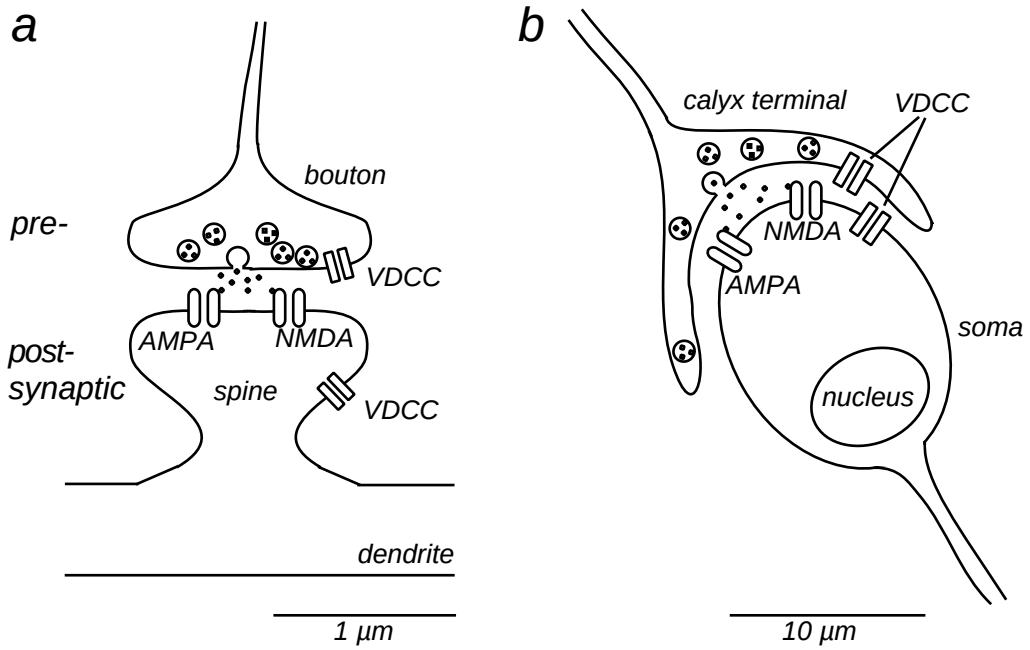

Fig. 1.2: Schematic diagram of synaptic structures. (**a**) Axo-dendritic synapse, using glutamate as excitatory transmitter. During a presynaptic action potential, voltage dependent Ca^{2+} channels (VDCC) open and admit Ca^{2+} influx in the vicinity of small synaptic vesicles, leading to vesicle fusion and release of their content. Postsynaptic glutamate receptor channels (AMPA, NMDA) open and generate an excitatory postsynaptic potential. (**b**) A calyx-type, axo-somatic synapse, approximately 10-fold larger than small synapses. The key features of glutamatergic transmission, regarding excitation-secretion coupling and postsynaptic receptor activation are conserved. Channels and vesicles not drawn to scale.

potential' (EPSP) and the underlying current an 'excitatory postsynaptic current' (EPSC). Inhibitory synapses use transmitters such as γ-amino-butyric acid (GABA) or glycine, which activate anion-selective channels. The increased permeability for Cl^- leads to a hyperpolarization of the postsynaptic compartment and/or decreases the excitability of the membrane by shunting simultaneously occurring, depolarizing currents. Evoked potential changes and underlying currents are called 'inhibitory postsynaptic potentials' (IPSPs) and 'currents' (IPSCs), respectively.

Another type of chemical transmission is mediated by 'metabotropic' receptors, which do not permit ion flux across the membrane when bound to transmitter, but trigger intracellular signaling cascades by the activation of G-proteins. Their action occurs on a slower time scale and often exerts a modulatory effect on the excitability of a neuron or the transmission efficacy of a synapse (e.g. Nakanishi, 1994; Byrne and Kandel, 1996).

Electrical transmission is mediated by ‘gap junctions’, which are built of channel forming proteins (*connexins*) embedded in the apposing membrane regions of contacting neurons. Hexameric connexin complexes connect the cytoplasm of the two neurons by an ion-permeable pore, which is pH- and Ca^{2+}-sensitive. Electrical signals can propagate directly and without delay across the cell-cell border by ionic current flow through gap junctions. In particular heart muscle and smooth muscle cells are electrically coupled by gap junctions; they are also abundantly present in the central nervous system, where they participate in the synchronization of electrical activity within a cell ensemble (Draguhn et al., 1998).

The synapse investigated in this study is a large axo-somatic synapse in the medial nucleus of the trapezoid body (MNTB) in the brainstem, whose presynaptic terminal forms a large calyx-shaped structure around the postsynaptic cell body (Fig. 1.2 b). The terminal contains several hundred active zones (Sätzler, 2000) and releases glutamate from more than a hundred vesicles upon arrival of a single presynaptic action potential (Borst and Sakmann, 1996). The postsynaptic neuron contains glutamate channels of both the α-amino-3-hydroxy-5-methyl-isoxazole-4-propionic acid (AMPA) and the N-methyl-D-aspartate (NMDA) type. A single EPSC is sufficient for postsynaptic action potential initiation, and therefore ‘suprathreshold’.

1.1.3 Synaptic plasticity

The coupling strength of a chemical synapse can change depending on its previous activation pattern or the presence of neuromodulatory substances. Frequently, chemical synaptic transmission is described using Poisson or binomial statistics, in its simplest form leading to the definition of four quantities (del Castillo and Katz, 1954): Ideally, the amount of transmitter released from one vesicle evokes a postsynaptic signal, whose size is distributed normally, the mean signal corresponding to the ‘quantal size’ q. During an action potential, exactly one vesicle can fuse at a single site, the ‘release site’, with probability p. A synapse contains N such release sites with uniform release probability p. Then the ‘quantal content’ m, i.e. the number of transmitter packets (vesicles) released during one action potential, is:

$$m = N\,p \tag{1.1}$$

Short term changes in synaptic strength, which decay within several hundred milliseconds to seconds, are activity dependent and are known as facilitation, augmentation, post-tetanic potentiation (PTP) and depression. Facilitation refers to the increase in a second or later postsynaptic response compared to that evoked by a conditioning first pulse. It decays on the order of several tens to hundreds of milliseconds. Augmentation and PTP are induced by a conditioning train of stimuli

and decay with a time constant of several seconds or minutes, respectively. All forms of short term enhancement are in part dependent on presynaptic [Ca^{2+}] elevations following stimulation, called 'residual Ca^{2+}', which may act by either increasing *N* or *p*, or both. Both differences in the kinetics of the Ca^{2+} removal mechanisms and different molecular targets mediating synaptic enhancement are thought to account for the various components of increased synaptic strength. Other mechanisms can also contribute to short term enhancement, such as facilitation of presynaptic Ca^{2+} channels or an activity-dependent relief of postsynaptic AMPA receptors from a polyamine block (*reviewed by* Zucker, 1999). Another form of short term plasticity is synaptic depression, i.e. a decrease in quantal content after repetitive stimulation that usually recovers with time constants of hundreds of milliseconds to several seconds. A likely mechanism is the depletion of fusion-competent vesicles available at the active zone, corresponding to a reduction in *N* in Eq. 1.1, due to previous release. Alternatively, activation of presynaptic metabotropic receptors or a mechanism that changes the Ca^{2+} sensitivity of the release machinery during prolonged exposure to elevated [Ca^{2+}] ('adaptation') may lead to a reduction in *p* or *N* (Nakanishi, 1994; Hsu et al., 1996). Other mechanisms include desensitization of postsynaptic transmitter receptors and depletion of Ca^{2+} in the synaptic cleft (Trussell et al., 1993; Borst and Sakmann, 1999a). Taken together, short term plasticity is often shaped by multiple mechanisms, which may dominate different temporal phases of the observed changes in synaptic strength.

Aside from short term changes, many synapses in the central nervous system exhibit an activity-dependent increase or decrease in synaptic efficacy lasting hours or days (*reviewed by* Bliss and Collingridge, 1993). Depending on the direction of change, they are called long term potentiation (LTP) and long term depression (LTD). While LTP can be induced by high frequency stimulation (for example, a few pulses at 100 Hz, repeated several times), LTD is induced by sustained low frequency stimulation (1 – 20 Hz). Alternatively, pairing protocols have been used in hippocampal and neocortical connections, where paired pre- and postsynaptic action potentials evoke LTP or LTD, when the postsynaptic action potential succeeds or precedes the presynaptic action potential, respectively (Magee and Johnston, 1997; Markram et al., 1997). Currently, no simple model is able to predict the various forms of LTP/LTD induction found in different synapses suggesting that multiple mechanisms are involved. However, since both long term effects are often found to depend on the degree of postsynaptic [Ca^{2+}] elevation, it is thought that LTP induction requires [Ca^{2+}] to rise above a higher threshold than that imposed by the mechanisms of LTD induction (Bear, 1995). The postsynaptic rise in [Ca^{2+}] can be mediated by NMDA receptor channels, voltage dependent Ca^{2+} channels or intracellular Ca^{2+} stores and is

modulated by postsynaptic membrane depolarization. The NMDA receptor channel represents an ideal substrate for coincidence detection of pre- and postsynaptic activity, because it permits appreciable Ca^{2+} influx only when it is activated by glutamate released from the presynaptic terminal and a simultaneous relief from Mg^{2+} block by postsynaptic depolarization (Mayer et al., 1984; Nowak et al., 1984).

The capability of pairing protocols to induce LTP/LTD implies that these forms of plasticity may encode persistent information on coincident activity in a neural network. In turn, a shift of synaptic weights driven by coincident activity is the key mechanism suggested by Hebb (1949) to form the basis of learning. Meanwhile, several genetic studies were performed, in which long term plasticity was manipulated and its possible role in learning was analyzed in behavioral tasks (recent studies are, e.g., Tang et al., 1999; Zamanillo et al., 1999). Because interfering with an isolated mechanism may be masked or compensated by other processes in the living animal, it is difficult at present to assign well-defined functions to LTP/LTD in learning and the formation of memory. Thus, intense research currently focuses on evaluating the significance of LTP and LTD in behavior.

1.2 Exo- and endocytosis

1.2.1 Vesicle cycling

A presynaptic terminal is specialized to release transmitter substances with precise timing and at high rates. This is achieved by storage of the transmitter in small packages, the synaptic vesicles, which can fuse with the membrane shortly after a presynaptic action potential. Presynaptic terminals have developed membrane trafficking mechanisms to maintain the supply of vesicles in a release-ready state.

A general model of vesicle cycling in the presynaptic terminal is depicted in Fig. 1.3 (Südhof, 1995; Augustine et al., 1999). In the resting terminal, at least two functional pools of synaptic vesicles can be distinguished (Greengard et al., 1993): (1) a set of vesicles is found in contact with the presynaptic membrane at the active zone, which is regarded as the pool of vesicles readily releasable upon arrival of an action potential. The morphologically docked vesicles found in electron micrographs can be sub-divided into ‘docked only’ and ‘docked and primed’ vesicles, depending on whether they have passed through all molecular priming steps necessary for Ca^{2+}-triggered fusion (Südhof, 1995, *see below*). (2) Vesicles are observed to form clusters near the active zone, which are stabilized probably because of the binding of the

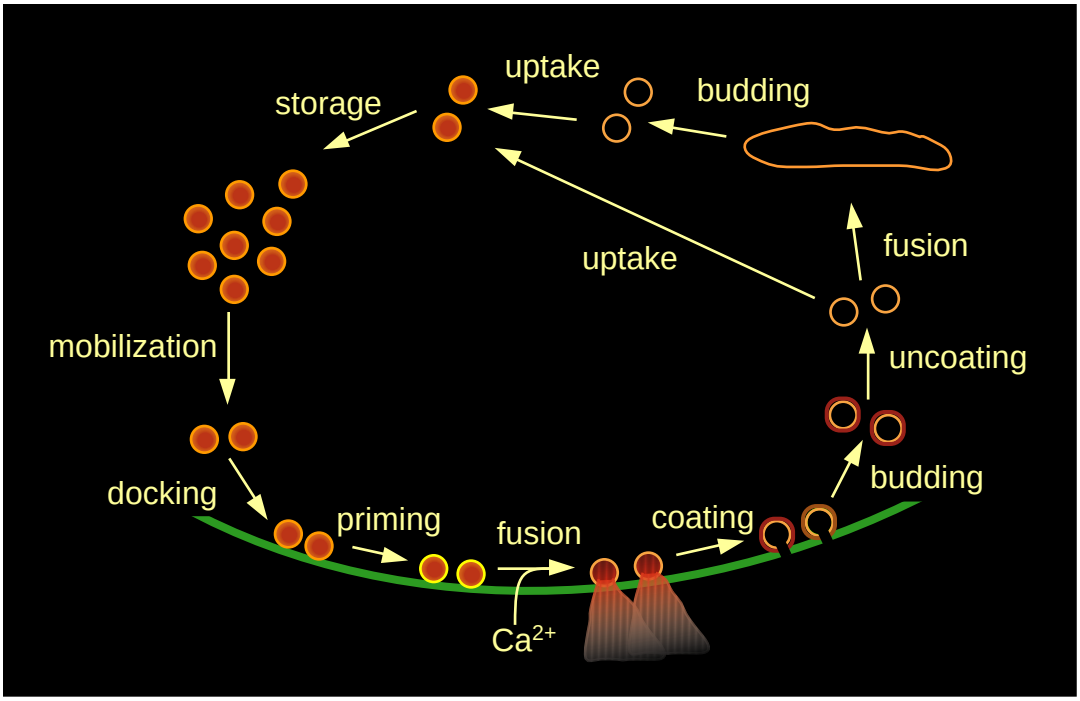

Fig. 1.3: The synaptic vesicle cycle. Before fusing with the presynaptic membrane, synaptic vesicles have to be translocated to and brought into close apposition with the presynaptic membrane (*mobilization* and *docking*). Further molecular reactions (*priming*) are required until a vesicle can undergo Ca^{2+}-triggered fusion. Vesicular membrane is recycled after coating with clathrin (*coating*, *budding*, *uncoating*). Endocytosed vesicles may transit by fusion and budding through intracellular endosomes and are added to the reserve pool (*storage*). Recycled vesicles are refilled with neurotransmitter by active transport (*uptake*) (modified from Augustine et al., 1999).

vesicle protein synapsin I with cyto-skeletal elements (Pieribone et al., 1995). Vesicles from this ‘reserve pool’ are translocated to the active zone and repopulate empty release sites during repetitive stimulation (e.g. Zenisek et al., 2000). After fusion and transmitter release, clathrin-coated membrane segments bud from the presynaptic membrane and form vesicles that are thought to be translocated into the reserve pool, possibly after fusion with and budding from intracellular endosomes (Heuser and Reese, 1973, *see* section 1.2.3 for an alternative model). During this cycling, vesicles accumulate neurotransmitter by active transport, which is driven by an electrochemical gradient due to a proton pump. Many steps of synaptic vesicle cycling can be associated with specific molecular reactions by disrupting the cycle at different stages. Useful tools are microinjection of peptides or antibodies or genetic manipulations that interfere with one of the putative molecular reactions (Pieribone et

al., 1995; Südhof, 1995; Augustine et al., 1999). To clarify the role of the numerous types of presynaptic proteins is still difficult and is the focus of current research. The following sections will briefly introduce more detailed concepts that have been proposed for the key events during synaptic transmission.

1.2.2 Exocytosis

1.2.2.1 *Some molecules involved in exocytosis*

Chemical transmission requires the precisely timed release of transmitter molecules into the synaptic cleft by the specific fusion of synaptic vesicles with the presynaptic membrane. The abundance of intracellular membrane in the terminal necessitates that this signaling process be highly regulated by specific biochemical binding partners on the vesicle and the target membrane. The vesicular and target membrane contain numerous proteins, of which well characterized super-families are the GTP-binding Rab proteins and the soluble NSF attachment protein receptor (SNARE) proteins (Südhof, 1995). While both protein families may contribute to vesicle transport specificity and target membrane recognition, the SNARE proteins are thought to be important also in mediating the last steps of membrane fusion (Jahn and Südhof, 1999; Chen and Scheller, 2001) The vesicular (v-) SNARE protein synaptobrevin and the target membrane (t-) SNARE proteins SNAP-25 and syntaxin can form a tight complex, the SNARE core complex, which is likely to play a functional role in vesicle targeting to the release site and/or fusion of the two lipid bilayers. In this complex, synaptobrevin and syntaxin both contribute one and SNAP-25 contributes two α-helical domains, which bind by forming a four-stranded coiled-coil structure. Because syntaxin and synaptobrevin bind in parallel fashion, i.e. with the amino termini at one end and the membrane-anchored carboxy termini at the other end of the core complex, it is thought that the binding reaction between SNARE proteins may occur in a ‘zipper-like’ fashion, thus exerting mechanical force on the lipid membrane anchors. The core complex is heat stable up to 90° C and resistant to protease digestion, biochemical denaturation and cleavage by clostridial neurotoxins, which are able to cut SNARE proteins in the isolated state (Chen and Scheller, 2001). In biological systems, SNARE complexes are disassembled by *N*-ethyl-maleimide-sensitive fusion protein (NSF) and soluble NSF attachment protein (α-SNAP) under hydrolysis of ATP. This reaction is thought to reactivate previously used SNARE proteins for a new fusion cycle.

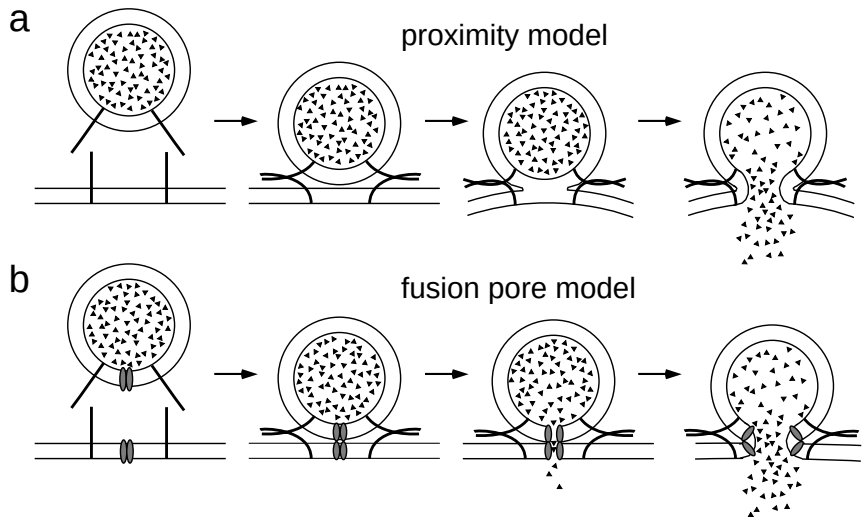

Fig. 1.4: Models of lipid membrane fusion in exocytosis. (**a**) In the 'proximity' model, fusion is induced, when the vesicle and presynaptic membrane are forced into close apposition by the tight binding of v- and t-SNAREs in a zipper-like manner. A precursor state of the fully fused membranes may be 'hemifusion' (3rd step in a), where the inner membrane leaflets have mixed, but the outer leaflets are intact. (**b**) In the 'fusion pore' model, the mixing of vesicle and presynaptic membrane lipids is mediated by a proteinaceous channel connecting both membranes. Binding of v- and t-SNAREs may anchor vesicles to the target membrane and promote the formation of fusion pore precursors.

1.2.2.2 *The fusion mechanism*

The fusion mechanism itself requires that two closely apposed phospholipid bilayers merge in an aqueous environment. Because of the repulsive forces between the polar phospholipid head groups, a high energy barrier must be overcome, which is thought to be mediated by specialized fusion proteins. Two principal hypotheses have been put forward to describe the fusion reaction of the transmitter vesicle with the target membrane mechanistically (Fig. 1.4). In 'proximity' models it is proposed that the action of membrane proteins such as SNARE complexes is restricted to reducing the activation energy by forcing the two lipid bilayers into close apposition, from where lipids of the two proximal leaflets can mix and form a hemifusion or stalk state (Fig. 1.4 a). It is unclear whether the hemifused state is immediately followed by the break down and mixing of the distal leaflets, or whether this state is metastable, requiring another catalyzing step for full fusion to occur (Jahn and Südhof, 1999; Chen and Scheller, 2001). In the 'fusion pore model', the fusion of apposing membranes is mediated by a proteinaceous channel structure that spans both membranes and promotes the mixing of the two lipid bilayers (Almers and Tse, 1990). This could possibly involve radial expansion of the fusion protein's subunits within the lipid bilayers, allowing the phospholipids to flow and mix in the expanding space between

the subunits. As an example, a membrane spanning, proteolipidic sector of the vacuolar H^+-ATPase in yeast, a proton pump molecule, was recently shown to form *trans*-complexes between apposing intracellular membranes and to mediate fusion (Peters et al., 2001), the latter in the absence of SNARE core complexes. Thus, the role of various molecular interactions in fusion is still controversial and it remains to be elucidated to what extent the mechanisms driving membrane fusion are molecularly conserved in different cells and species.

1.2.3 Endocytosis

Synaptic terminal membrane is recycled during and after transmitter release by local infolding of the membrane and subsequent budding of small vesicles and/or larger compartments called cisternae (*reviewed by* Wilkinson and Cole, 2001). This way, the increase in terminal surface area due to exocytosis is quickly compensated, which is necessary to maintain the supply of membrane material for the formation of new vesicles and to prevent terminal deformation. Based on electron microscopic studies, two alternative recycling pathways were proposed, which differed in several aspects. In one model, fused vesicles are thought to collapse completely into the presynaptic membrane. Membrane retrieval occurs away from the release site and involves specific membrane recognition mediated by the protein adaptor complex AP2, which triggers the coating and infolding of the membrane segment mediated by clathrin (Pearse et al., 2000). Clathrin-coated vesicles pinch off and subsequently discard the coating; then they are transferred to the reserve pool of vesicles (Heuser and Reese, 1973; Südhof, 1995). In a second model, the fusion of a vesicle is thought to be reversible, leaving the vesicle membrane largely intact and allowing it to reseal and detach from the release site quickly after pore opening and transmitter discharge (‘kiss and run’, Ceccarelli et al., 1973; Fesce et al., 1994). The proposed mechanism does not require clathrin-mediated endocytosis and makes recycled vesicles available close to the release site, which could be advantageous to counteract rapid depletion of the releasable vesicle pool during repetitive stimulation.

Recent experiments using fluorescent membrane markers with different departitioning properties suggest that at least two endocytotic pathways, which resemble those proposed originally, may be at work in synaptic terminals. Thus, endocytosis via the formation of cisternae may serve to supply newly assembled vesicles to the reserve pool on a slow time scale, whereas a rapid endocytotic pathway near the active zone may be capable of locally recycling or reusing vesicles previously located in the readily releasable pool (Pyle et al., 2000; Richards et al., 2000; Stevens and Williams, 2000).

1.2.4 The role of Ca^{2+} in exocytosis and endocytosis

In the exocytotic event sequence, vesicles are arrested in a primed state at the release site. Only after opening of Ca^{2+} channels in response to a nerve pulse does a rise of the intracellular Ca^{2+} concentration trigger the final steps of transmitter release (Katz, 1969). In early experiments it was shown by varying the extracellular [Ca^{2+}] that transmitter release is controlled by the cooperative action of several Ca^{2+} ions (Dodge Jr. and Rahamimoff, 1967). Later, measurements of the dependence of transmitter release on intracellular [Ca^{2+}] confirmed that at least three Ca^{2+} ions are required to trigger the fusion of a vesicle, thus providing the release mechanism with a supra-linear sensitivity to variations in [Ca^{2+}] (Heinemann et al., 1994; Heidelberger et al., 1994). Despite considerable effort, the mechanism by which Ca^{2+} deploys the fusion machinery is still under debate. Many Ca^{2+}-binding proteins present in presynaptic terminals have a modulating function in transmitter release (Burgoyne and Morgan, 1998). The most prominent candidate for a neuronal Ca^{2+} sensor for transmitter release is synaptotagmin I, which binds to phospholipids and syntaxin and oligomerizes in a Ca^{2+}-dependent manner. Neurons in which synaptotagmin was absent or point mutated showed reduced synchronous transmitter release (Nonet et al., 1993; Broadie et al., 1994; Geppert et al., 1994; Fernández-Chacón et al., 2001). However, a widely accepted functional model of synaptotagmin-triggered fusion has not yet emerged.

Aside from being the crucial signal for rapid membrane fusion, Ca^{2+} is likely to regulate also other steps in the synaptic vesicle cycle. Increased [Ca^{2+}] following stimulation may enhance the rate at which the readily releasable pool is replenished (*reviewed by* Zucker, 1999; *but see* Wu and Borst, 1999). It has been observed in non-neural exocytosis that even the expansion rate of a granular fusion pore may be a function of intracellular [Ca^{2+}] (Hartmann and Lindau, 1995). Also endocytosis is regulated by Ca^{2+} in many systems, although the exact dependence is not generally established (Henkel and Almers, 1996). Thus it was observed that rapid endocytosis in endocrine cells is initiated by Ca^{2+} binding to calmodulin (Artalejo et al., 1996). In hippocampal synapses, intracellular [Ca^{2+}] was observed to up-regulate endocytosis (Sankaranarayanan and Ryan, 2001). In contrast, in synaptic terminals of retinal bipolar cells, increased [Ca^{2+}] levels appeared to inhibit endocytosis (von Gersdorff and Matthews, 1994).

It can be summarized that many processes in the synaptic vesicle cycle are subject to Ca^{2+}-sensitive modulation, implying that the balanced operation of this cycle requires tight regulation of intracellular [Ca^{2+}] levels.

1.3 Motivation

The speed of chemical transmission is limited by the time the final steps of exocytosis require for completion after arrival of a presynaptic action potential. These steps include the opening of presynaptic Ca^{2+} channels, Ca^{2+} diffusion to and activation of the Ca^{2+} sensor for release and ultimately the fusion of the vesicle and target membrane. The activation of the release sensor by Ca^{2+} is of particular interest because it represents the very relay mechanism by which electrical activity – the flow of ions across the membrane – is coupled to chemical signal transmission – the discharge of chemical transmitter molecules from a fused vesicle. Therefore, the temporal coupling precision will be a main determinant of the synchronicity of pre- and postsynaptic excitation. As mentioned above, synchronicity and coincidence detection are important for the activity-dependent adjustment of synaptic weights, which is considered a possible mechanism for the way a biological network processes and stores information. In addition, the Ca^{2+}-release sensor reaction not only partially determines the fidelity of chemical transmission, but may also be a target where the adjustment of synaptic weights can be implemented. When restricting the view on this element of the signaling cascade, two basic regulatory mechanisms may be considered. First, the Ca^{2+} signal observed by the Ca^{2+} sensor during an action potential may be activity-dependent, for instance due to action potential broadening or modulation of Ca^{2+} channel opening. Second, the efficacy of the Ca^{2+} sensor to bind Ca^{2+} and trigger fusion – its sensitivity - may be regulated in an activity-dependent manner.

To better understand the significance of excitation-secretion coupling for transmission fidelity and synaptic plasticity, the general dependence of the process of transmitter release on intracellular [Ca^{2+}] should be determined first. Because of its importance, several investigations have focussed on this issue in other exocytotic systems, for example in hormone releasing cells or in specialized nerve terminals, however with divergent findings that apparently cannot be extrapolated to other synapses (*see* section 5.3.3 for a more detailed discussion).

In this study, the Ca^{2+} dependence of rapid synaptic transmission was characterized in a glutamatergic giant synapse in rat brainstem slices, using pre- and postsynaptic current recordings (Forsythe, 1994; Borst et al., 1995). Because of the large size of the pre- and postsynaptic compartment, electrical signals can be detected from both compartments using the whole-cell patch clamp technique. In this method, a recording pipette is tightly sealed to a patch of cell membrane, permitting low resistance access to the intracellular compartment for electrical measurements and diffusional delivery of substances (Neher and Sakmann, 1976; Hamill et al., 1981; Edwards et al., 1989).

A UV-sensitive Ca^{2+} chelator loaded with Ca^{2+} was introduced to the presynaptic terminal together with a fluorescent Ca^{2+} indicator (Kaplan and Somlyo, 1989). The presynaptic [Ca^{2+}] was artificially raised by brief UV laser pulses and measured using quantitative fluorescence microscopy. By simultaneously measuring the postsynaptic currents, the relation between presynaptic glutamate release and intracellular [Ca^{2+}], in other words the 'Ca^{2+} sensitivity of transmitter release', could be determined for this mammalian synapse. Furthermore, this relation was described in a quantitative model, which was subsequently used to estimate the Ca^{2+} signal triggering synaptic transmission during physiological activity.

2. Theory

2.1 Intracellular Ca^{2+} dynamics

Calcium is probably the most versatile signal transduction element in living cells. It controls diverse cell functions, of which the fastest are excitation-secretion coupling in synapses and excitation-contraction coupling in muscle cells, both occurring within milliseconds. On a time scale of minutes or longer, Ca^{2+} is a main regulator of cell cycling, gene expression and programmed cell death (Clapham, 1995). In general, cells maintain intracellular [Ca^{2+}] at a level ~10^4-fold lower than the extracellular level. Furthermore, cells must precisely control local and global [Ca^{2+}] signals in order to maintain a high specificity when using a single ion type as a quasi-universal messenger.

In a more abstract view, cells can be regarded as a finite, three-dimensional space delimited by a closed surface, the plasma membrane, and compartmentalized into different spatial and functional units. In this volume, the Ca^{2+} concentration is a function of space and time, [Ca^{2+}](**r**,*t*). The dynamic evolution of [Ca^{2+}](**r**,*t*) depends on three regulatory mechanisms: passive diffusion, chemical reaction and active transport. In living cells, all three processes exist and contribute to shaping [Ca^{2+}](**r**,*t*).

The first one, diffusion in an aqueous medium, naturally occurs wherever electrochemical gradients are encountered. Thus, Ca^{2+} diffusion occurs along the electrochemical gradient over the plasma membrane through Ca^{2+}-permeable channel proteins, giving rise to localized Ca^{2+} influx. Intracellular diffusion of Ca^{2+} within the cytosol is influenced by diffusional barriers, which contribute to shaping local Ca^{2+} signals. One example for this compartmentalization of Ca^{2+} signaling is the restriction of [Ca^{2+}] elevations during synaptic activation to a postsynaptic compartment, the 'synaptic spine': the parent dendrite is largely spared from the Ca^{2+} signal because of the narrower spine neck, forming a bottle-neck for Ca^{2+} diffusion (Yuste and Denk, 1995).

In the second mechanism, Ca^{2+} can bind to mobile or immobile proteins in a chemical reaction, which is generally termed 'Ca^{2+} buffering'. This mechanism largely contributes to maintaining low global [Ca^{2+}] levels and to confining [Ca^{2+}] elevations to the vicinity of their sources. To date, a large number of Ca^{2+}-binding proteins have been found, of which prominent neuronal members are calbindin, calretinin and

parvalbumin (Blaustein, 1988). Ca^{2+} buffering reactions are usually described using second order reaction rate equations (*see next section*).

A third mechanism is the active transport of Ca^{2+} 'uphill', against the electrochemical gradient under consumption of chemical energy. This mechanism is responsible for the sequestration of Ca^{2+} across the plasma membrane into the extracellular space and for the uptake of Ca^{2+} into intracellular stores, such as mitochondria or the endoplasmic reticulum. The active transport is taken over by membrane-integral proteins, e.g. the Ca^{2+}-ATPase or the Na^{+}-Ca^{2+} exchanger.

Under the combined influence of numerous interactions of the above type, a complex spatio-temporal pattern of intracellular $[Ca^{2+}]$ is expected to evolve, especially whenever cellular activity perturbs the electrochemical equilibrium. A special case important for neuronal exocytosis is the rapid opening of Ca^{2+} channels during action potentials which generates highly localized and short-lived $[Ca^{2+}]$ elevations close to synaptic vesicles at the presynaptic membrane (*reviewed by* Neher, 1998). These so-called 'Ca^{2+} microdomains' have been difficult to measure directly, mostly because light microscopy lacks the spatial resolution. However, spatially and temporally confined $[Ca^{2+}]$ elevations which probably arise from the opening of a cluster of several channels have been observed (Llinás et al., 1992; DiGregorio et al., 1999; Yazejian et al., 2000).

On the other hand, mathematical simulations have given much insight into the complex distribution of $[Ca^{2+}](\mathbf{r},t)$, especially during channel opening at synaptic sites (Chad and Eckert, 1984; Simon and Llinás, 1985; Pape et al., 1995; Naraghi and Neher, 1997; *reviewed by* Neher, 1998). The modeled $[Ca^{2+}](\mathbf{r},t)$, however, is quite sensitive to the kinetic properties of the buffer species present in the vicinity of the Ca^{2+} channels. For synapses, only little information is currently available regarding the buffers' identity, nor is much known about the spatial arrangement of Ca^{2+} channels, buffers and vesicles (*but see* Harlow et al., 2001).

Therefore, in the present study a different approach was used to analyze the dependence of a cellular process on $[Ca^{2+}](\mathbf{r},t)$. By uniform uncaging of Ca^{2+} throughout the presynaptic terminal, the spatial dependence of $[Ca^{2+}](\mathbf{r},t)$ was removed (Fig. 2.1). By choosing a short-pulsed UV source and a rapidly converting Ca^{2+} cage and fast Ca^{2+} indicators, also the temporal dependence of $[Ca^{2+}](\mathbf{r},t)$ was largely reduced to a brief transition period of 100-200 µs.

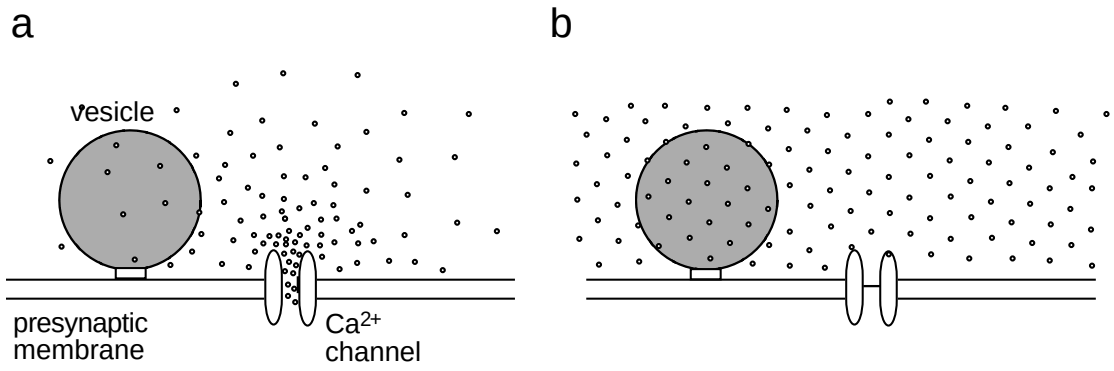

Fig. 2.1: Spatial pattern of $[Ca^{2+}]$ during Ca^{2+} influx and UV-induced Ca^{2+} uncaging. (**a**) The opening of a Ca^{2+} channel in the presynaptic plasma membrane mediates the influx of Ca^{2+} ions. The concentration profile and the location of vesicles relative to the Ca^{2+} channels is generally not known, making it difficult to predict the $[Ca^{2+}]$ present at the Ca^{2+} sensor during action potential-evoked release. (**b**) UV-induced photolysis of a high-affinity Ca^{2+} chelator permits spatially homogeneous $[Ca^{2+}]$ elevations. Volume-averaged $[Ca^{2+}]$ measurements then reflect the $[Ca^{2+}]$ at the Ca^{2+} sensor for release.

In the following, the general approach to model Ca^{2+} dynamics will be stated based on the three regulatory mechanisms mentioned above. A simple approximation is considered for a single channel Ca^{2+} domain in order to illustrate the effect of Ca^{2+} buffers on the spatial extent of the microdomain. Finally, the time course of $[Ca^{2+}](t)$ evoked by Ca^{2+} uncaging will be calculated using a detailed model, which takes into account those Ca^{2+} buffers also present in the experiments.

2.1.1 Time-dependent Ca^{2+} diffusion-reaction in an aqueous medium

Firstly, diffusion of Ca^{2+} and Ca^{2+} buffering molecules is described by Fick's law, if we assume the intracellular volume to be an isopotential space.

$$\frac{\partial[Ca^{2+}](\mathbf{r},t)}{\partial t} = D_{Ca}\,\Delta[Ca^{2+}](\mathbf{r},t), \tag{2.1}$$

where Δ is the Laplace operator and D_{Ca} the diffusion coefficient of Ca^{2+}, which also may be a function of space and time. The same applies for the Ca^{2+} buffers present.

Secondly, the buffering reactions are commonly described with 2nd order reaction rate equations. The rate of concentration changes during a buffer reaction between Ca^{2+} and a buffer B_1:

$$Ca + B_1 \underset{k_{-1}}{\overset{k_1}{\longleftrightarrow}} CaB_1 \tag{2.2}$$

is proportional to the reactants' concentrations, with association and dissociation rate constants k_1, k_{-1}:

$$\begin{aligned}\frac{d[\mathrm{Ca}^{2+}]}{dt} &= -k_1[\mathrm{Ca}^{2+}][\mathrm{B}_1] + k_{-1}[\mathrm{CaB}_1] \\ \frac{d[\mathrm{CaB}_1]}{dt} &= k_1[\mathrm{Ca}^{2+}][\mathrm{B}_1] - k_{-1}[\mathrm{CaB}_1]\end{aligned} \tag{2.3}$$

Thirdly, the action of active transport mechanisms cannot be represented in a general form, but it is dependent on chemical energy supply and local $[Ca^{2+}]$. The transport rate p can often be approximated using a Michaelis-Menten relation, which accounts for the limited transport capacity at saturating $[Ca^{2+}]$:

$$p([\mathrm{Ca}^{2+}],\mathbf{r},t) = p_{\max}(\mathbf{r},t)\frac{[\mathrm{Ca}^{2+}](\mathbf{r},t)}{([\mathrm{Ca}^{2+}](\mathbf{r},t) + K_{\mathrm{m}})} \ , \tag{2.4}$$

where p_{max} is the maximal pump rate in a given volume element, and K_m is the $[Ca^{2+}]$ where p becomes half-maximal.

By combining these mechanisms in the most general form, the spatio-temporal evolution of $[Ca^{2+}](\mathbf{r},t)$ can be described by a system of partial differential equations:

$$\frac{\partial[\mathrm{CaB}_i]}{\partial t} = k_i[\mathrm{Ca}^{2+}][\mathrm{B}_i] - k_{-i}[\mathrm{CaB}_i] + D_{\mathrm{CaB}_i}\Delta[\mathrm{CaB}_i] \ , \tag{2.5}$$

$$\frac{\partial[\mathrm{B}_i]}{\partial t} = -k_i[\mathrm{Ca}^{2+}][\mathrm{B}_i] + k_{-i}[\mathrm{CaB}_i] + D_{\mathrm{B}_i}\Delta[\mathrm{B}_i] \ , \tag{2.6}$$

$$\begin{aligned}\frac{\partial[\mathrm{Ca}^{2+}]}{\partial t} = &-\sum_i^n (k_i[\mathrm{Ca}^{2+}][\mathrm{B}_i] - k_{-i}[\mathrm{CaB}_i]) + D_{\mathrm{Ca}}\Delta[\mathrm{Ca}^{2+}] \\ &+ j([\mathrm{Ca}^{2+}],\mathbf{r},t) - p([\mathrm{Ca}^{2+}],\mathbf{r},t)\end{aligned} \tag{2.7}$$

Here, B_i denotes n different Ca^{2+} buffer species with association and dissociation rate constants k_i and k_{-i}, respectively. Ca^{2+} influx is summarized as j, which depends on both passive transport through ion channels and active transport, e.g. the Na^+-Ca^{2+} exchanger operating in reverse mode (Regehr, 1997). Furthermore, p comprises the various Ca^{2+} sequestration mechanisms.

In general, this set of partial differential equations cannot be solved analytically. For different spatial arrangements and buffer conditions, $[Ca^{2+}](\mathbf{r},t)$ has been calculated numerically (e.g. Simon and Llinás, 1985; Yamada and Zucker, 1992; Roberts, 1994). In parallel, the evolution of $[Ca^{2+}](\mathbf{r},t)$ can be approximated analytically for some limiting cases, for example, when the concentration of the buffer in its free and Ca^{2+}-bound form is assumed to be constant (Neher, 1986), when Ca^{2+} binding is assumed to

be instantaneous ('rapid buffer approximation', Smith, 1996) or when the change in free buffer concentration is small during a perturbation ('linearized buffer approximation', Pape et al., 1995; Naraghi and Neher, 1997).

2.1.2 Ca^{2+} microdomains

Numerical and analytical solutions of $[Ca^{2+}](\mathbf{r},t)$ show that increases in $[Ca^{2+}]$ are defined locally around the site of Ca^{2+} influx and drop sharply with distance from the channel. To illustrate this point, Ca^{2+} influx through a single channel is treated as a point source in an infinite plane, corresponding to the molar flux Φ (in units $mol.s^{-1}$) into a semi-infinite medium (Fig. 2.2 a). It is convenient to use spherical coordinates and first consider the development of the steady-state solution in the absence of Ca^{2+} buffering and extrusion. Eq. 2.5 - 2.7 reduce to a radial diffusion equation:

$$\frac{\partial[Ca^{2+}]}{\partial t} = D_{Ca}\left(\frac{\partial^2[Ca^{2+}]}{\partial r^2} + \frac{2}{r}\frac{\partial[Ca^{2+}]}{\partial r}\right). \tag{2.8}$$

Assuming that the $[Ca^{2+}]$ is zero prior to channel opening, which occurs at $t = 0$, and Φ is constant thereafter, the solution to Eq. 2.8 is given by (Crank, 1975):

$$[Ca^{2+}](r,t) = \frac{\Phi}{4\pi D_{Ca} r}\,\mathrm{erfc}\left(\frac{r}{2\sqrt{D_{Ca}t}}\right). \tag{2.9}$$

Two characteristics of Ca^{2+} microdomains can readily be understood from this equation. Firstly, if a channel is continuously open, a microdomain will reach a steady-state profile, since the error function erfc will approach unity for large t. With a value for D_{Ca} = 220 $\mu m^2\ s^{-1}$ (Naraghi and Neher, 1997), steady-state will be established in a range of 10-100 nm from the channel within ~10 µs to ~1 ms. Secondly, assuming a single channel current of i_{Ca} = 0.2 pA, (corresponding to a flux $\Phi = i_{Ca}/F \approx 2\times10^{-18}$ $mol.s^{-1}$; F Faraday's constant), the steady-state $[Ca^{2+}]$ in the immediate vicinity of a channel (≤ 10 nm) can reach 70 µM or more and drops with a 1/r-dependence (Fig. 2.2 b). This already emphasizes the local nature of Ca^{2+} microdomains.

Ca^{2+} buffers decrease the range of $[Ca^{2+}]$ even further and reduce the size of microdomains. If it is assumed that Ca^{2+} buffering near a Ca^{2+} channel is dominated by a single buffer B_1 present in large concentrations, the buffered diffusion of Ca^{2+} can be modeled in a simplified scheme, which formally corresponds to the cable equation (Neher, 1986):

$$\frac{\partial[Ca^{2+}]}{\partial t} = -k_1^{app}[Ca^{2+}] + k_{-1}^{app} + D_{Ca}\left(\frac{\partial^2[Ca^{2+}]}{\partial r^2} + \frac{2}{r}\frac{\partial[Ca^{2+}]}{\partial r}\right). \tag{2.10}$$

In this approximation, it is assumed that the concentrations of the free and Ca^{2+}-bound buffer are constant and can therefore be incorporated in the apparent rate constants $k_1^{app} = k_1 [B_1]$ and $k_{-1}^{app} = k_{-1} [CaB_1]$. The steady-state solution of this differential equation is given by:

$$\Delta[Ca^{2+}](r,t) = \frac{\Phi}{4\pi D_{Ca} r} \exp(-r/\lambda_B) \quad , \tag{2.11}$$

where λ_B is determined by the buffer association rate constant k_1, its concentration $[B_1]$, and the Ca^{2+} diffusion coefficient D_{Ca}:

$$\lambda_B = \sqrt{D_{Ca} / k_1 [B_1]}. \tag{2.12}$$

λ_B corresponds to the mean radial distance Ca^{2+} can diffuse away from the channel before it is bound by the buffer. It is useful to note that the exponential term in equation (2.11) predicts a sharper decay of the Ca^{2+} microdomain than equation (2.9) at steady-state in the absence of Ca^{2+} buffers, when moving away from the Ca^{2+} channel.

In many synapses, the dependence of transmitter release on added buffers with different length constants λ_B was investigated to estimate the distance between Ca^{2+} channels and the sites of transmitter release (Adler et al., 1991; Borst and Sakmann, 1996; Ohana and Sakmann, 1998). Fig. 2.2 b shows the predicted effect of two Ca^{2+} buffers, EGTA and BAPTA, which have similar affinity ($K_D \sim 200$ nM), but different association rate constants ($k_{1, EGTA} = 2.5 \times 10^6$ M^{-1} s^{-1}, $k_{1, BAPTA} = 4 \times 10^8$ M^{-1} s^{-1}; Naraghi and Neher, 1997). Because EGTA can significantly reduce free $[Ca^{2+}]$ only after several tens or hundreds of nanometers (Fig. 2.2 b), inhibition of transmitter release by the relatively ineffective EGTA supports the view that Ca^{2+} channels and release sites are not tightly co-localized. Inhibition of release by EGTA varies in different preparations, which may indicate that there are a variety of synaptic arrangements between Ca^{2+} channels and release sites (*see* section 5.3.3).

This section introduced the concept of Ca^{2+} microdomains in the simplified case of single channel domains in the absence of buffer saturation. The analysis becomes more complicated when the overlap of Ca^{2+} domains of several channels and the effect of local depletion of free Ca^{2+} buffers is to be considered (Naraghi and Neher, 1997; Neher, 1998).

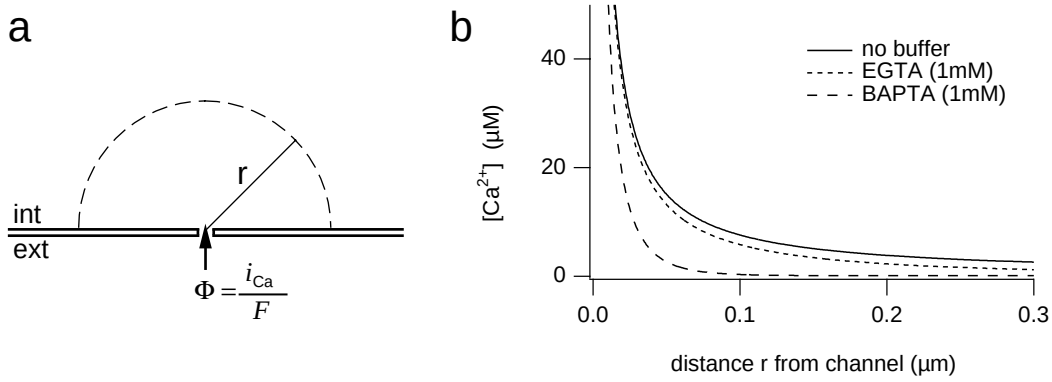

Fig. 2.2: Steady state $[Ca^{2+}]$ profile near a single Ca^{2+} channel in the presence of different Ca^{2+} buffers. (**a**) Ca^{2+} influx through a single channel is treated as diffusion from a point source into a semi-infinite space (*see text*). (**b**) The free $[Ca^{2+}]$ drops with the buffer length constant λ_B of the Ca^{2+} buffer. Single channel Ca^{2+} domains are confined to, at most, a few hundred nanometers from the source. Endogenous Ca^{2+} buffers (not taken into account in this approximation) are likely to further reduce the spatial extent of the Ca^{2+} domain.

2.1.3 Simulation of laser-induced $[Ca^{2+}]$ jumps

To circumvent the uncertainties of local Ca^{2+} domains, spatially homogeneous Ca^{2+} uncaging was used in this study to characterize the Ca^{2+} sensitivity of glutamate release. This permitted calculation of the temporal evolution of $[Ca^{2+}]$ in the absence of concentration gradients, which largely simplifies the theoretical description.

The temporal evolution of $[Ca^{2+}](t)$ was calculated by numerically solving a set of differential equations derived from the scheme in Fig. 2.3. A simplified scheme is shown in Fig. 2.3 a, where a fraction α of the cage DM-nitrophen (DM) is instantaneously excited to the intermediate state DM^* at time t_0, and is converted to the low affinity photoproduct (DMp) at the rate $k_{p,1}$. The only other Ca^{2+} buffer present is the Ca^{2+}-sensitive dye (D). At all times, the buffers bind and unbind Ca^{2+} at the rates k_i (i = 1, 2, 4, 9), finally reaching a new equilibrium.

In the experiments, however, Ca^{2+} is also bound by other buffers. Furthermore, DM-nitrophen exhibits a considerable affinity for Mg^{2+}. Finally, absorption measurements of the decay of DM-nitrophen intermediates revealed a double-exponential decay (Ellis-Davies et al., 1996), and measurements of the $[Ca^{2+}]$ time course following laser photolysis showed a fast and a slow component of $[Ca^{2+}]$ increase. Therefore, the simple model was extended to account for these conditions (Fig. 2.3 b). Here, the binding of buffers to both Ca^{2+} (left column in b) and Mg^{2+} (right column in b) was taken into account. The solutions used in this study contained ATP and phosphocreatine (PC), which also bind Ca^{2+} and Mg^{2+} (Fabiato and Fabiato, 1979).

Furthermore, cells contain endogenous buffers (EB), which can be included in this scheme once they are kinetically characterized. The photolysis reaction of DM-nitrophen is divided into two decay pathways, where the photolyzed fraction α is subdivided into a fast and a slowly decaying fraction, β_1 and β_2 = 1-β_1, respectively, which, at $t = t_0$, form the excited intermediate states DM1* and DM2*, respectively. DM1* and DM2* decay at different rates $k_{p,1}$ and $k_{p,2}$ to the low affinity states DM1p and DM2p, respectively. Both states have the same, low affinity for Ca^{2+}, but DM2p was modeled to have 100-fold slower association and dissociation rate constants, $k_{5,Ca}$, $k_{-5,Ca}$, than DM1p, which largely improved the overlay of measured and predicted $[Ca^{2+}](t)$ on a longer time scale (*see* Fig. 4.2). Finally, all buffers interact simultaneously with Ca^{2+} and Mg^{2+}, as indicated by the pairs of horizontal arrows.

For the reader's convenience, the set of differential equations is given in expanded form below. Buffers not affected by the UV pulse obey the simple buffer reaction equation (Eq. 2.3). These are non-photolyzed DM-nitrophen (i = 1), ATP (i = 6), phosphocreatine (i = 7), the endogenous buffer (i = 8) and the indicator (i = 9):

$$\frac{d[B_i]}{dt} = -k_{i,Ca}[B_i][Ca^{2+}] + k_{-i,Ca}[CaB_i] - k_{i,Mg}[B_i][Mg^{2+}] + k_{-i,Mg}[MgB_i] \quad (2.13)$$

$$\frac{d[CaB_i]}{dt} = +k_{i,Ca}[B_i][Ca^{2+}] - k_{-i,Ca}[CaB_i] \quad (2.14)$$

$$\frac{d[MgB_i]}{dt} = +k_{i,Mg}[B_i][Mg^{2+}] - k_{-i,Mg}[MgB_i] \ , \quad (2.15)$$

where $k_{\pm i,Ca}$ and $k_{\pm i,Mg}$ denote the association and dissociation rate constants for Ca^{2+} and Mg^{2+}, respectively. The excited cage species DMj* (j = 1, 2) in their free and cation-bound form decay at rates $k_{p,j}$, and interact with Ca^{2+} and Mg^{2+} at rates $k_{\pm i,Ca/Mg}$ (i = 2, 3):

$$\frac{d[DMj^*]}{dt} = -k_{i,Ca}[DMj^*][Ca^{2+}] + k_{-i,Ca}[CaDMj^*] - k_{i,Mg}[DMj^*][Mg^{2+}] + k_{-i,Mg}[MgDMj^*] - k_{p,j}[DMj^*] \quad (2.16)$$

$$\frac{d[CaDMj^*]}{dt} = +k_{i,Ca}[DMj^*][Ca^{2+}] - k_{-i,Ca}[CaDMj^*] - k_{p,j}[CaDMj^*] \quad (2.17)$$

$$\frac{d[MgDMj^*]}{dt} = +k_{i,Mg}[DMj^*][Mg^{2+}] - k_{-i,Mg}[MgDMj^*] - k_{p,j}[MgDMj^*]. \quad (2.18)$$

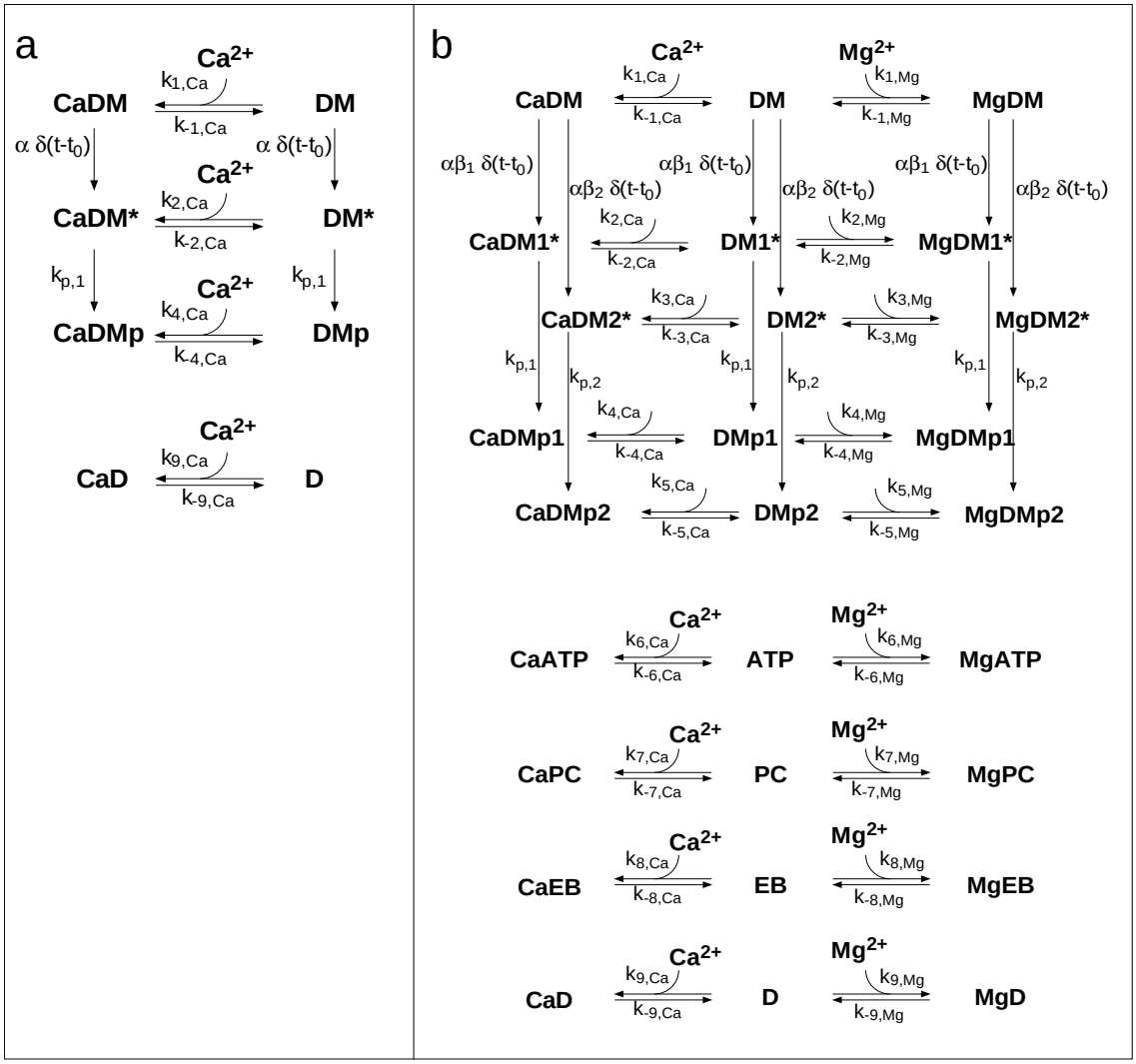

Fig. 2.3: Reaction scheme of buffered Ca^{2+} uncaging. (**a**) Simple model of Ca^{2+} uncaging and buffering in the presence of DM-nitrophen (DM), DM-nitrophen photoproducts (DMp) and the Ca^{2+} indicator (D). (**b**) Refined model of [Ca^{2+}] dynamics which includes the presence of ATP, phosphocreatine (PC) and an endogenous buffer (EB) and Mg^{2+} as a second divalent ion species that is chelated by DM-nitrophen. In addition, the conversion of excited DM-nitrophen (DM^*) proceeds along two pathways with different rate constants $k_{p,1}$ and $k_{p,2}$. The resulting photoproducts DMp1 and DMp2 have the same affinity for Ca^{2+}, but DMp2 has a 100-fold slower dissociation rate constant. This accounts for the slow component of Ca^{2+} uncaging found in photolysis experiments in vitro.

They are converted to the low affinity photoproducts DMpj, where a free intermediate DMj^* is cleaved into two identical photoproduct molecules, whereas a cation-bound intermediate results in one free and one cation-bound photoproduct molecule (reaction rate constants are $k_{\pm i,Ca/Mg}$, i = 4, 5):

$$\frac{d[\mathrm{DMpj}]}{dt} = -k_{\mathrm{i,Ca}}[\mathrm{DMpj}][\mathrm{Ca}^{2+}] + k_{\mathrm{-i,Ca}}[\mathrm{CaDMpj}] - k_{\mathrm{i,Mg}}[\mathrm{DMpj}][\mathrm{Mg}^{2+}] + k_{\mathrm{-i,Mg}}[\mathrm{MgDMpj}] + 2\,k_{\mathrm{p,j}}[\mathrm{DMj}^{*}] + k_{\mathrm{p,j}}[\mathrm{CaDMj}^{*}] + k_{\mathrm{p,j}}[\mathrm{MgDMj}^{*}] \quad (2.19)$$

$$\frac{d[\mathrm{CaDMpj}]}{dt} = +k_{\mathrm{i,Ca}}[\mathrm{DMpj}][\mathrm{Ca}^{2+}] - k_{\mathrm{-i,Ca}}[\mathrm{CaDMpj}] + k_{\mathrm{p,j}}[\mathrm{CaDMj}^{*}] \quad (2.20)$$

$$\frac{d[\mathrm{MgDMpj}]}{dt} = +k_{\mathrm{i,Mg}}[\mathrm{DMpj}][\mathrm{Mg}^{2+}] - k_{\mathrm{-i,Mg}}[\mathrm{MgDMpj}] + k_{\mathrm{p,j}}[\mathrm{MgDMj}^{*}]. \quad (2.21)$$

Finally, the concentrations of free divalent cations, $[Ca^{2+}]$ and $[Mg^{2+}]$, obey simple reaction kinetics, determined by the rate constants of all buffers, B_i, including the cage intermediates (i = 2, 3) and the photoproducts (i = 4, 5):

$$\frac{d[\mathrm{Ca}^{2+}]}{dt} = \sum_{\mathrm{i}=1}^{9}\left\{-k_{\mathrm{i,Ca}}[\mathrm{B_i}][\mathrm{Ca}^{2+}] + k_{\mathrm{-i,Ca}}[\mathrm{CaB_i}]\right\} \quad (2.22)$$

$$\frac{d[\mathrm{Mg}^{2+}]}{dt} = \sum_{\mathrm{i}=1}^{9}\left\{-k_{\mathrm{i,Mg}}[\mathrm{B_i}][\mathrm{Mg}^{2+}] + k_{\mathrm{-i,Mg}}[\mathrm{MgB_i}]\right\}. \quad (2.23)$$

Initial conditions were determined by calculating the equilibrium concentrations of all reactants under the assumption that DM-nitrophen is initially present only in its high affinity form (DM). This was done by solving the set of equations given by the law of mass action:

$$[\mathrm{Ca}^{2+}][\mathrm{B_i}] = [\mathrm{Ca}^{2+}]([\mathrm{B_i}]_{\mathrm{tot}} - [\mathrm{CaB_i}] - [\mathrm{MgB_i}]) = K_{\mathrm{D,i,Ca}}[\mathrm{CaB_i}] \quad (2.24)$$

$$[\mathrm{Mg}^{2+}][\mathrm{B_i}] = [\mathrm{Mg}^{2+}]([\mathrm{B_i}]_{\mathrm{tot}} - [\mathrm{CaB_i}] - [\mathrm{MgB_i}]) = K_{\mathrm{D,i,Mg}}[\mathrm{MgB_i}] \quad (2.25)$$

$$[\mathrm{Ca}^{2+}]_{\mathrm{tot}} - [\mathrm{Ca}^{2+}] - \sum_{\mathrm{i}}[\mathrm{CaB_i}] = 0 \quad (2.26)$$

$$[\mathrm{Mg}^{2+}]_{\mathrm{tot}} - [\mathrm{Mg}^{2+}] - \sum_{\mathrm{i}}[\mathrm{MgB_i}] = 0 \quad , \quad (2.27)$$

where $[X]_{tot}$ denotes the total concentration of species X, and $K_{D,i,Ca/Mg}$ denotes the dissociation constant of buffer B_i, given by $K_{D,i,Ca/Mg} = k_{-i,Ca/Mg}/k_{i,Ca/Mg}$ for Ca^{2+} and Mg^{2+}, respectively. The intermediates DMj* (j = 1, 2), present at time zero as a fraction $\alpha\,\beta_j$ of $[DM]_{tot}$, were modeled to have the same rate constants as intact DM-nitrophen ($k_{\pm 2,Ca/Mg} = k_{\pm 3,Ca/Mg} = k_{\pm 1,Ca/Mg}$). The perturbation of the system was modeled by allowing DMj* to decay to the photoproduct, beginning at time zero.

Rate constants used for the calculation of $[Ca^{2+}](t)$ were taken from the literature. For some buffers, only dissociation constants were available, but not the kinetically important rate constants. This was the case for Ca^{2+} and Mg^{2+} binding to PC. In that

case, rate constants were chosen to be very slow, such that the buffer had no effect on the rapidly changing time course of $[Ca^{2+}]$ at the beginning of the perturbation. When no interaction was expected, e.g. for binding of Mg^{2+} to Fura-2-FF (Xu-Friedman and Regehr, 1999), the respective K_D was adjusted to 1 M. The choice of Ca^{2+} cages and buffers is discussed in greater detail in section 3.4.2, together with the applicable kinetic constants.

2.2 Fluorescence

Ionic concentrations in small cellular compartments are often measured using fluorescent indicators, which change their fluorescent properties when bound to the ionic species of interest. How these fluorescence changes are related to concentration changes is the subject of a later section (3.4.1). Here, the fundamental concept of fluorescence will briefly be described.

Fluorescent indicators possess 'chromophores', i.e. groups of atoms within the indicator molecule, which can absorb a photon, leading to electronic state excitation (Atkins, 1990). The absorption bands depend on the energy gaps between the ground state and the possible excited states of the group's electronic system, which are influenced by the rest of the molecule. In Fig. 2.4, the potential energy of a diatomic molecule in the ground state and different excited electronic states is diagrammed as a function of the internuclear distance. According to the Franck-Condon-principle, absorption of a photon induces a 'vertical transition' of the molecule into an excited state, i.e. the transition occurs without a rearrangement of the massive nuclei of the system, which react to the new electron density distribution and relax to the new equilibrium distance only after the transition. Vibrational and rotational states cause a spread of the energy levels within a given electronic state, which usually causes broad bands in the absorption spectrum of the molecule rather than sharp spectral lines (*see* e.g. Fig. 3.3). The absorption probability is proportional to the square of the transition dipole moment μ of the chromophoric group, which is determined by the wave functions of the initial and final state of the system, $|\varphi_i\rangle$ and $|\varphi_f\rangle$, respectively: $\mu = -e \langle\varphi_f|\mathbf{r}|\varphi_i\rangle$, where $\mathbf{r}$ represents the electronic coordinates. In the Born-Oppenheimer approximation, in which the electrons move in the quasi-static electric field of the massive nuclei, the complete wave function is the product of the electronic and vibrational wave functions: $|\varphi_i\rangle = |\varphi_{i,e}\rangle\,|\varphi_{i,v}\rangle$. Therefore, $\mu = -e \langle\varphi_{f,e}|\mathbf{r}|\varphi_{i,e}\rangle\langle\varphi_{f,v}|\varphi_{i,v}\rangle$. Because of the second factor, the system is most likely excited into that vibrational

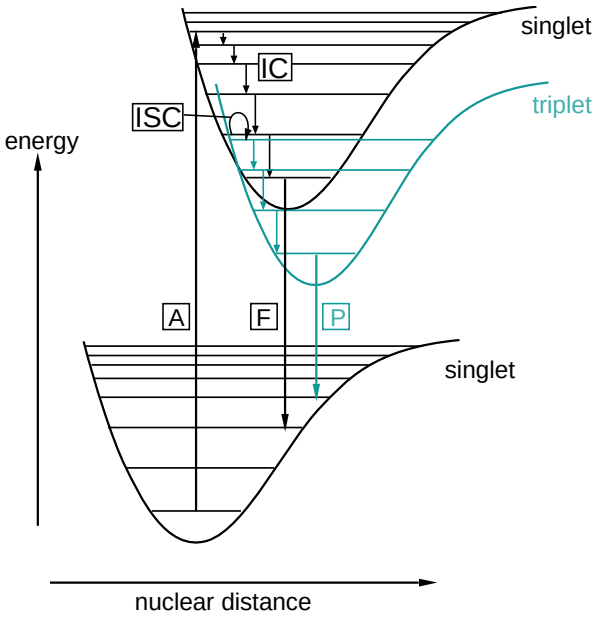

Fig. 2.4: Decay mechanisms of a diatomic molecule after optical excitation. After absorption of a photon (A) the chromophore undergoes a singlet→singlet state transition. After non-radiant, internal conversion (IC), it can decay to the ground state under emission of a fluorescence photon (F). Alternatively, a forbidden transition to the meta-stable triplet state can occur (intersystem crossing, ISC). Further de-excitation can occur via emission of a photon (phosphorescence) or a change in the molecule's conformation (photochemical reaction, photo-bleaching, *not shown*).

sub-state of a given electronic state, that exhibits the largest overlap with the initial vibrational level of the ground state and which is usually above the lowest vibrational level of the excited electronic state.

The de-excitation of a chromophore occurs along mechanistically different channels. Firstly, energy is dissipated by non-radiant, *internal conversion* (IC, Fig. 2.4). This means that, within the excited electronic state, the system cascades towards the lowest vibrational and rotational level by collisional interaction with its molecular environment ('thermal decay'). Secondly, a vertical transition to the electronic ground state can then occur by spontaneous emission of a photon. Since the radiant transition usually occurs after thermal decay within the excited electronic state, the emitted photon has a lower energy than the absorbed photon, which results in a shift of the emission spectrum relative to the absorption spectrum towards longer wavelengths (*Stokes shift*). This de-excitation is called 'fluorescence', and it is characterized by a lifetime of a few nanoseconds of the lowest vibrational level of the first excited state.

De-excitation from the excited singlet state to the ground state also occurs by other mechanisms, such as non-radiant thermal decay or 'phosphorescence'. In the latter case, the chromophore undergoes a forbidden transition from the excited singlet state into the triplet state (*intersystem crossing*, ISC, Fig 2.4), which has a non-zero probability, for example because of spin orbit coupling of the electrons' magnetic moments. After internal conversion within the triplet state, a radiant transition from the triplet to the singlet state cannot be mediated solely by emission of a photon, and therefore the triplet state has a considerably longer lifetime of $>10^{-8}$ seconds than the first excited singlet state.

The fluorescence quantum efficiency η of a chromophore is given by the ratio of fluorescence photons N_F emitted by a molecule over the number of photons absorbed N_A. This is determined by the relative probability of the different decay pathways of an excited chromophore. Thus:

$$\eta = \frac{N_F}{N_A} = \frac{k_F}{k_F + \Sigma\, k_i} \quad , \tag{2.28}$$

where k_F is the rate constant of fluorescent decay of the first excited singlet state, and the k_i's are the rate constants of decay via parallel, non-fluorescent decay mechanisms such as thermal decay, intersystem crossing into the triplet state or photo-activated, chemical reaction.

In a later section (3.4.1), it is assumed that the fluorescence intensity is proportional to the concentrations of the bound and unbound form of a Ca^{2+} indicator, respectively. The validity of this assumption will be discussed in the following:

The number of emitted photons F recorded per unit time from a fluorescence indicator is proportional to the number of photons I_{abs} absorbed per unit time, the quantum efficiency η of the indicator and the collection efficiency C of the optical setup, which is the product of several loss factors that account for the incomplete coverage of the solid angle by the objective lens, for reflection and absorption of collected photons at the various optical components as well as for the conversion efficiency of the photodetector. Lambert-Beer's law specifies the amount of attenuation when light of intensity I_0 passes through a layer of thickness l of homogeneously distributed absorbers:

$$I_{abs} = I_0(1-10^{-\varepsilon l c}) = I_0(1-e^{-2.303\varepsilon l c}) \approx 2.303\, I_0 \varepsilon l c \quad , \tag{2.29}$$

where ε is the molar extinction coefficient of the absorbing species and c its concentration. The right side of the equation is the first order approximation after Taylor expansion of the exponential function. In the present study, Ca^{2+} indicators were used with molar extinction coefficients of ~25,000 M^{-1} cm^{-1} at a concentration of 1 mM, and the dye-filled structures had a cross section of not more than 20 µm along the optical axis. Omitting the higher order terms of the Taylor expansion therefore results in an error of ≤ 6%. With this approximation, the collected fluorescence signal can be written as:

$$F = \eta\, C\, I_{abs} \approx 2.303\, \eta\, C\, I_0 \varepsilon\, l\, c. \tag{2.30}$$

If the time-independent factors η, C, I_0, ε and l are combined to a single proportionality constant S, and the Ca^{2+}-bound and free form of the indicator are treated as independent species, the individual fluorescent signals can be written in the simple form:

$F_D = S_D\, c_D$ and $F_{CaD} = S_{CaD}\, c_{CaD}$, where the index D denotes the Ca^{2+}-free and the index CaD denotes the Ca^{2+}-bound form of the indicator. The overall recorded fluorescence signal is:

$$F = S_D\, c_D + S_{CaD}\, c_{CaD}. \tag{2.31}$$

This relation will be used in section 3.4.1 to calculate $[Ca^{2+}]$ from fluorescence recordings according to the ratiometric formalism.

2.3 Kinetic model of vesicle fusion

A kinetic model of the reaction between Ca^{2+} and the sensor for transmitter release was implemented for two reasons. Firstly, Ca^{2+} binding rate constants can be estimated this way and be compared to in vitro reaction kinetics of putative Ca^{2+} sensor molecules. Secondly, the model allowed us to calculate the expected release of the calyx synapse in response to different $[Ca^{2+}]$ waveforms, which are likely to occur during presynaptic action potentials at the release site, but which cannot be measured directly.

The model consisted of two uncoupled reaction steps, first the Ca^{2+} binding and activation of the Ca^{2+} sensor unit X, and second the fusion reaction of the vesicle, which is promoted by the formation of activated Ca^{2+} sensor units. The sensor unit has five Ca^{2+}-binding sites with identical Ca^{2+} association and dissociation rate constants α, β, respectively. If fully occupied, the sensor switches between the deactivated state XCa_5 and the activated state XCa_5^* with rate constants γ, δ, respectively, which are Ca^{2+}-independent. This is illustrated in the following scheme:

$$\mathrm{X} \underset{\beta}{\overset{5\alpha[Ca^{2+}]}{\rightleftharpoons}} \mathrm{XCa} \underset{2\beta}{\overset{4\alpha[Ca^{2+}]}{\rightleftharpoons}} \mathrm{XCa_2} \underset{3\beta}{\overset{3\alpha[Ca^{2+}]}{\rightleftharpoons}} \mathrm{XCa_3} \underset{4\beta}{\overset{2\alpha[Ca^{2+}]}{\rightleftharpoons}} \mathrm{XCa_4} \underset{5\beta}{\overset{\alpha[Ca^{2+}]}{\rightleftharpoons}} \mathrm{XCa_5} \underset{\delta}{\overset{\gamma}{\rightleftharpoons}} \mathrm{XCa_5^*} \tag{2.32}$$

The vesicle fusion reaction is modeled in a second scheme, in which a fusion-competent vesicle V irreversibly reaches the fused state F at a rate proportional to the occupancy of the release sensor in the activated state, XCa_5^*, at time t:

$$V \xrightarrow{\rho_{max}\, XCa_5^*(t)} F, \tag{2.33}$$

where ρ_{max} is the maximal release rate constant (Fig. 2.5 a). Release rates are calculated by solving the following equation numerically:

$$-\frac{dN}{dt}(t) = \rho_{max}\, XCa_5^*(t)\, N(t), \tag{2.34}$$

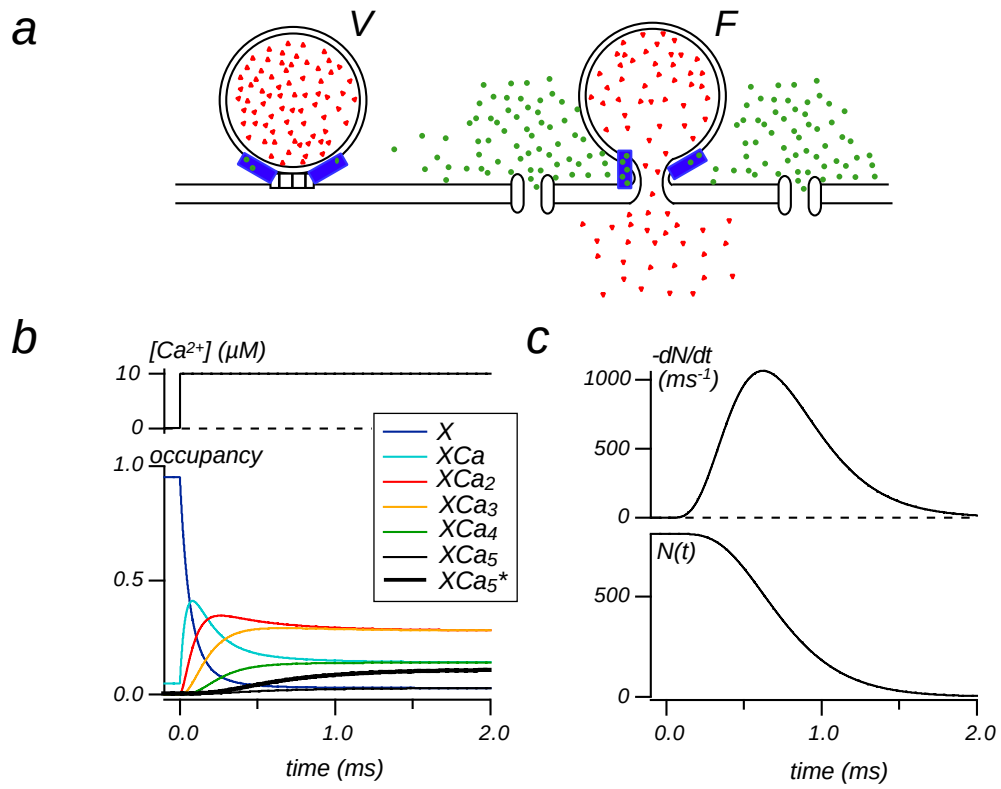

Fig. 2.5: Kinetic model of the Ca^{2+} sensor for release. (**a**) Schematic diagram of a readily releasable vesicle (*V, left*) docked to the membrane. Only if at least one of its Ca^{2+} sensor units (*blue rectangles*) has bound five Ca^{2+} (*green*), it can undergo fusion (*F*, *right*) and release its transmitter content (*red*). (**b**) Occupancy of the possible states of the Ca^{2+} sensor (*bottom panel*) in response to a [Ca^{2+}] jump to 10 µM (*top panel*). (**c**) Release rate (*top panel*) calculated from Eq. 2.34, and release rate integral (*bottom panel*) in response to the [Ca^{2+}] jump shown in (b). The pool of readily releasable vesicles is depleted in ~1.5 ms.

where N is the number of vesicles residing in the readily releasable pool. The boundary condition is $N(0) = 810$, the initial size of the vesicle pool, which was determined independently by action potential trains (*see* section 4.2.3).

The evolution of the Ca^{2+} binding reaction in response to a [Ca^{2+}] step is shown in Fig. 2.5 b. The predicted release rate $-dN/dt$ and the decay of the readily releasable pool $N(t)$ is shown in Fig. 2.5 c.

The system of differential equations arising from the above fusion model were programmed in Mathematica 3.0 (Wolfram Research, Illinois) and solved numerically. Parameters used to describe the experimentally observed release rates were:

$\alpha = 3\times10^8\ M^{-1}s^{-1}$, $\beta = 3{,}000\ s^{-1}$, $\gamma = 30{,}000\ s^{-1}$, $\delta = 8{,}000\ s^{-1}$, $\rho_{max} = 40{,}000\ s^{-1}$.

The fusion model was adjusted to agree with the experimental values, displayed in Fig. 4.8 and Fig. 5.2. Initial fitting trials using an optimization routine showed that the quality of the fit was rather sensitive to variation of the Ca^{2+} association and dissociation rate constants, and suggested the above values for α and β. γ, δ and ρ_{max} were adjusted manually.

To investigate the behavior of the model during simulated action potential-evoked release, a typical [Ca^{2+}] transient was chosen that is expected to occur near release sites. To this end, the time course of the Ca^{2+} current as previously measured (Borst and Sakmann, 1996; Borst and Sakmann, 1998) was taken as a template for the time course of the [Ca^{2+}] transient. It has been shown previously that the release of a vesicle is most likely caused by the Ca^{2+} elevation of overlapping Ca^{2+} microdomains in this synapse (Borst and Sakmann, 1999b). This suggests that the [Ca^{2+}] transient present at the release site is probably not dominated by the stochastic nature of single channel openings. The time course of the Ca^{2+} current was calculated using a Hodgkin-Huxley model, as described by Borst and Sakmann, (1998). The Ca^{2+} current waveform, which had a peak amplitude of –2.6 nA, was multiplied by a constant conversion factor to convert the current into a [Ca^{2+}] transient. To match the quantal content during measured and predicted release evoked by an action potential, the conversion factor was adjusted to 3.4 µM/nA. In Fig. 4.9 and 4.10, predictions of the present Ca^{2+} sensor model were compared to experimental findings regarding the amplitude, rise time and delay of measured EPSCs. In those cases, the release rate predicted by the Ca^{2+} sensor model was convolved with the measured time course of the standard miniature EPSC (*see* section 4.2.2) to obtain a model version of the EPSC, which could be analyzed analogously to measured EPSCs.

3. Methods

This chapter presents the basic measurement techniques as well as the mathematical tools to analyze and interpret the acquired data. All measured quantities in this and later sections are specified as mean ± standard error of the mean (SEM), if not stated explicitly.

3.1 Experimental setup

The Ca^{2+} sensitivity of glutamate release in the MNTB giant synapse was investigated using a combination of electrophysiological and fluorometric methods. In the following, the main components of the setup used in this study are described. While the presynaptic [Ca^{2+}] was optically manipulated and monitored, the electrical responses of the pre- and postsynaptic compartments were measured with the established whole-cell voltage-clamp technique (Hodgkin et al., 1952; Hamill et al., 1981). The setup consisted of an upright microscope (Axioskop, ZEISS, Germany), which was equipped with an epifluorescence port used to deliver the UV excitation light of a monochromator (Monochromator B, TILL photonics, Germany) together with the UV pulse output of a Nd:YAG laser (Minilite II, Continuum, California) to the specimen plane (Fig. 3.1). The brain slice was mounted on a continuously perfused chamber and visualized using infrared trans-illumination, and a video camera (Vidicon, Hamamatsu, Japan) at one of the imaging ports of the microscope (*see also* Fig. 4.1 a). For electrophysiological control, two patch clamp pipettes could be positioned in the perfusion chamber with micro-manipulators (Maerzhaeuser, Germany) under video control. Pre- and postsynaptic voltage clamp recordings were performed using two patch clamp amplifiers (Axopatch 200 A or B, Axon Instruments, California). Fluorescence emission from the specimen plane was detected with a photodiode located at the second imaging port of the microscope and amplified with a third patch clamp amplifier (Axopatch 200 A or B). Stimulation of afferent nerve fibers could be evoked with a bipolar electrode attached to the microscope stage with a manually adjustable holder.

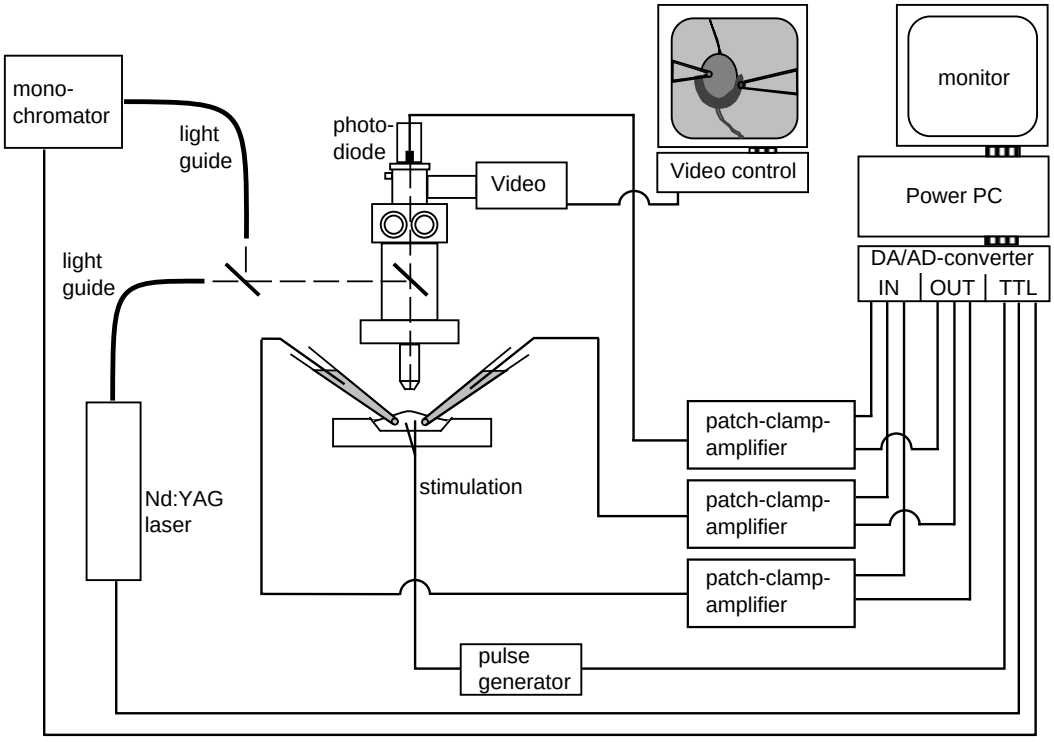

Fig. 3.1: Schematic diagram of the experimental setup. Two patch clamp electrodes and the photodiode for rapid [Ca^{2+}] measurements are amplified using patch clamp amplifiers. The signals are sampled and stored by a computer which also triggers the monochromator for fluorescence excitation and the laser for UV-induced photolysis of the Ca^{2+} cage. Both light sources are coupled via light guides into the epifluorescence port of an upright microscope using two beam splitters. An infrared-sensitive video camera is used to monitor the electrophysiological recording. (Infrared trans-illumination pathway not shown for clarity).

3.1.1 Optical components

3.1.1.1 *Upright microscope, infrared video microscopy of brain slices*

An upright microscope was used to image the brain slice and to measure the fluorescence from microscopic structures of the biological sample. The microscope was equipped with a 60x water immersion objective lens (LUMPlanFL/IR, NA 0.9, Olympus, Japan). Infrared video microscopy has become the standard tool for brain slice imaging. To improve the contrast of the transparent brain slice, a recently developed trans-illumination technique was applied, termed ‘gradient contrast illumination’, in which an asymmetrical spatial filter located in the conjugate aperture plane of the microscope condenser partially blocks the light from the microscope lamp. As a result, the light bundles leave the condenser at a preferential angle, inclined to the optical axis, and illuminate the object in an oblique fashion.

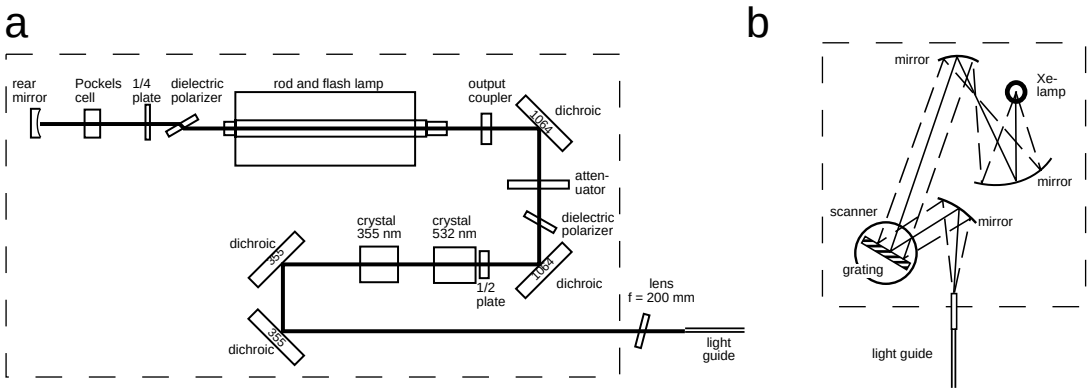

Fig. 3.2: UV light sources. (**a**) Schematic design of the laser head (adapted from Continuum Minilite). Key features are the flash lamp-pumped lasing rod, the Q-switch (Pockels cell, λ/4 wave plate), and the anisotropic crystals for third harmonic generation. (**b**) The monochromator. The spectrum of a Xe lamp is diffracted by a reflection grating. The scanner position determines the wavelength which is coupled into the light guide.

This creates a light-shadow pattern, enhancing the contrast of the video image (Dodt et al., 1999). This system yields a similar image quality as the more common differential interference contrast (DIC) configuration, but has the additional advantage that no optical components (DIC prisms, analyser) are required between the objective lens and the photodetector.

3.1.1.2 *Laser and monochromator*

Two different UV light sources were used to excite the fluorophore and to photolyze the Ca^{2+} chelator, respectively. Ca^{2+} uncaging was performed using a Q-switched neodymium-yttrium aluminum garnet (Nd:YAG) laser, whose frequency-tripled output at 355 nm was coupled into one arm of the epifluorescence port of the microscope. The quality (Q-) switch is implemented by insertion of a Pockels cell within the optical oscillator and yields a pulse width of ~5 ns. Frequency tripling of the fundamental harmonic is based on the principle of higher order harmonic generation in anisotropic optical crystals. In such a crystal, an incident electric field induces dipole oscillations not only at the incident frequency, but also at multiple integers thereof (*see e.g.* Young, 2000). In the present laser, a first KTP crystal generates 532 nm light (Fig. 3.2 a). In a second crystal, frequency mixing of the radiation at 1064 nm and 532 nm results in a fraction of the radiant energy being emitted at the tripled fundamental frequency, i.e. with a wavelength of 355 nm. The undesired wavelengths of the laser (1064 nm, 532 nm) are blocked by suitable dichroic mirrors in the optical path.

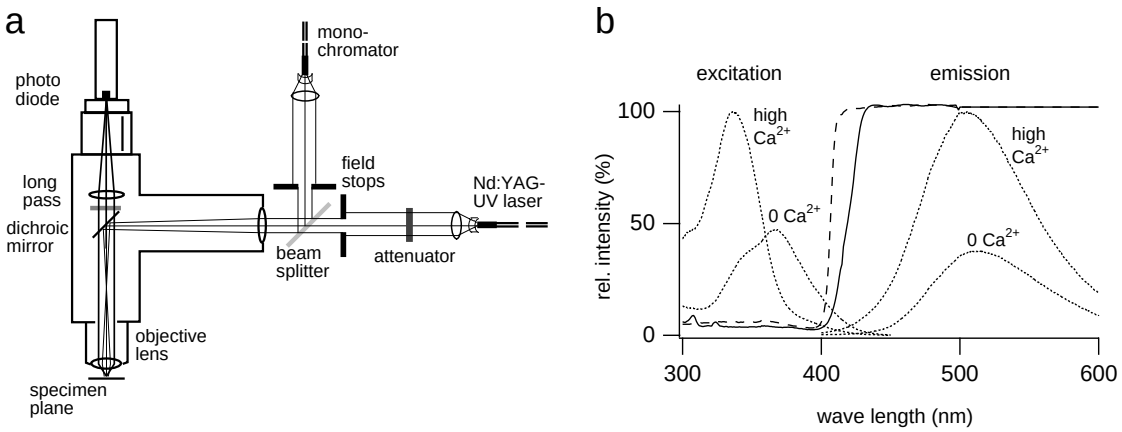

Fig. 3.3: Epifluorescence illumination and spectra of dichroic mirrors and Ca^{2+} indicators. (**a**) UV light exiting the two light guides is collimated, spatially filtered and united before the epifluorescence port of the microscope. A dichroic mirror and a long pass filter in the microscope tube separate excitation from emission light. (**b**) Measured transmittance of the dichroic mirror (*solid line*) and the long pass filter (*dashed line*). The excitation and emission spectra of Fura-2-based Ca^{2+} indicators (*dotted traces)* can be separated with this filter set. Note the characteristic wavelength shift between the excitation spectrum of the indicator in the free (0 Ca^{2+}) and in the Ca^{2+}-bound (high Ca^{2+}) state (Filter spectra measured with a Beckman UD-600 spectrometer, Fura-2 spectra obtained from Molecular Probes).

For dual-wavelength [Ca^{2+}] measurements, the output of a monochromator was coupled into the second arm of the epifluorescence port of the microscope. Monochromatic light of four different wavelengths could rapidly be selected by two TTL bits fed into the monochromator control. The monochromator permits rapid wavelength switching (~ 1 ms) by rotating a reflection grating, which is mounted on a scanner, to preselected positions (Fig. 3.2 b). A beam splitter was used to combine the two UV light sources, nominally reflecting 8% of the monochromator and transmitting 92% of the laser intensity (Fig. 3.3 a). The collimated output of the light guides was spatially filtered using two adjustable, rectangular field stops at the level of the conjugate focal plane in the epifluorescence port.

Excitation and emission light were separated by a dichroic mirror and a long pass filter (TILL photonics) in the microscope tube. The transmittance of these components were checked with a spectrometer (Beckman, UD-600) and are displayed in Fig. 3.3 b.

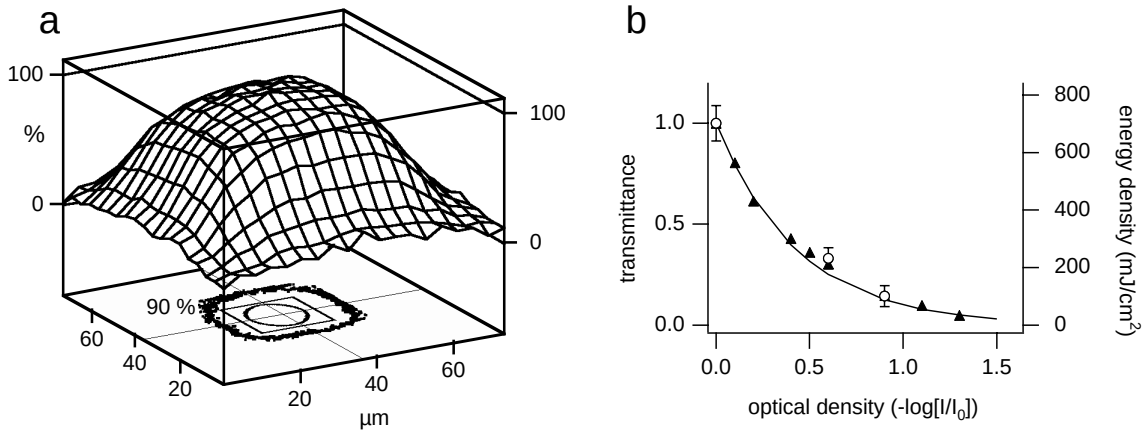

Fig. 3.4: Laser beam profile and attenuation. (**a**) A surface plot of the normalized pulse energy distribution in a subregion of the specimen plane. The square and the ellipse drawn in the bottom plane show the location of the detection area of the photodiode and the idealized boundaries of the postsynaptic neuron, respectively. The 90% level of the energy profile is outlined as dotted contour in the bottom plane. (**b**) The UV pulse energy was attenuated with neutral density filters. Measured pulse energies (*filled triangles*) agreed with the nominal transmittance of neutral density filters (*solid line*). An estimate of the energy density in the area of the photodiode (20 x 20 µm^2, *see* a) is shown for optical densities of 0, 0.6 and 0.9, respectively (*open circles*).

3.1.1.3 *Homogeneity of illumination, energy attenuation*

An important prerequisite of controlled [Ca^{2+}] jumps induced by UV photolysis in an extended compartment is the homogeneity of the UV pulse energy over the boundaries of the compartment. The energy profile in the specimen plane was therefore tested by uncaging fluorescein (2 mM DMNB-fluorescein, MW 3000, Molecular Probes, Oregon). It was mixed with glycerol (5% fluorescein/95% glycerol) to inhibit diffusional spread of the dye, placed under a coverslip and uncaged with laser pulses of different energy. The fluorescence profiles of uncaged fluorescein were imaged with a slow scan CCD camera (PXL, Photometrics, Arizona), and overlaid with the location of the detection area of the photodiode (20 x 20 µm^2), which also encloses the typical circular area with the cross-section of the axo-somatic synapse (15 – 18 µm). The energy profile in the specimen plane (Fig. 3.4 a, average of 6 profiles) is partially shaped by an adjustable rectangular aperture between the light guide exit and the microscope. The profile returns to zero within the field of view, of which Fig. 3.4 (a) only shows a central subregion. The possibility that a single UV pulse saturated the fluorescein uncaging and thus distorted the recorded energy profiles was excluded in experiments with multiple pulses. These experiments showed that the relation between the amount of uncaged fluorescence and the number of pulses was linear. Most importantly, the boundaries of the synapse

are well located within the 90% level of the energy profile. Thus, the requirement for homogeneity is met.

To obtain different [Ca^{2+}] jump amplitudes in subsequent physiological experiments, the pulse energy was attenuated by insertion of neutral density filters in the pathway between the light guide exit and the beam splitter ('attenuator' in Fig. 3.3 a). The pulse energy was then measured using a pyroelectric joulemeter (ED-100A, gentec, Canada) at the level of the back aperture of the objective lens and normalized to the unattenuated peak energy at that location. The peak energy at this level was 47 ± 5 µJ (mean ± S.D., n = 3 experimental days). The transmittance of the neutral density filters agreed well with their nominal values (Fig. 3.4 b). Furthermore, the pulse energy was measured in the focal plane of the objective lens, which yielded a value of 23 ± 3 µJ. With this information, an attempt was made to calibrate the energy density in the region of interest (ROI) covered by the photometric detection area. The ratio of energy absorbed in the ROI over that absorbed in the entire field of view is given by the ratio of the volume integrals of the energy profile measured within the boundaries of the ROI and the field of view, respectively. This ratio is 0.122. Thus, with no attenuation, an energy of 0.122 x 23 µJ irradiates on the ROI measuring 400 μm^2, which results in an energy density of 700 mJ/cm^2. Ca^{2+} uncaging experiments always employed neutral density filters of a nominal OD of ≥0.6, limiting the energy density to < 250 mJ/cm^2 in the ROI. This number, however, should only be considered a rough estimate, because the energy densities measured in the focal plane of the objective lens were close to the maximum density specified for the used joulemeter.

3.1.1.4 *Fast photodetection with photodiode, photodiode holder*

One goal of the study was to measure both the [Ca^{+}] signal and the evoked EPSCs at a high temporal resolution. Therefore, a rapid photometric device was built with a small photodiode and a patch clamp amplifier. This approach was first used by Escobar et al. (1997) to measure the Ca^{2+} uncaging dynamics of Ca^{2+}-DM-nitrophen solutions in small volumes. The low noise characteristics of the capacitive feedback circuit of the patch clamp amplifier (Axopatch 200 A or B) make this system ideal for measuring the small photocurrent in a silicon photodiode (S2386-18K or S5973, Hamamatsu, Japan). The peak photocurrent is a few tens of pA for an indicator-filled volume like the Calyx of Held. In the photometric system, the patch clamp amplifier is used as a current-to-voltage converter. Since the bias voltage of the headstage is limited to 0.2 V and 1 V for the Axopatch 200 A and B, respectively, in some experiments a 9 V

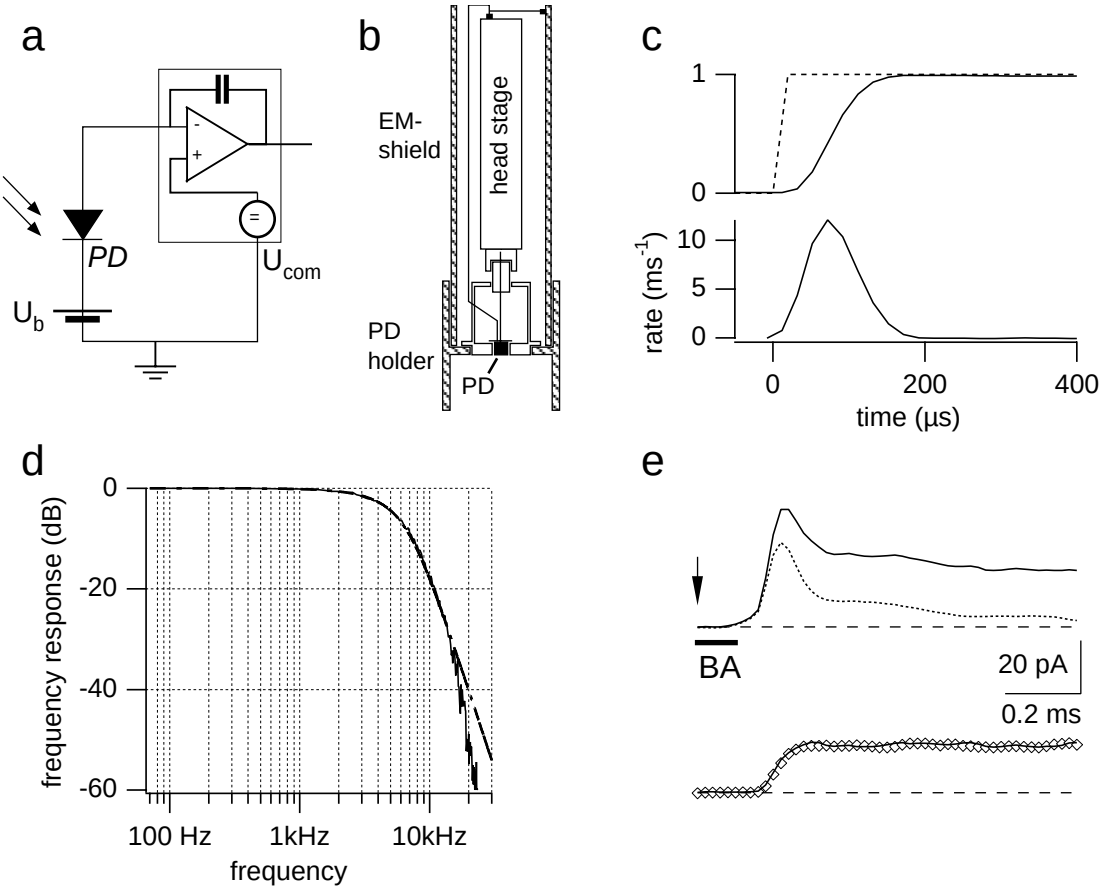

Fig. 3.5: Rapid fluorescence detection with a photodiode. (**a**) Photodetection circuit. The photocurrent is amplified using the headstage of the Axopatch 200 amplifier. To increase the reverse bias voltage, an external battery (U_b, 9V) is included. (**b**) Layout of the photodiode holder (external battery not included). (**c**) Normalized step response (*top solid line*, average of 5 sweeps) and its derivative, the impulse response (*bottom line*), to a LED light pulse (*top dashed line*). (**d**) Frequency response of the photodiode circuit, 3 dB cut-off frequency is 4.1 kHz. The dashed line is the theoretical frequency response of a 4-pole Bessel filter (f_c = 4.2 kHz). (**e**) Signal recovery following a laser pulse. *Top solid trace*: Photocurrent evoked by a laser pulse (*indicated by arrow*) and a simultaneously rising, step-like LED pulse. *Top dotted trace*: Photocurrent evoked by a laser pulse alone. The 'blank activate (BA)' period is indicated by the horizontal bar. The subtraction of the two top signals (*bottom diamonds*) is virtually indistinguishable from the measured LED pulse in the absence of a laser pulse (*bottom solid line*).

battery was added in series with the photodiode to increase the reverse bias voltage and to reduce the noise generated by the semiconductor capacitance (Fig 3.5 a). To further minimize the noise level of the photometric unit, a compact holder was built with short connections between the headstage and the photodiode (Fig. 3.5 b). The large photodiode (S2386-18K) had an active area of 1.1 x 1.1 mm^2 and exhibited a dark noise level of ~0.25 pA_{rms} (5 kHz bandwidth). With the small photodiode (S5973, active area 0.12 mm^2) noise levels below 0.1 pA_{rms} could be obtained.

To characterize the speed of this system, the response to step-like light pulses emitted from a LED was recorded (Fig. 3.5 c). The step response was filtered by a 4-pole Bessel (nominal f_c = 5 kHz) and sampled at 50 kHz. It exhibits a 10-90% rise time of 84 µs and a 0-50% filter delay of 79 µs. The impulse response of the photometric circuit was obtained by calculating the derivative of the step response. Then, the frequency response was calculated as the discrete Fourier transform of the impulse response (Fig. 3.5 d). In addition, the theoretical frequency response *A* was calculated by the formula:

$$A = \frac{A_0}{\prod_n (1 + a_n P + b_n P^2)} \tag{3.1}$$

where n = 2, $A_0 \approx 1$, a_1 = 1.3397, a_2 = 0.7743, b_1 = 0.4889, b_2 = 0.3890 and P = i f/f_c for a 4-pole Bessel filter (Tietze and Schenck, 1978). The cut-off frequency was adjusted to f_c = 4.2 kHz. The theoretical rise time and filter delay are 84 µs and 78 µs, respectively, in very good agreement with the measured values. This indicates that the actual cut-off frequency of the photodiode system is slightly lower than the nominal value of the output filter of the patch clamp amplifier (4-pole Bessel, f_c = 5 kHz). To account for this filtering, the time course of the $[Ca^{2+}]$-dependent fluorescent signal predicted by a model of Ca^{2+} uncaging was digitally filtered before comparing it with the experimentally obtained $[Ca^{2+}]$ time course. For simplicity, a digital 4-pole RC filter (f_c = 4.2 kHz) was used to mimic the filtering of the photometric circuit (implemented in Igor Pro 3.14, Wavemetrics, Oregon).

Next, the ability of the system to accurately measure light signals after a brief, high-intensity laser pulse was examined. The UV pulse evoked a brief current transient in the photodiode system, which is likely to originate from luminescence (i.e. fluorescence *and* phosphorescence, *see* section 2.2) in the optical components of the microscope and in the indicator dyes (Fig. 3.5 e). The so-called flash artifact in the photocurrent record could largely be suppressed by the ‘blank activate (BA)’ function of the Axopatch amplifier, which prevents the amplifier output from saturating for the period the blank activate input sees a high TTL level. To examine the fidelity of the system immediately after the pulse, a laser pulse was combined with the rising edge of a LED light pulse (Fig. 3.5 e, *top traces*). Although the flash artifact exceeds the BA interval (100 µs), the LED pulse can well be measured ~200 µs after the pulse if the laser artifact is measured independently and is later subtracted from the recording that comprises both the LED light step and the coincident laser pulse. During the first ~200 µs, however, the subtraction method is very sensitive to the fast decaying phase

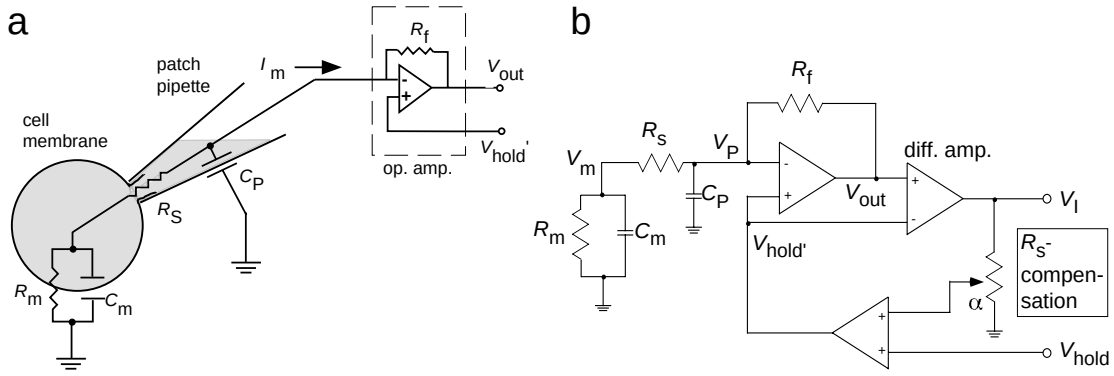

Fig. 3.6: Whole-cell configuration and R_s compensation. (**a**) Electrical access and voltage control over the cell membrane are achieved with a tightly sealed patch clamp pipette. The holding potential V_{hold}' is applied to the non-inverting input of the operational amplifier, which is laid out as a current-to-voltage converter with a resistive feedback loop, i.e. the voltage drop across R_f is proportional to the input current I_m. (**b**) Cell-headstage circuit including R_s compensation. V_I is the voltage drop across R_f, measured as the difference between V_{out} and V_{hold}' (= V_P), and therefore proportional to I_m. To compensate the unavoidable voltage drop across R_s, which is also proportional to I_m, a fraction α of V_I is summed to the command potential V_{hold}. Thus, the deviation of V_m from V_{hold} is reduced ('R_s compensation', *see text for further details*).

of the laser artifact; this interval was therefore not taken into account for further analysis.

3.1.2 Electrophysiological components

3.1.2.1 *Pre- and postsynaptic whole-cell voltage clamp*

The pre- and postsynaptic compartments were electrophysiologically controlled using the whole-cell voltage clamp technique (Hodgkin et al., 1952; Hamill et al., 1981). In short, small glass pipettes with an inner tip diameter of around 1 µm are filled with a saline that resembles the cytosol in its ionic composition. It can furthermore be used to load substances with a special function into the cell interior such as the UV-sensitive Ca^{2+} chelator. When the pipette tip is brought into close contact with a cell membrane and after application of gentle negative pressure, a highly resistive barrier forms between the glass and the lipid bilayer of the membrane, the 'giga-seal'. After rupturing the membrane patch within the pipette tip by a suction pulse, the intracellular compartment is in electrical contact with the pipette electrode and can be held at a command voltage supplied by the headstage, which acts as a current-voltage-converter (Fig 3.6 a).

3.1.2.2 *Bandwidth and fidelity*

The bandwidth of the voltage clamp is mainly determined by the electrical access to the cell interior. This access is impaired by the membrane material in the pipette tip combined in series with the actual resistance of the pipette, giving rise to the series resistance R_s. The series resistance R_s combined with the membrane capacitance C_m form a 1-pole RC filter, which determines the time constant with which voltage steps can charge the plasma membrane. In the present application, no voltage steps were applied; however, the series resistance had a severe impact on the measurement of postsynaptic currents, because together with the membrane resistance R_m, it represents a voltage divider between the pipette electrode and ground (Fig. 3.6 a). This results in a reduction of the command voltage over the cell membrane as soon as a current passes through the series resistance. Just as importantly, the RC filter also limits the bandwidth of the current recording, which may cause problems when one wants to faithfully record fast membrane conductance changes. The patch clamp amplifier is therefore equipped with a feed forward correction loop, called 'R_s compensation', that dynamically corrects the applied command voltage to the desired value, proportionately to the current that passes through the pipette (Fig. 3.6 b). Furthermore, a subsequent stage in the amplifier boosts high frequency components to improve the frequency response of the cell-headstage circuit (not shown). Practically, the electrical cell parameters (whole-cell membrane capacitance C_m and resistance R_m) are estimated by small voltage steps and adjusted at the amplifier, then the amount of correction α (60-100%) is chosen to operate the voltage clamp circuit with fast response characteristics, but without oscillations. The postsynaptic recordings of glutamate activated, AMPA receptor-mediated currents were performed using 90-95 % correction throughout the present study.

Since measured EPSCs evoked by large laser-induced [Ca^{2+}] jumps exhibited 20-80% rise times of not less than 190 µs, independent experiments were performed to test whether this minimum was due to an insufficient bandwidth of the cell-headstage circuit. A model cell (Patch-1U, Axon Instruments) with typical parameters (C_m = 33 pF, R_m = 500 MΩ, R_s = 10 MΩ) was extended by a rapid bounceless switch in parallel to the membrane capacitance in order to mimic the rapid conductance change across the cellular membrane (Fig. 3.7 a). The switch (Sherman et al., 1999) consisted of two AgCl electrodes that were vertically mounted in a syringe tube and electrically connected by KCl saline (150 mM; Fig. 3.7 a, inset). The level of the saline surface could be varied by pressure, which allowed rapid interruption of the electrical contact. Electronic or electromagnetic switches were not used for this application because

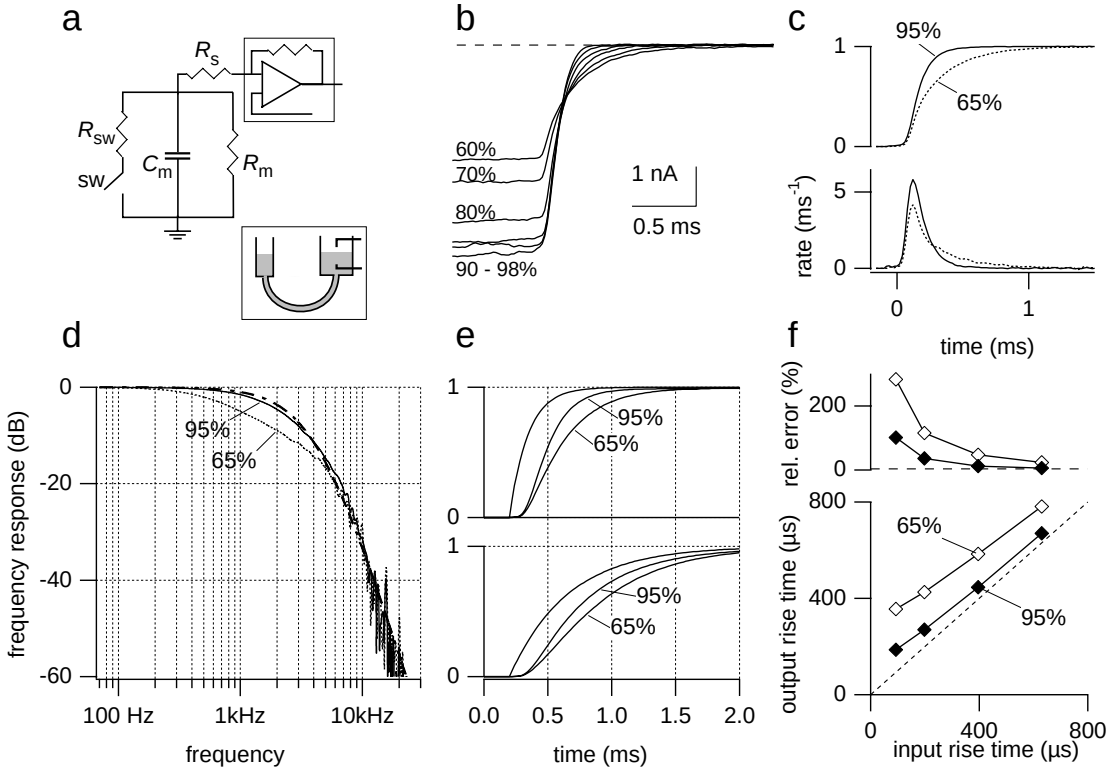

Fig. 3.7: Bandwidth of the electrophysiological recording system. (**a**) Simplified circuit of the model cell and the amplifier headstage. To measure step responses in the presence of R_s compensation, a rapid bounceless switch (sw) was implemented using two AgCl electrodes connected with a KCl solution of variable height (*inset*). (**b**) Step responses to a closed→open transition of the switch, measured with different amounts of R_s compensation, indicated at the traces. (**c**) Step responses recorded with 60–70% and 90–98% R_s compensation were averaged and normalized (*top traces, labeled 65% and 95% respectively*). *Bottom*: The corresponding impulse responses, obtained as derivatives of the step responses. (**d**) The measured frequency responses (*solid and dotted lines*) depend on the amount of R_s compensation. Also shown is the theoretical response of a 4-pole RC filter (f_c = 1.8 kHz, *bold dashed line*). (**e**) Simulated response of the recording system to input signals with a finite rise time. *Top*: input 20-80% rise time 198 µs, *bottom*: input rise time 630 µs. (**f**) *Bottom*: Output vs. input rise time diagram for 65% and 95% R_s compensation, respectively. The *dashed straight line* corresponds to the unity relation. *Top*: Deviation of the rise time of the output from that of the input wavefom in percent.

they often exhibit a slow gating time, high residual currents in the open state or bouncing behavior. Next, step responses of the cell-headstage circuit were measured with different levels of R_s compensation (Fig. 3.7 b), under the assumption that the switch rapidly undergoes a closed-open transition compared to the response time of the circuit. Two effects were observed:

First, the absolute value of the current amplitude in the closed state of the switch increases with the amount of correction. This is because the deviation of the voltage drop across R_m from the command potential adjusted at the amplifier control (-30 mV in this experiment) is reduced with increased correction settings. The residual deviation can be corrected off-line by calculating the residual series resistance R_{res} (= (1-%correction/100)×R_s) and scaling the recorded membrane current I_{meas} with a factor that increases with the voltage drop across R_{res} (Traynelis, 1998). The corrected current I_{corr} is calculated point-wise by the equation:

$$I_{corr} = I_{meas} \frac{V_{hold}}{V_{hold} - I_{meas} R_{res}} \tag{3.2}$$

This correction was applied to all compound EPSCs recorded during the physiological experiments described later.

Second, the rise time of the step responses is a function of the amount of correction (Fig. 3.7 b,c) and sub-maximal correction settings lead to increased rise times. The averaged step responses for 60-70% and 90-98% correction were normalized and the impulse response was calculated by numerical differentiation. The magnitude of the discrete Fourier transform yielded the effective frequency response of the cell-headstage circuit, which exhibited a stronger attenuation of frequencies between 0.3 and 5 kHz for the low compensation setting compared to the high setting (Fig. 3.7 d). The phase response was linear within the pass band of the filter (not shown). The frequency response of the 95% correction setting was compared to the theoretical frequency response and could satisfactorily be described by a 4-pole RC filter with f_c = 1.8 kHz (*compare* Eq. 3.1). An ideal filter of this type has a 10-90% rise time of 190 µs (Tietze and Schenck, 1978), somewhat faster than that of the measured step response ($t_{10\text{-}90\%}$ = 226 µs; $t_{20\text{-}80\%}$ = 140 µs). Since the ideal 4-pole Bessel filter has a 0–50% filter delay of 141 µs, also the recorded time course of an EPSC will be shifted in time compared with the real event by that delay. Because in physiological experiments the cell parameters naturally varied, a value of −100 µs was used to shift measured EPSCs to the left on the temporal axis, thus accounting for the estimated filter delay.

The calculated impulse responses were used to compare the systems output with a given input waveform. Theoretical input signals (mono-exponential functions) were convolved with the impulse response, and the 20-80% rise time of the output signal was compared to that of the input signal (Fig. 3.7 e,f). It is observed that, with 95% compensation, an input signal with $t_{20\text{-}80\%}$ = 198 µs gives rise to an output with $t_{20\text{-}80\%}$ = 270 µs, and an input signal with $t_{20\text{-}80\%}$ = 630 µs yields an output with $t_{20\text{-}80\%}$ = 670 µs. The fidelity at 65% R_s compensation is clearly reduced (Fig. 3.7 f, *open symbols*).

Since, at 95% correction, the step response exhibits a 20-80% rise time of 140 µs, also the rise times of the fastest compound EPSCs ($t_{20\text{-}80\%}$ = 220 ± 12 µs; n = 4) were probably not limited by the bandwidth of the cell-headstage circuit. Therefore, the measured compound EPSCs contain sufficient information to analyze the underlying transmitter release rates, provided the waveform of the EPSC evoked by transmitter release from a single vesicle is known (*see next section*). These miniature EPSC (mEPSC) waveforms were measured in identical experimental conditions and averaged (*see* section 4.2.2). The 20-80% rise time of the 'standard' mEPSC (120-130 µs), however, was very close to the step response rise time of the system. Thus, the rise time of the quantal EPSC is only an upper limit for the duration of AMPA receptor channel activation in response to a single transmitter packet.

3.2 Extraction of transmitter release rates from compound EPSCs

The postsynaptic response to glutamate, i.e. the AMPA receptor mediated EPSC, was used as an assay of presynaptic vesicle fusion and transmitter release. Strictly, this observable is a reliable measure of presynaptic fusion rates only, if the compound EPSC is a linear superposition of identical quantal EPSCs, of which each results from transmitter release from a single vesicle. Ideally, the time course of the compound EPSC can be written as:

$$I(t) = \zeta(t) * q\,F(t), \tag{3.3}$$

which is the convolution of the vesicle release rate ζ with the quantal EPSC of peak amplitude q (quantal size, *see* section 1.1.3) and normalized time course $F(t)$. This relation is not valid, if vesicles do not contribute independently to the compound EPSC, which may be the case if, for example, a build-up of glutamate in the synaptic cleft leads to postsynaptic receptor desensitization or saturation, which would alter the quantal EPSC amplitude and time course while the compound EPSC develops. These effects are discussed in section 5.2.2.2. Here, the validity of the above equation is assumed for short release periods (≤ 5 ms following the onset of release) and a way is described to back-calculate the release rate on the basis of Eq. 3.3.

The quantal EPSC amplitude q and waveform $F(t)$ were estimated in independent experiments as described in section 4.2.2, assuming that the majority of spontaneously occurring miniature EPSCs (mEPSCs) are evoked by release of a single transmitter packet. The averaged mEPSC had a peak amplitude of –31.1 pA, a 20-80% rise time

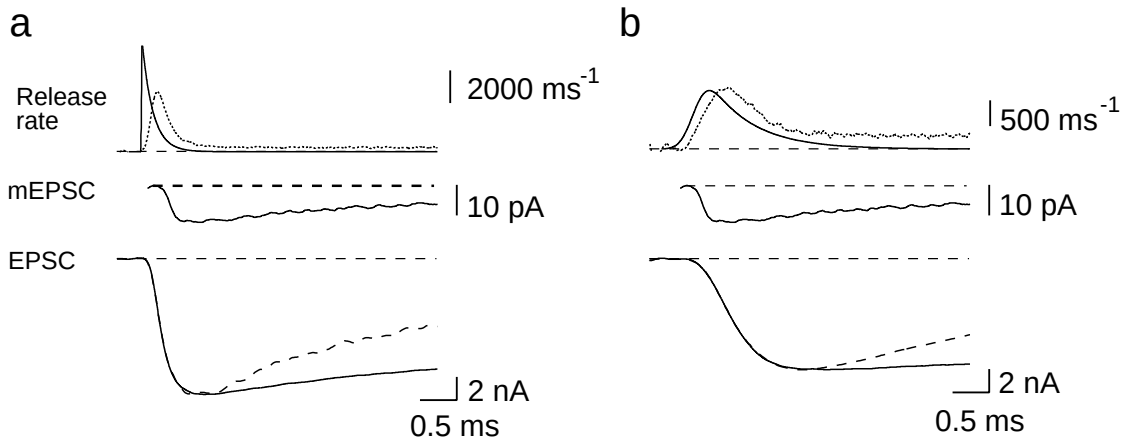

Fig. 3.8: Calculation of release rates. (**a**) The rising phase of the measured EPSC (*bottom, solid line*) was fit with the convolution (*bottom, dashed line*) of the miniature EPSC waveform (mEPSC, *middle panel*) with a theoretical release rate (*top, solid line*). The release rate calculated with Eq. 3.6 is shown for comparison (*top, dotted line*). The peak release rate is underestimated using Eq. 3.6, because it assumes an instantaneous rise of the mEPSC. (**b**) Same as in (a) for a more slowly rising EPSC. For slower release events, the release rate calculated with the convolution algorithm and with Eq. 3.6 give similar results. The mismatch between modeled and measured EPSCs following the peak of the EPSC may be because of accumulation of glutamate in the synaptic cleft or because of a slower release component not accounted for in the theoretical release rate waveform.

of 123 µs ($t_{10\text{-}90\%}$ = 192 µs) and decayed bi-exponentially (τ_1 = 2.4 ms (45.4%), τ_2 = 7.0 ms (54.6%); fit to a 25 ms interval beginning at the peak). Alternatively, the averaged mEPSC could be approximated with an analytical function of the form:

$$\text{mEPSC}(t) = A_1\,(1+\text{erf}(k_1(t\text{-}t_0)))\times[A_2\exp(-k_2(t\text{-}t_0)) + A_3\exp(-k_3(t\text{-}t_0))] \qquad (3.4)$$

(with free parameters A_i, k_i (i = 1, 2, 3) and t_0), which gave similar rise and decay time constants (Bollmann et al., 2000). Given the measured average mEPSC, the release rate was back-calculated from a measured compound EPSC by convolving the average mEPSC with a theoretical release rate time course of the form:

$$f(t) = A\left(1+\text{erf}\left[k_1\left(t-t_0\right)\right]\right)\times\exp\left[-k_2\left(t-t_0\right)\right] \qquad (3.5)$$

and fitting the convolution to the measured EPSC by variation of A, k_1, k_2 and t_0. This simple release rate waveform yielded good fits of the EPSC between the baseline and the peak of the EPSC (Fig. 3.8). At later times, the fit could not account for the often slow decay of the measured EPSC. Probably, this could have been improved by adding a second, more slowly decaying exponential term to the release rate time course. In order to reduce the number of fit parameters, this term was not included, because only *peak* release rates, which occurred during the fast rising phase of the

EPSC, were used to compare modeled and experimental release rates. The optimization was performed using a simplex algorithm (programmed in Igor Pro 3.14; provided by Dr. G. Borst). The fit release rate was then evaluated at its peak and compared to the peak release rate calculated with a model of Ca^{2+}-triggered vesicle fusion (*see* section 2.3).

A simpler approach to retrieve release rates is described by Van der Kloot (1988), which is based on the assumption that the rise time of the quantal EPSC is much faster than the rise time of the compound EPSC and that it decays with a single time constant τ_0. In that case, the quantal EPSC is assumed to rise quasi-instantaneously and the release rate is simply given by:

$$\zeta(t) = \frac{1}{q}\left(\frac{dI_{EPSC}(t)}{dt} + \frac{I_{EPSC}(t)}{\tau_0}\right) \tag{3.6}$$

where I_{EPSC} is the compound EPSC, and q the peak amplitude of the quantal EPSC. Using this deconvolution method for very rapid EPSCs measured in the Calyx of Held leads to an underestimation of maximal release rates (Fig. 3.8 a), because the quantal EPSC rises only about two times faster than the fastest compound EPSCs. Conversely, the observation that 20-80% rise times of compound EPSCs reached a minimum of ~220 µs, clearly slower than the 20-80% rise time of the measured step response (140 µs) and also slower than that of the mEPSC (120–130 µs) suggests that the derived maximum release rates reflect the physiological maximum of the release process rather than the limited bandwidth of the recording system.

3.3 Preparation and electrophysiological recordings

3.3.1 Brain slice preparation, stimulation and extracellular solutions

Transverse brainstem slices were obtained from 8- to 10-day old Wistar rats. Briefly, the animal was decapitated, and a block containing the brainstem and the cerebellum was isolated and glued to the bottom of a slice chamber. Using a vibratome (Campden Instruments, England), four to five 200-µm-thick brainstem slices were cut and incubated at 37°C for 30 min. The preparation was done in ice-cold solution containing (in mM): 125 NaCl, 2.5 KCl, 3 $MgCl_2$, 0.1 $CaCl_2$, 25 dextrose, 1.25 NaH_2PO_4, 0.4 ascorbic acid, 3 *myo*-inositol, 2 sodium pyruvate and 25 $NaHCO_3$ (bubbled with 5% CO_2, 95% O_2, pH 7.4). The solution used during experiments had the same composition, except it contained 1 mM $MgCl_2$ and 2 mM $CaCl_2$. During electrophysiological recordings, postsynaptic NMDA receptors were blocked by D-2-

amino-5-phosphonovalerate (D-APV, 50 µM, Tocris Cookson, UK). Cyclothiazide (CTZ, 100 µM, Tocris) was added to minimize postsynaptic AMPA receptor desensitization (*see* section 4.2.1). Experiments were done at room temperature (20-24°C).

Presynaptic axons were stimulated with a bipolar teflon coated steel electrode positioned at the midline of the brain slice (Fig. 3.9). For pre- and postsynaptic recordings, only synapses were selected that exhibited an extracellular field potential of two spikes separated by ~1 ms, corresponding to the pre- and postsynaptic action potential. Thus, the size of the releasable vesicle pool could first be estimated by afferent stimulation of the intact terminal, before it was challenged by photolysis-evoked [Ca^{2+}] jumps.

3.3.2 Whole-cell recordings, intracellular solutions

Simultaneous pre- and postsynaptic whole-cell recordings from giant synapses were performed using two Axopatch 200 (A or B) amplifiers. The postsynaptic pipette solution contained (in mM): 125 cesium gluconate, 20 CsCl, 10 disodium phosphocreatine, 4 MgATP, 0.3 GTP, 10 HEPES, 0.5 EGTA (pH 7.2). Postsynaptic pipettes had an open-tip resistance of 2-3 MΩ. The uncompensated series resistance was 12 ± 1 MΩ (n = 43), electronically compensated to 90–95 %. The recorded EPSCs were corrected off-line for the voltage error caused by the residual series resistance (*see* section 3.1.2.2).

The presynaptic pipette solution contained the Ca^{2+}-DM-nitrophen complex in different concentrations, depending on which [Ca^{2+}] levels were desired (*see* Table 3.1). To keep the osmolality of the solution constant at around 310 mmol/kg, the potassium concentration was varied. In several experiments, Na_2ATP and $MgCl_2$ were added to test for an effect of MgATP on the release mechanism or on replenishment of the releasable vesicle pool. Either Mag-Fura-2 (Molecular Probes) or Fura-2-FF (TefLabs, Texas) were used as low-affinity Ca^{2+} indicators to circumvent the temporal filtering effects of Ca^{2+} buffering that are introduced by Ca^{2+} indicators of high affinity. All presynaptic solutions contained in (mM): 20 KCl or NaCl, 30 HEPES (pH 7.2), 1 Ca^{2+} indicator (*see* Table 3.1). Solution A1, A2 and A3 were used to evoke Ca^{2+} jumps between 0.5 and 100 µM, B was used for jumps with $0.5 \leq [Ca^{2+}] \leq 15$ µM. With solutions C, D and E, the calibration constants of the Ca^{2+} indicator were

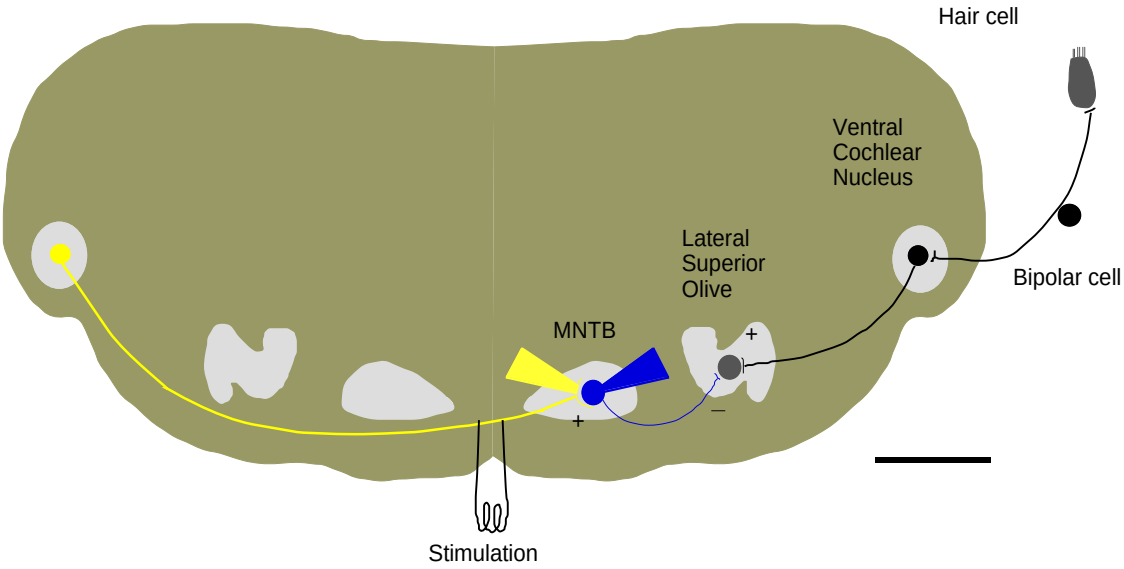

Fig. 3.9: Rat brainstem preparation. The Calyx of Held represents a relay synapse in the binaural auditory pathway. The presynaptic neuron, the globular bushy cells (yellow) in the anteroventral cochlear nucleus (AVCN) project contralaterally to the medial nucleus of the trapezoid body (MNTB), where an excitatory (+), glutamatergic synapse is formed with the soma of a principal neuron (blue). MNTB principal neurons form inhibitory (-), glycinergic synapses with neurons in the lateral superior olive (LSO), which also receive excitatory input from the ipsilateral AVCN. The convergence of binaural auditory information in the LSO is thought to play a role in sound localization (Helfert and Aschoff, 1997). Horizontal scale bar: ~0.5 mm.

determined in the presynaptic terminal. Presynaptic pipettes (4–6 MΩ) were used to dialyze the terminal for at least 4 minutes before a laser pulse was applied.

All compound EPSCs and spontaneous mEPSCs were filtered at 5 kHz (4-pole Bessel filter), digitized with an A/D-converter (ITC 16, Instrutech, New York), stored and analyzed using a Power PC 8100/110 (Apple Macintosh**,** California). Miniature release events following $[Ca^{2+}]$ jumps to <1.5 µM were filtered at 2 kHz, in some experiments after wash-out of CTZ. Fluorometric and electrophysiological data were acquired with the PulseControl Software 4.7 (Herrington et al., 1995) programmed for the IgorPro 3.14 data acquisition and analysis software package (Wavemetrics, Oregon). The analysis of digital records was performed by customized routines in the IgorPro macro programming language.

3.3.3 Adjustment of the DM-nitrophen – $CaCl_2$ *equilibrium*

The initial [Ca^{2+}] level in the presynaptic solution is an important parameter and should be adjusted to a pCa ~7. At higher pCa, a large amount of DM-nitrophen remains in the unbound state and can act as a potent buffer for uncaged Ca^{2+}, thus producing large and rapid Ca^{2+} spikes (Escobar et al., 1997). Is it lower, the intracellular [Ca^{2+}] appreciably exceeds the physiological resting value of 50-100 nM and the state of the dialyzed terminal may deviate significantly from its resting conditions. Unfortunately, the purity of DM-nitrophen was quite variable and therefore, the adjustment of the DM-nitrophen–Ca^{2+} balance could not rely on nominal concentration values; this method would have been compromised further due to pipetting errors when µl volumes are handled. Instead, the presynaptic solution was prepared with a nominal DM-nitrophen concentration of 11.6 mM, and then a variable amount of $CaCl_2$ was added. A small sample volume of this solution was mixed with Fura-2 (0.2 mM) and the free [Ca^{2+}] was fluorometrically determined using microcuvettes. If it was around 100 nM, the remaining solution was mixed with the low affinity indicator Mag-Fura-2 or Fura-2-FF for use in subsequent [Ca^{2+}] jump experiments. Given a K_D of DM-nitrophen for Ca^{2+} of 5 nM (Kaplan and Ellis-Davies, 1988), the purity of the DM-nitrophen stock was calculated to be 70-90%, which results in an effective DM-n concentration of ~9 mM in solutions A1 and B. The presynaptic solution was newly prepared on each experimental day and its basal [Ca^{2+}] was measured to prevent uncertainties in the purity levels of DM-nitrophen, which may degrade by multiple freezing and thawing cycles (Zucker, 1993).

3.4 Optically controlled, intracellular [Ca^{2+}] jumps

Since the natural ways, in which the presynaptic terminal tightly controls the intracellular [Ca^{2+}] (localized Ca^{2+} influx, buffered diffusion, internal uptake and extrusion), give rise to complex and hardly resolvable fluctuations in the local [Ca^{2+}], an ‘artificial’ way was employed to rise the presynaptic [Ca^{2+}] homogeneously and to measure it simultaneously. Both aspects are brought about by optical means. The first subsection describes the methods of quantifying absolute [Ca^{2+}] changes with fluorometric Ca^{2+} indicators, while the second subsection will explain the methods of UV laser-induced [Ca^{2+}] elevations.

	A 1 2 3	B	C (R_{min})	D (R_{max})	E (K_{eff})
K-gluconate	90/100/100	50	60	60	40[*)]
DM-n	9 / 4.5 / 2.3	9	9	9	9
$CaCl_2$	8.6 / 4.3 / 2.2	6.5	-	20	17[1)]/ 13[2)]
Na_2-ATP	-	10	-	-	-
$MgCl_2$	-	3	-	-	-
PC / GTP	-	10 / 0.3	-	-	-
EGTA	-	-	20	-	
DPTA	-	-	-	-	25
Ca^{2+} indicator	MF or FF	FF	MF or FF	MF or FF	MF or FF

Table 3.1: Presynaptic pipette solutions. Concentrations in mM. Solutions A and B were used for presynaptic Ca^{2+} uncaging to levels between 0.5 – 100 µM. For small $[Ca^{2+}]$ jumps (< 6 µM), the relative amount of DM-n/$CaCl_2$ was reduced in solution A (A2 and A3). C, D and E were used for in situ calibration of the Ca^{2+} indicators. All solutions contained HEPES (30 mM), pH ~7.2 (adjusted with KOH or NaOH, respectively).
[1)] K_{eff} of Mag-Fura-2 was determined with 17 mM $CaCl_2$, yielding a calculated $[Ca^{2+}]_{free}$ of 32 µM. [2)] For Fura-2-FF, 13 mM $CaCl_2$ were added, yielding a calculated $[Ca^{2+}]_{free}$ of 14 µM. [*)] In E, Na-gluconate and NaCl replaced K-gluconate and KCl, respectively, and the extracellular $[Ca^{2+}]$ was lowered to < 0.1 mM to inhibit the Na^+-Ca^{2+}-exchanger of the presynaptic cell membrane. Abbreviations: MF: Mag-Fura-2, FF: Fura-2-FF, DM-n: DM-nitrophen, PC: phosphocreatine.

3.4.1 Ratiometric $[Ca^{2+}]$ measurements

The metal complex form of a ratiometric ion indicator exhibits a shifted absorption spectrum when compared to the spectrum of the free indicator molecule (*see* Fig. 3.3 b). By measuring the fluorescence of the indicator at two excitation wavelengths, this property can be used to determine absolute $[Ca^{2+}]$ values independent of the dye concentration. Fig. 3.10 (a) displays the sequence of illumination intervals, and the fluorescence signals measured from microcuvettes (inner diameter: 0.2 x 0.02 mm, Microslides, VitroCom, New Jersey) filled with solution B. After subtraction of the flash artifact recorded separately (section 3.1.1.4), the fluorescence time course can be converted to $[Ca^{2+}]$ according to the following formalism:

Let F_1 and F_2 be the fluorescence intensities measured in a sample (microcuvette or presynaptic terminal) with the excitation wavelengths λ_1 and λ_2, respectively.

According to Eq. 2.31, F_1 and F_2 are proportional to the concentration of the Ca^{2+} indicator in the free and the Ca^{2+}-bound form, [D] und [CaD]:

$$\begin{aligned} F_1 &= S_{D,1}[D] + S_{CaD,1}[CaD] \\ F_2 &= S_{D,2}[D] + S_{CaD,2}[CaD] \end{aligned} \quad . \tag{3.7}$$

$S_{D,i}$, $S_{CaD,i}$ (i =1,2) are constants, which are determined by, for example, the excitation intensity and quantum efficiency of the detection system, and by the molar extinction coefficient and the quantum efficiency of the Ca^{2+} indicator.

The law of mass action predicts:

$$[CaD] = [D]_{tot} \frac{[Ca^{2+}]}{[Ca^{2+}] + K_D} \tag{3.8}$$

$$[D] = [D]_{tot} \frac{K_D}{[Ca^{2+}] + K_D} \quad , \tag{3.9}$$

where $[D]_{tot}$ = [D] + [CaD] represents the total concentration of indicator in the sample. The ratio R of the two fluorescence signals is independent of $[D]_{tot}$ and can be expressed, using Eq. 3.7 – 3.9, as:

$$R = \frac{F_1}{F_2} = \frac{S_{D,1}[D] + S_{CaD,1}[CaD]}{S_{D,2}[D] + S_{CaD,2}[CaD]} = \frac{S_{D,1}K_D + S_{CaD,1}[Ca^{2+}]}{S_{D,2}K_D + S_{CaD,2}[Ca^{2+}]} \tag{3.10}$$

This equation can be solved for $[Ca^{2+}]$:

$$[Ca^{2+}] = K_D \frac{S_{D,2}}{S_{CaD,2}} \frac{S_{D,1}/S_{D,2} - R}{R - S_{CaD,1}/S_{CaD,2}} \quad . \tag{3.11}$$

Finally, the following calibration constants are introduced:

$$R_{min} = \frac{S_{D,1}}{S_{D,2}} \tag{3.12}$$

$$R_{max} = \frac{S_{CaD,1}}{S_{CaD,2}} \tag{3.13}$$

$$K_{eff} = K_D \frac{S_{D,2}}{S_{CaD,2}} \tag{3.14}$$

K_{eff} can simply be expressed in terms of the dissociation constant K_D and R_{min} and R_{max}, if λ_1 corresponds to the isosbestic wavelength λ_{iso} of the indicator's excitation spectrum. At this wavelength, the fluorescence is independent of the fraction of the indicator bound to Ca^{2+} such that $S_{CaD,1} = S_{D,1}$. In this case, K_{eff} can be written as:

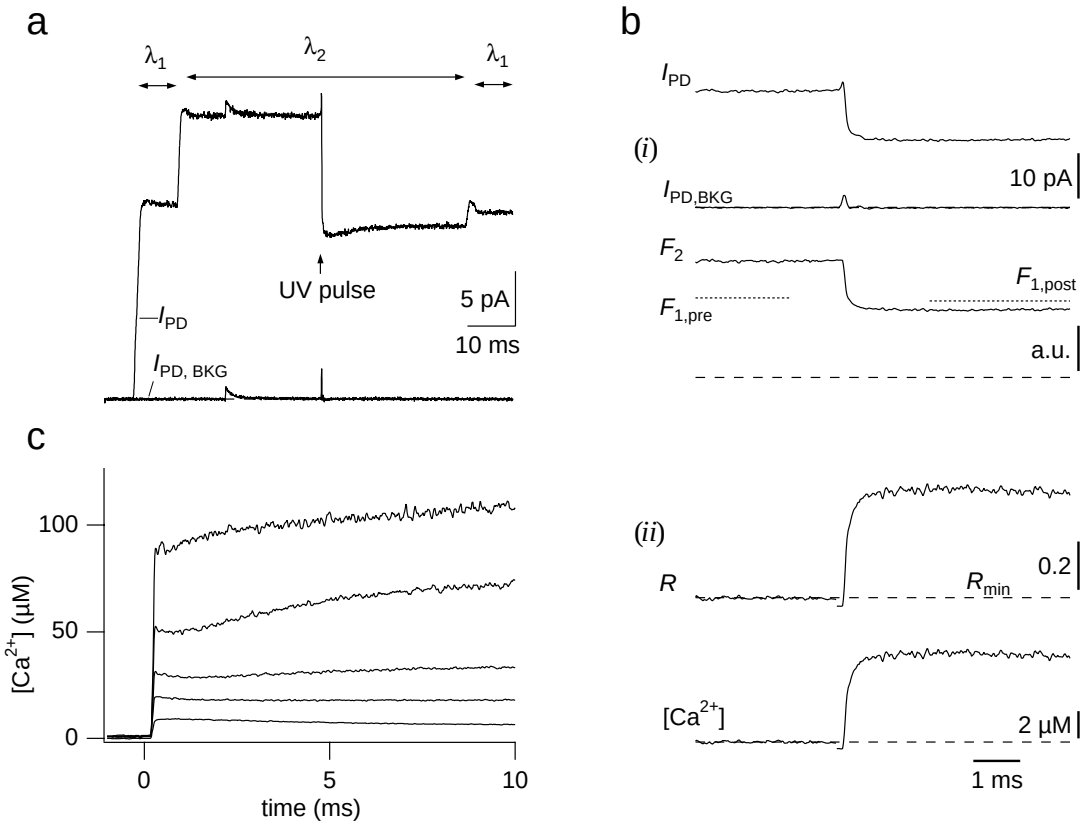

Fig. 3.10: Ratiometric [Ca^{2+}] measurements and [Ca^{2+}] jumps evoked by laser photolysis. (**a**) Sequence of illumination intervals. The fluorescence change in the test solution (B in table 3.1) was measured in microcuvettes. During the UV pulse (*arrow*), the sample is illuminated with λ_2 = 380 nm, and the change in [Ca^{2+}] is detected as a rapid decrease in the photocurrent I_{PD}. Briefly before and after the pulse, the Ca^{2+}-independent fluorescence is recorded by switching to the isosbestic wavelength, λ_1. The background signal arising from the UV pulse alone ("flash artifact") is recorded separately ($I_{PD,\ BKG}$), while the monochromator is switched off. The small transient *before* the UV pulse is a discharge current of the capacitative headstage evoked by a controlled 'forced reset'. (**b**) Background subtraction and ratiometric conversion of fluorescence records. (***i***) After subtraction of the background ($I_{PD,\ BKG}$) from the signal (I_{PD}), the Ca^{2+}-sensitive fluorescence (F_2) is obtained (expressed in arbitrary units, a.u.). (***ii***) The ratio R ($=F_1/F_2$) of the fluorescence record is formed, which exhibits a small discontinuity at the time of the UV pulse, because $F_{1,pre}>F_{1,post}$. R can then be converted to [Ca^{2+}], using Eq. 3.16. (**c**) Range of [Ca^{2+}] jumps that can be evoked by laser photolysis. Solution A was used in microcuvettes.

$$K_{\text{eff}} = K_{\text{D}} \frac{S_{\text{D},2}}{S_{\text{CaD},2}} \frac{S_{\text{CaD},1}}{S_{\text{D},1}} = K_{\text{D}} \frac{R_{\max}}{R_{\min}} \quad . \tag{3.15}$$

Inserting Eq. 3.12 – 3.15 into Eq. 3.11 results in the classical equation for ratiometric [Ca^{2+}] measurements:

$$[\text{Ca}^{2+}] = K_{\text{D}} \frac{R_{\max}}{R_{\min}} \frac{R - R_{\min}}{R_{\max} - R} = K_{\text{eff}} \frac{R - R_{\min}}{R_{\max} - R} \quad . \tag{3.16}$$

Calibration

In order to obtain absolute [Ca^{2+}] values, the calibration parameters R_{min}, R_{max} und K_{eff} must be determined. This is achieved by recording the fluorescence signals from calibration solutions in which the [Ca^{2+}] is adjusted to known values, using appropriate Ca^{2+} buffers. This should be done in the same experimental environment, in which the [Ca^{2+}] is to be determined, because the calibration parameters may vary due to optical and chemical differences. Thus, R_{min}, R_{max} und K_{eff} were measured in presynaptic terminals with solutions of similar composition as those used for later Ca^{2+} uncaging experiments. In particular, since DM-nitrophen absorbs in the UV range and may contribute to the fluorescence signal (Zucker, 1992), it was also included in the calibration solutions.

R_{min} was determined by adding the high affinity Ca^{2+} buffer EGTA to the presynaptic solution (solution C, Table 3.1), which should buffer the intracellular [Ca^{2+}] to nanomolar levels. R_{max} was measured with a high $CaCl_2$ solution (solution D) such that the indicator was saturated with Ca^{2+}. To determine the K_D of the indicator, a solution was prepared with a balanced mixture of $CaCl_2$ and DPTA, a low affinity Ca^{2+} buffer, at high concentrations (solution E). The K_D of DPTA for Ca^{2+} (80 µM, Neher and Zucker, 1993) was confirmed by Scatchard analysis with a Ca^{2+}-sensitive electrode. The free [Ca^{2+}] in this solution (E) was calculated to be 32 µM and 14 µM, respectively, for the ionic compositions stated in Table 3.1, which were used to calibrate Mag-Fura-2 and Fura-2-FF, respectively.

Since the UV pulse may change the calibration parameters, R_{min}, R_{max} und K_{eff} were analyzed before and after a laser pulse. Thus, pre- and postflash parameters were obtained for two different attenuation levels (neutral density filter, OD = 0.9 and 1.5) and interpolated for other attenuation levels (Table 3.2).

3.4.2 Rapid [Ca^{2+}] elevations, evoked by laser photolysis

3.4.2.1 *Choice of the UV-sensitive* Ca^{2+} *chelator*

As mentioned above, the difficulty to resolve local [Ca^{2+}] elevations near the Ca^{2+} sensor during action potentials is overcome by the much better controllable approach of raising the [Ca^{2+}] homogeneously, so that the measured intracellular [Ca^{2+}] is most likely the effective [Ca^{2+}] at the Ca^{2+} sensor for transmitter release. To do so, the UV-

	Mag-Fura-2		Fura-2-FF	
	OD 0.9	OD 1.5	OD 0.9	OD 1.5
$R_{min, pre}$	0.358 ± 0.007 (5)		0.734 ± 0.01 (5)	
$R_{min, post}$	0.360 ± 0.009 (5)	0.361 ± 0.008 (5)	0739 ± 0.011 (5)	0.743 ± 0.008 (5)
$R_{max, pre}$	4.61 ± 0.52 (5)		6.23 ± 0.27 (5)	
$R_{max, post}$	4.65 ± 0.57 (5)	4.32 ± 0.58 (5)	5.65 ± 0.10 (5)	6.04 ± 0.27 (5)
$K_{D, pre}$	30.9 ± 2.6 (9)		8.89 ± 0.58 (6)	
$K_{D, post}$	32.2 ± 2.4 (9)	29.5 ± 2.3 (9)	7.90 ± 0.64 (6)	8.24 ± 0.66 (6)

Table 3.2: Ratiometric *in situ* calibration parameters. Calibration constants to convert fluorescence records into [Ca^{2+}] were determined before and after a UV pulse, which was attenuated with neutral density filters (optical density 0.9 and 1.5, respectively). Stated as mean ± SEM (number of cells). Most calibration parameters were not significantly different before and after the flash (paired t-test, P>0.05).

sensitive Ca^{2+} chelator DM-nitrophen was dialyzed into the presynaptic terminal and partially photolyzed with a strong UV pulse. Due to its high affinity (K_D = 5 nM Kaplan and Ellis-Davies, 1988), it can be almost completely loaded with Ca^{2+}, while the equilibrated free [Ca^{2+}] remains in the 100 nM range. The photoproducts exhibit a dramatically reduced affinity for Ca^{2+} (K_D = 3 mM). Since DM-nitrophen is a derivative of the Ca^{2+} chelator EDTA, it also exhibits a relatively high affinity for Mg^{2+} (K_D = 2.5 µM), which limits its use when molecular signal cascades are to be examined that depend on the hydrolysis of MgATP. Other Ca^{2+} cages are available, which have a higher specificity for Ca^{2+}, but also lack the very high affinity for Ca^{2+} compared to that of DM-nitrophen. For example, the UV-sensitive Ca^{2+} chelator nitrophenyl-EGTA, (NP-EGTA) has a K_D of 80 nM (Ellis-Davies and Kaplan, 1994), and can therefore be loaded only up to ~60% with Ca^{2+} if the free [Ca^{2+}] should not exceed ~100 nM. It also exhibits a ~4-fold lower extinction coefficient compared to DM-n, while the quantum yield is of comparable magnitude (DM-n: 0.18, NP-EGTA: 0.2-0.23). Thus, NP-EGTA was not suitable to evoke [Ca^{2+}] jumps to more than 5 µM even when used at a concentration of 10 mM. Therefore, the advantageous properties of DM-nitrophen were used to evoke large Ca^{2+} jumps of up to 100 µM (Fig. 3.10 c), while Mg^{2+} and ATP were omitted from the presynaptic pipette solution (solution A). In other experiments, a solution (solution B) was used, in which $MgCl_2$ (3 mM) and Na_2-ATP (10 mM) were included to test whether MgATP affects the rate of neurotransmitter release at a given [Ca^{2+}] (Heidelberger, 1998). The free [Ca^{2+}] in this solution was adjusted by addition of $CaCl_2$, until it exhibited a pCa of ~7, as measured with Fura-2 in microcuvettes (*see* section 3.3.3). It is calculated that the [MgATP] is

1.0 - 1.5 mM with this ionic composition. With this saline, [Ca^{2+}] jumps up to 15 µM could be evoked. The release events measured with this solution were similar to those measured in the absence of MgATP (solution A).

3.4.2.2 [Ca^{2+}] *uncaging dynamics*

The time course of the [Ca^{2+}] after partial photolysis of the Ca^{2+} cage is shaped by multiple factors and has been minutely analyzed (Zucker, 1993; Ellis-Davies et al., 1996; Escobar et al., 1997). It mainly depends on the rate of conversion of the cage into its low affinity photoproducts, and the kinetic properties of the participating Ca^{2+} buffers including free, unphotolyzed cage and the Ca^{2+} indicator (*see* section 2.1.3). It is known that the liberated [Ca^{2+}] can rise quickly to elevated levels before it is buffered by the various buffers present. This situation generates an overshoot in [Ca^{2+}], known as 'Ca^{2+} spike', before it relaxes to a lower steady-state level. This spike can dramatically exceed the steady-state level resumed thereafter by the system. Even worse, it cannot be measured if it decays faster than the characteristic equilibration time of the Ca^{2+} indicator which is given by:

$$\tau = \frac{1}{k_{on,D}[\mathrm{Ca}^{2+}] + k_{off,D}} \tag{3.17}$$

The Ca^{2+} indicators used in this study were of low affinity and therefore had rapid response characteristics. However, they partially act as Ca^{2+} buffers and cannot track the dynamic [Ca^{2+}] changes that occur *before* they equilibrate with the new [Ca^{2+}] level, which is partially determined by the indicator itself. Fura-2-based low affinity indicators such as Mag-Fura-2 and Fura-2-FF have a Ca^{2+} association rate constant of ~5×10^8 $M^{-1} s^{-1}$, and relax to steady-state with time constants of 50 – 200 µs (Naraghi, 1997). Thus, Ca^{2+} spikes can occur during the first 100 – 200 µs, which cannot be detected fluorometrically. Therefore, one has to rely on kinetic simulations of the Ca^{2+} uncaging dynamics immediately following the UV pulse. This requires the knowledge of the kinetic rate constants of the participating Ca^{2+} buffers, which were taken from published values. A detailed model of the interaction of rapidly uncaged Ca^{2+} (and Mg^{2+}) with the prevalent buffers was therefore devised, which is described in section 2.1.3. It showed that a Ca^{2+} spike occurred during the first 100 µs after the UV pulse, whose relative amplitude mainly depended on the ionic composition. It is useful to define the 'Ca^{2+} spike ratio' as the ratio between the simulated spike amplitude and the simulated plateau [Ca^{2+}] level, which is fluorometrically measurable. In the experiments, the amplitude of the [Ca^{2+}] plateau was determined by averaging the measured [Ca^{2+}] in an interval that was defined by the 20% and 80% crossing levels

$[Ca^{2+}]_{measured}$	Interval (ms)		Ca^{2+} spike ratio		
(µM)	Start	End	Sol. A1/MF	Sol. A3/FF	Sol. B/FF
1	1	10	n.d.	n.d.	2.1
2	1.1	4.1	2.8	4.4	1.8
5	0.8	2.7	2.2	3.9	1.6
10	0.7	1.6	1.8	3.4	1.4
15	0.6	1.2	1.7	2.8	1.3
25	0.5	1	1.5	n.d.	n.d.
50	0.4	0.8	1.4	n.d.	n.d.
90	0.4	0.8	1.4	n.d.	n.d.

Table 3.3: Ca^{2+} spike ratios calculated for different internal solutions, according to the kinetic model of Ca^{2+} uncaging in section 2.1.3. The interval used to obtain average $[Ca^{2+}]$ amplitudes ($[Ca^{2+}]_{measured}$) is smaller for larger $[Ca^{2+}]$ jumps, because it was adapted to the rise time of the EPSC. The Ca^{2+} spike ratio is the peak amplitude of the modeled Ca^{2+} spike divided by the $[Ca^{2+}]_{measured}$. Ca^{2+} spike ratios were not determined (n.d.) for conditions not applicable in the present study.

of the simultaneously measured EPSC and therefore increased for smaller $[Ca^{2+}]$ jumps. Plateau $[Ca^{2+}]$ levels in simulations were calculated analogously, by averaging simulated $[Ca^{2+}]$ in the interval that corresponded to the analysis interval for a given $[Ca^{2+}]$ level in the experiment (Table 3.3). The Ca^{2+} spike ratio is also a function of the pulse energy, because the relaxation time constant of the indicator depends on the $[Ca^{2+}]$ reached, which is higher at higher pulse energies. For solution A1/Mag-Fura-2, the Ca^{2+} spike ratio was ≤ 2.8 and decreased for larger $[Ca^{2+}]$ jumps, whereas it could reach values of ≤ 4.4 for solution A3/Fura-2-FF. In contrast, with solution B/Fura-2-FF, the Ca^{2+} spike ratio was ≤ 2.1, which was mostly because of the high amount of free ATP (calculated 8-9 mM), which has a rapid Ca^{2+} association rate constant on the order of $\sim 1 \times 10^9$ M^{-1} s^{-1} (Eigen and Wilkins, 1965). Therefore, the comparison of release rates measured with solutions A/Fura-2-FF and B/Fura-2-FF gave important information on the possible influence of the Ca^{2+} spike on the release rate.

3.4.3 Implementation of a kinetic model for Ca^{2+} uncaging

As described in the previous section, it is necessary to calculate the evolution of the $[Ca^{2+}]$ by kinetic simulations of the Ca^{2+} uncaging and buffering reactions. This can be done if the respective kinetic rate constants are known. The main reactants in solution

A were DM-nitrophen and its photoproducts, the Ca^{2+} indicator and Ca^{2+}. For solution B, also the buffering action of ATP and phosphocreatine and the binding of these compounds to the divalent Mg^{2+} had to be taken into account. For the dissociation constants of these buffers, measured or published values were used in the model. Where possible, the association and dissociation rate constants were taken from the literature or otherwise assumed (*see* Table 3.4).

The general model of Ca^{2+} uncaging and buffering is described in a previous section (2.1.3). There, a proportion α of both the Ca^{2+}-bound and free form of DM-nitrophen are converted to an intermediate state (DM^*, $CaDM^*$) at time point t_0, which decay to the low affinity photoproducts of DM-nitrophen (DMp). Kinetic constants for this reaction have been measured by Ellis-Davies et al. (1996), and Escobar et al. (1997).

In a refined model (Fig. 2.3 b), the presence of Mg^{2+} was included as well as the buffering action of other compounds, i.e. ATP, phosphocreatine, and an endogenous buffer. A second, new feature of the more detailed model is the presence of two decaying pathways of the DM-nitrophen aci-nitro intermediates to the low affinity photoproducts. This is similar to a model of Ca^{2+} uncaging suggested by Ayer and Zucker (1999), in which the generation of two distinct photoproducts is predicted. In their model, DM-nitrophen complexed to Ca^{2+} decays to the low affinity photoproduct described in earlier studies, whereas a second photoproduct with slower Ca^{2+} binding and unbinding kinetics is formed by photolysis of free DM-nitrophen or DM-nitrophen bound to Mg^{2+}. However, since in the present study a slow $[Ca^{2+}]$ component was also observed in a Mg^{2+}-free solution with DM-nitrophen nearly completely saturated with Ca^{2+}, a model was preferred in which the two photoproducts are generated independently of the bound or unbound state.

The kinetic parameters of this model are specified in Table 3.4. To compare the modeled $[Ca^{2+}]$ time course with experimental traces, the modeled time course of the indicator-Ca^{2+} complex $[CaD](t)$ was converted to a simulated 'dye-reported' $[Ca^{2+}]_{measured}(t)$ according to the equation:

$$[Ca^{2+}]_{measured}(t) = K_D \frac{[CaD](t)}{[D]_{tot} - [CaD](t)} \quad . \tag{3.18}$$

This equation is derived from the calibration equations stated in section 3.4.1, which are valid only when the Ca^{2+}-indicator reaction is in chemical equilibrium. Therefore, Eq. 3.18 corresponds to the law of mass action for the Ca^{2+}-indicator reaction, but it underestimates the true $[Ca^{2+}]$ during the non-equilibrated phase. The modeled dye-reported $[Ca^{2+}]$ time course was then digitally filtered with a 4-pole RC filter (f_c =

	Ca^{2+}			Mg^{2+}			Reference
	k_{on} ($M^{-1} s^{-1}$)	k_{off} (s^{-1})	K_D (M)	k_{on} ($M^{-1} s^{-1}$)	k_{off} (s^{-1})	K_D (M)	
DM	30×10^6	0.15	5×10^{-9}	60×10^3	0.15	2.5×10^{-6}	Ca^{2+}: [1], [4] Mg^{2+}: [5]
DMp1	30×10^6	90×10^3	3×10^{-3}	60×10^3	180	3×10^{-3}	Ca^{2+}: [1], [4] Mg^{2+}: [5]
DMp2	0.3×10^6	900	3×10^{-3}	60×10^3	180	3×10^{-3}	Ca^{2+}: from present data Mg^{2+}: [5]
ATP	1×10^9	200×10^3	0.2×10^{-3}	10×10^6	1×10^3	0.1×10^{-3}	Ca^{2+}: [3], [8] Mg^{2+}: [3], [8]
PC	1×10^6	70×10^3	70×10^{-3}	1×10^6	50×10^3	50×10^{-3}	Ca^{2+}: [6] for K_D, $k_{on/off}$ were assumed Mg^{2+}: [6]
MF	750×10^6	23×10^3	31×10^{-6}	-	-	-	Ca^{2+}: [7] for k_{on}, K_D measured *in situ*
FF	550×10^6	4.9×10^3	8.9×10^{-6}	550×10^6	550×10^6	1	Ca^{2+}: [7] for estimated k_{on}, K_D measured *in situ*

Table 3.4: Kinetic parameters for simulations of the Ca^{2+} time course following laser flash photolysis. Abbreviations: DM: non-photolyzed DM-nitrophen, DMp1: photoproduct 1 with fast dissociation rate constant, DMp2: photoproduct 2 with slower dissociation rate constant, PC: phosphocreatine, MF: Mag-Fura-2, FF: Fura–2–FF.
References: [1] Ellis-Davies et al. (1996). [2] Escobar et al. (1997). [3] Klingauf and Neher, (1997). [4] Xu et al. (1997). [5] Ayer and Zucker (1999). [6] Fabiato and Fabiato (1979). [7] Naraghi (1997). [8] Baylor and Hollingworth (1998).

4.2 kHz, *see* section 3.1.1.4) and overlaid with experimental, ratiometrically determined $[Ca^{2+}]$ traces (Fig. 4.2).

The set of differential equations derived from the kinetic scheme depicted in Fig. 2.3 was programmed in Mathematica 3.0 (Wolfram Research, Illinois) and numerically solved. The fit was adjusted by variation of the photolysis efficiency α to obtain different $[Ca^{2+}]$ levels. The relative fraction of the fast and the slow photoproducts was empirically adjusted to β_1 = 0.8 (DMp1) and β_2 = 0.2 (DMp2) to match the measured data. This is somewhat different from the relative amplitudes of the two intermediate decay components reported by Ellis-Davies et al. (1996), which were 0.66 for the fast intermediate decay (decay rate constant $k_{p,1}$ = 80,000 s^{-1}) and 0.34 for the slower component ($k_{p,2}$ = 11,000 s^{-1}). Furthermore, the endogenous buffer(s) present in the presynaptic terminal were not taken into account because no

information is available about its kinetic properties. Certainly, the above model cannot fully predict the complex chemistry of DM-nitrophen photolysis and subsequent Ca^{2+} buffering, but it accounts for the main features of the measured [Ca^{2+}] time course. It furthermore agrees with the Ca^{2+} spike measurements published previously (Ellis-Davies et al., 1996; Escobar et al., 1997). Therefore, it is assumed with some confidence that the Ca^{2+} spike ratio is not appreciably underestimated in the present kinetic model.

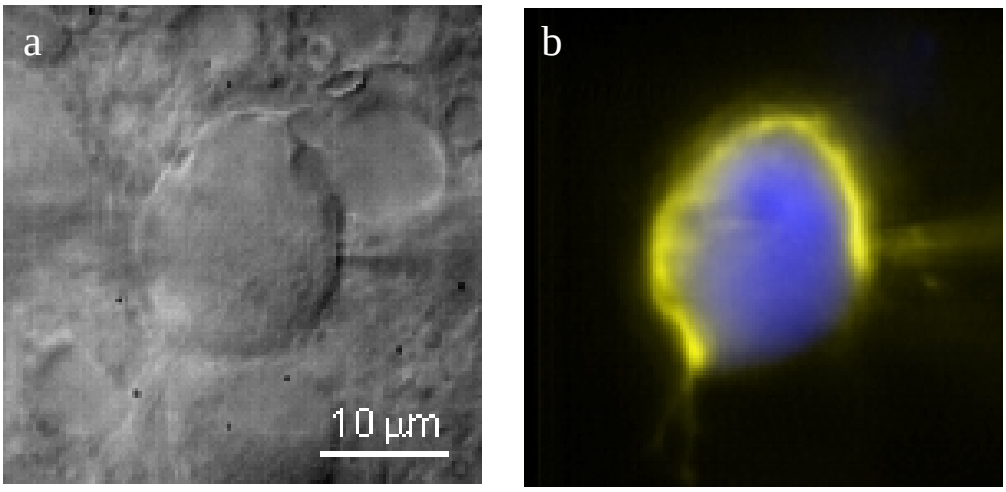

Fig. 4.1: Pre- and postsynaptic whole-cell recording of the giant synapse in the MNTB. (**a**) Video image of a giant synapse in the medial nucleus of the trapezoid body (MNTB). The pre- and postsynaptic recording pipettes are also weakly visible to the left and right of the synapse. (**b**) False color image of the presynaptic terminal (*yellow*) and the postsynaptic cell body (*blue*). The presynaptic terminal was stained with Mag-Fura-2 and the postsynaptic soma with Oregon-Green Bapta-5N. Images were taken with two different excitation wavelengths and later overlaid in Photoshop (Adobe, California). Adapted from Bollmann et al. (1998); image by Dr. F. Helmchen.

4. Results

The MNTB giant synapse is a large axo-somatic synapse in the auditory pathway of the brainstem. It can be visualized by infrared video microscopy, and both the pre- and postsynaptic compartments are electrically accessible with patch pipettes (Fig. 4.1). This favorable situation was used to measure the Ca^{2+} sensitivity of glutamate release with high temporal resolution.

In this chapter, the main findings are presented in three sections. First, the kinetics of rapid Ca^{2+} uncaging by laser photolysis were investigated under controlled conditions in microcuvettes. Second, quantal and compound glutamate release was characterized electrophysiologically at this type of synapse. And third, Ca^{2+} uncaging was applied to determine the dependence of glutamate release on the intracellular [Ca^{2+}] level, which is finally summarized in a kinetic model of Ca^{2+} binding and vesicle fusion. This model was used to obtain an amplitude estimate of transient [Ca^{2+}] elevations near releasable vesicles during action potential-evoked release.

4.1 Temporal analysis of [Ca^{2+}] uncaging in microcuvettes

4.1.1 Ca^{2+} uncaging in the presence of different Ca^{2+} buffers and indicators

Rapid release of Ca^{2+} from DM-nitrophen (DM-n) photoproducts was employed to evoke [Ca^{2+}] jumps of variable amplitude, which were used to challenge the releasable pool of vesicles in the MNTB giant synapse. Since a Ca^{2+} indicator of low affinity was co-loaded into the terminals, it was possible to directly measure the height of the [Ca^{2+}] jump briefly after the photolyzing laser pulse. To obtain estimates of what [Ca^{2+}] levels could be generated in the different solutions (*see* Table 3.1) and with different laser pulse energies, Ca^{2+} uncaging was first studied *in vitro* in small microcuvettes (Fig. 4.2). After subtraction of the background fluorescence and the pulse artifact, the evoked [Ca^{2+}] levels were reported by the Ca^{2+} indicators after ~200 µs. After this period, [Ca^{2+}] levels were detected that ranged between 2 and 100 µM with solution A1 and Mag-Fura-2, and between 0.5 and 15 µM with solutions A2, A3 and B and Fura-2-FF as the Ca^{2+} indicator (*see also* Fig. 3.10 c).

4.1.2 A refined model of Ca^{2+} uncaging with DM-nitrophen

The lag between the laser pulse and the plateau level of the dye-reported [Ca^{2+}] mainly originates from the finite association rate of the Ca^{2+} indicator, which is ~$5x10^8$ M^{-1} s^{-1} for Fura-2-based dyes. Therefore, these rapidly equilibrating indicators are too slow to report [Ca^{2+}] changes that are likely to occur during the first 100 - 200 µs (*see* section 3.4.2.2). Therefore, a detailed kinetic model was implemented to obtain estimates of the true [Ca^{2+}] time course that is expected after rapid laser photolysis (*see* section 2.1.3). The time course of [Ca^{2+}] increase during *in vitro* uncaging often exhibited not only a rapid component, much faster than the response time of the indicator, but also a slowly rising component (Fig. 4.2 a-c, Fig. 3.10 c). It

Fig. 4.2: Time course of Ca^{2+} uncaging. (**a**) [Ca^{2+}] jumps evoked by laser photolysis in solution A3, which contains no $MgCl_2$ or Na_2ATP. Fluorescence changes of the indicator, Fura-2-FF, were converted ratiometrically to [Ca^{2+}] (*noisy traces*). Model predictions of the [Ca^{2+}] time course as it is reported by the low affinity Ca^{2+} indicator are overlaid. Note the slow component of [Ca^{2+}] increase in the first three milliseconds. The photolyzed fraction α was 0.04, 0.128 and 0.179. The initial free [Ca^{2+}] was 170 nM (measured with Fura-2). (**b**) [Ca^{2+}] uncaging with solution B, containing $MgCl_2$ and Na_2ATP. The α's were 0.028, 0.0835 and 0.119. Initial free [Ca^{2+}] was 176 nM. (**c**) Ca^{2+} uncaging detected with Oregon-Green BAPTA-5N. →

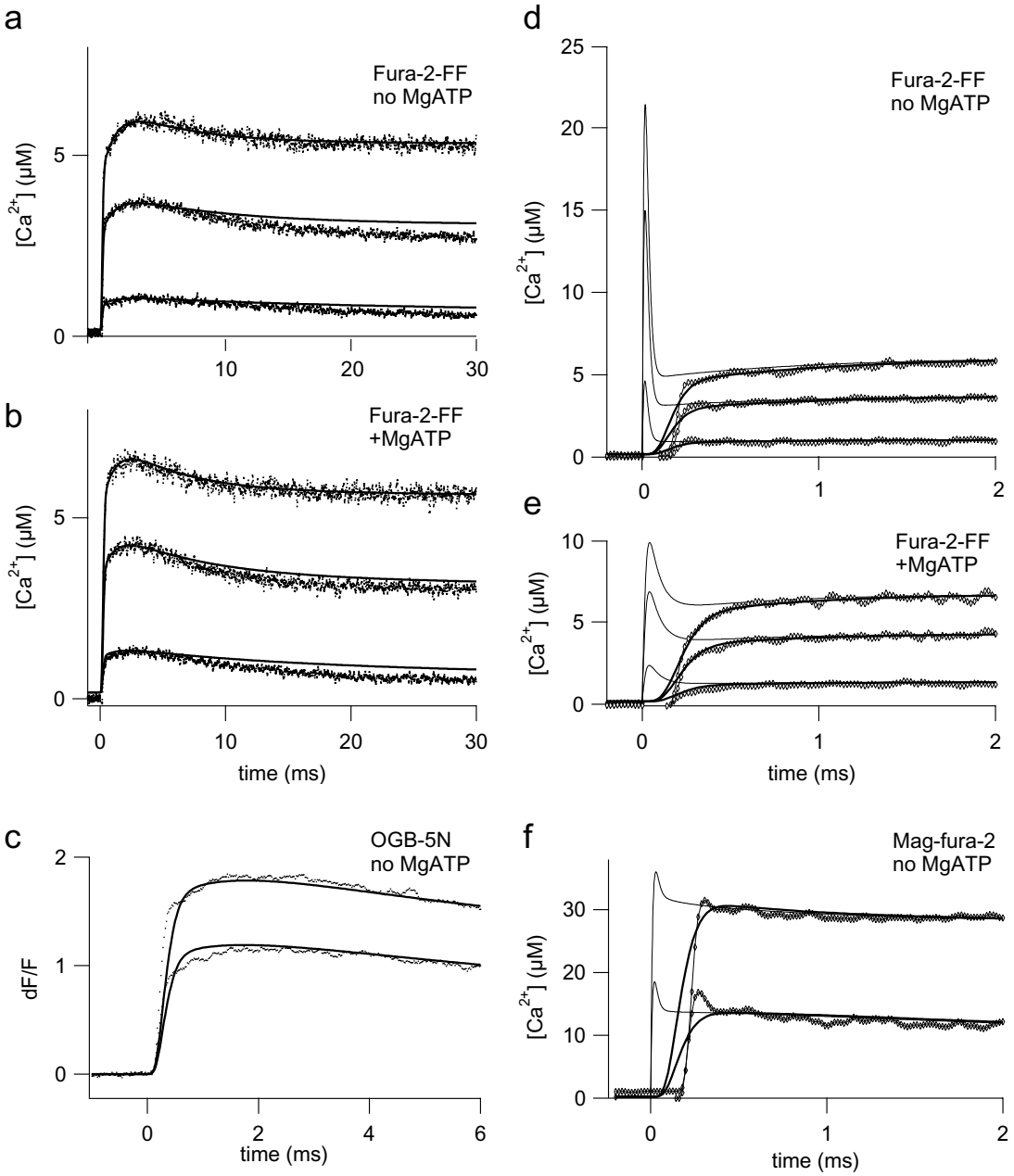

A slow component in $[Ca^{2+}]$ increase is also detected with this dye, indicating that it is not an artifact due to indicator bleaching. Model predictions are overlaid (*bold traces*; α = 0.024 and 0.036). (**d**) Same experiment as in (a), but on different scales. Here, diamonds indicate the experimental $[Ca^{2+}]$ time course, *bold traces* represent the predicted dye-reported $[Ca^{2+}]$, and *thin lines* represent the predicted true $[Ca^{2+}]$ time course, including the initial $[Ca^{2+}]$ spike. (**e**) Same experiment as in (b), with traces having the same meaning as in (d). Note that the amplitude of the predicted Ca^{2+} spike is much reduced compared to (d), because of the presence of ATP (10 mM). (**f**) Uncaging detected with Mag-Fura-2, which has a K_D ~3 fold larger than Fura-2-FF. Measured $[Ca^{2+}]$ (*diamonds*), modeled dye-reported $[Ca^{2+}]$ (*bold traces*), and back-calculated true $[Ca^{2+}]$ (*thin traces*) are overlaid. The initial Ca^{2+} overshoot is comparably small because of the lower affinity of Mag-Fura-2. Solution A1 was used, calculated α's were 0.083 and 0.0485.

was present both with dyes that show decreased fluorescence (Fura-2-based dyes), and those that show increased fluorescence (Oregon-Green Bapta-5N) when bound to Ca^{2+} (Fig. 4.2 a-c). This excluded the possibility that bleaching of the indicator was responsible for the slow increase in reported [Ca^{2+}]. Therefore, the model was refined by introducing a second decay pathway of DM-nitrophen that resulted in a photoproduct with 100-fold slower Ca^{2+} association and dissociation rate constants. This may be partially justified by the finding that intermediate decay of DM-nitrophen also follows a double exponential time course with similar relative amplitudes (McCray et al., 1992; Ellis-Davies et al., 1996). With this modification, predicted dye-reported [Ca^{2+}] time courses fit the experimentally observed ones much more closely under different buffer conditions (Fig. 4.2 a-f).

The model predicts the existence of a brief and transient overshoot of [Ca^{2+}], the 'Ca^{2+} spike' (Zucker, 1993; Ellis-Davies et al., 1996; Escobar et al., 1997), when not all Ca^{2+} buffers present are saturated to 100% with Ca^{2+}. As a measure of the amount of overshoot in [Ca^{2+}], the 'Ca^{2+} spike ratio' is calculated from model predictions (*see* section 3.4.2.2**,** Table 3.3). The Ca^{2+} spike ratio is smaller, the more DM-nitrophen is saturated with Ca^{2+}, but also if other rapid, low affinity Ca^{2+} buffers help damping the initial overshoot. In the studies designed to evoke large Ca^{2+} spikes (Ellis-Davies et al., 1996; Escobar et al., 1997), the Ca^{2+} spike ratios are much larger than in the present study, because in the latter the fraction of DM-nitrophen loaded with Ca^{2+} was approximately 95%, and a larger concentration of Ca^{2+} indicator was used (1 mM). Furthermore, in those sweeps in which ATP (10 mM) was included in the solution, the Ca^{2+} spike is damped because of the rapid Ca^{2+} binding kinetics of ATP (Eigen and Wilkins, 1965) (Fig. 4.2 b,e). The calculated effect of the Ca^{2+} spike on the release rate model is analyzed in section 5.2.1.3.

4.2 Electrophysiological characterization of glutamate release

As a measure of rapid synaptic glutamate release, postsynaptic currents were detected in the whole-cell configuration of the patch clamp technique. The following subsections describe the nature of the physiological compound EPSCs, and provide a characterization of the underlying quantal currents that result from the release of single transmitter packets from the presynaptic terminal.

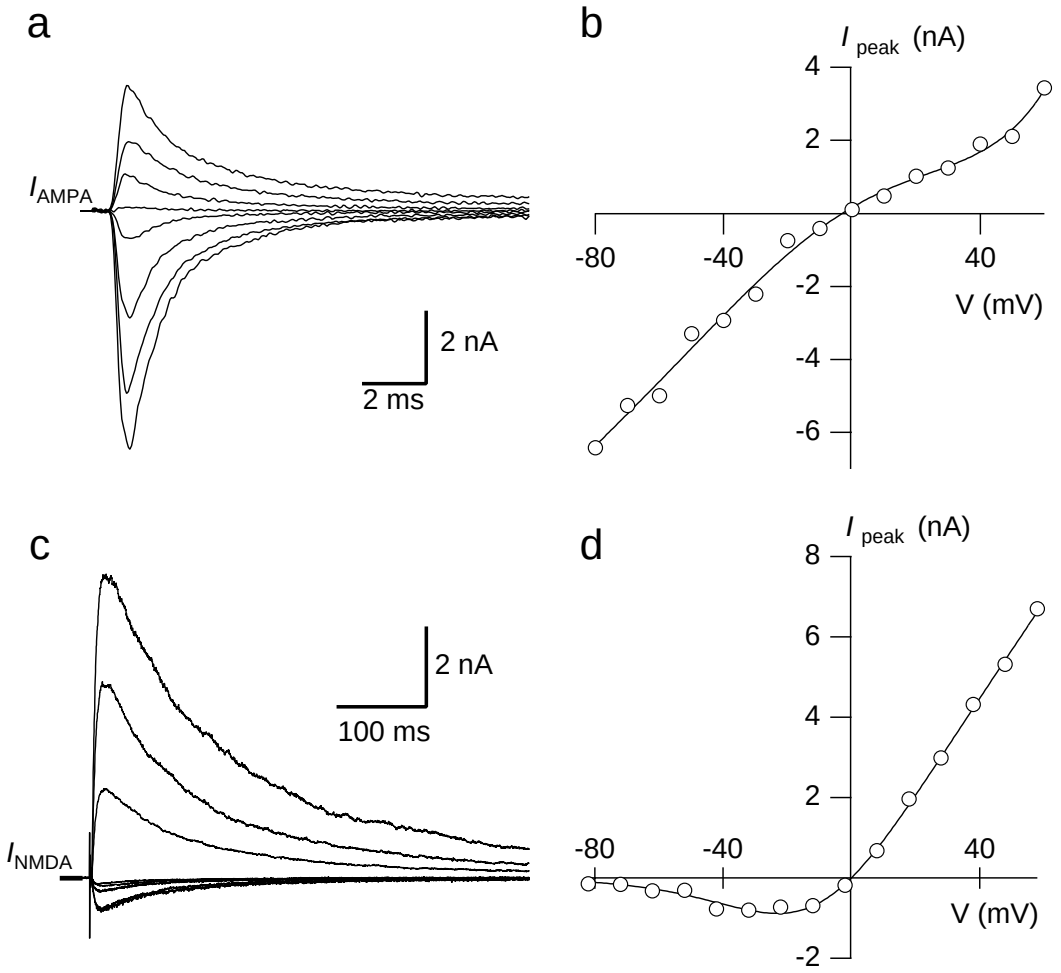

Fig. 4.3: AMPA and NMDA current-voltage relations. (**a**) Excitatory postsynaptic currents mediated by AMPA receptor channels, evoked by afferent stimulation. NMDA receptors were blocked by D-APV (50 µM). (**b**) Current-voltage relation of AMPA receptor channels. Current peak amplitudes are plotted versus the postsynaptic holding potential. (**c**) NMDA receptor-mediated EPSCs at different holding potentials. AMPA receptors were blocked by NBQX (10 µM). (**d**) As in (b). NMDA EPSC amplitudes exhibit outward rectifying behavior because of an external Mg^{2+}-dependent block, that is relieved at depolarized potentials.

4.2.1 Multi-quantal excitatory postsynaptic currents in the giant synapse

Glutamate release from the presynaptic terminal evokes EPSCs with dual time course in the postsynaptic neuron, which can be separated by pharmacological tools (Fig. 4.3). The released glutamate binds and activates ligand-gated receptor channels both of the AMPA and NMDA receptor type. Both current types are directed inwardly at negative postsynaptic membrane potentials and are carried mainly by Na^+, K^+ and Ca^{2+} ions. The AMPA current rises in less than 0.5 ms, and decays with fast and slow time constants of ~1 ms (92%) and ~14 ms, respectively (Borst et al., 1995; Bollmann et al., 1998). It exhibits a relatively linear current-voltage relation (Fig. 4.3 b). In

addition, it is characterized by a strong desensitization in the presence of sustained glutamate levels, which can be inhibited by addition of cyclothiazide (Trussell and Fischbach, 1989; Yamada and Tang, 1993; Otis et al., 1996a). The NMDA current has a slower time course; it peaks approximately 10 ms after the presynaptic release event, and decays with time constants of ~40 ms and ~150 ms (Barnes-Davies and Forsythe, 1995). It is characterized by an outwardly rectifying current-voltage relation in the presence of physiological concentrations of extracellular Mg^{2+} (Fig. 4.3 d). This is because NMDA receptor channels are blocked by Mg^{2+} at negative membrane potentials, while their conductance is increased ~100-fold at positive potentials due to a voltage-dependent relief of the Mg^{2+} block (Nowak et al., 1984; Mayer et al., 1984).

In order to detect the fast presynaptic release time course with a high bandwidth, the slowly-activating NMDA receptors were blocked with the competitive antagonist D-APV (50 µM). The rapidly responding AMPA receptors were used as postsynaptic detectors. However, since their marked desensitization to glutamate may mask slow release events, cyclothiazide (CTZ) was added in all experiments to reduce desensitization, thus improving the integrating behavior of the postsynaptic detector (Fig. 4.4 a). This improvement becomes particularly evident during high frequency stimulation (Fig. 4.4 b), when the recording in the presence of CTZ reveals ongoing phasic release after more than 10 action potentials, while the response in the absence of CTZ is largely desensitized.

The postsynaptic response to large, flash-evoked $[Ca^{2+}]$ jumps was often >20 nA at a holding potential of –80 mV, which saturated the patch clamp amplifier. Therefore, action potential and flash-evoked EPSCs were measured at a holding potential of –30 mV. To examine the dependence of the time course of the EPSCs on the holding potential, EPSCs were compared at –30 mV and –80 mV in the same terminal. The amplitudes of the EPSCs at these holding potentials scaled linearly with voltage, and their decay time constants (fit within 100 ms) were not significantly different. The 20-80% rise times were slightly, but not significantly, slower for the EPSCs at –30 mV (365 ± 19 µs at –30 mV versus 345 ± 23 µs at –80 mV, n = 7, paired t-test, $P > 0.05$). Subtraction of a scaled version of the EPSC measured at –80 mV from the EPSC measured at –30 mV revealed a slow inward current, whose time course resembled that of NMDA receptor-mediated synaptic currents. Its amplitude (10-20 ms after stimulation) was 6 ± 2 % (n = 7) of the peak amplitude of the action potential-evoked AMPA current (Fig. 4.4 d). It probably originated from an activity-dependent relief of the NMDA receptor block, and might in principle affect the deconvolution analysis of release rates, which is based on AMPA receptor-mediated miniature EPSCs.

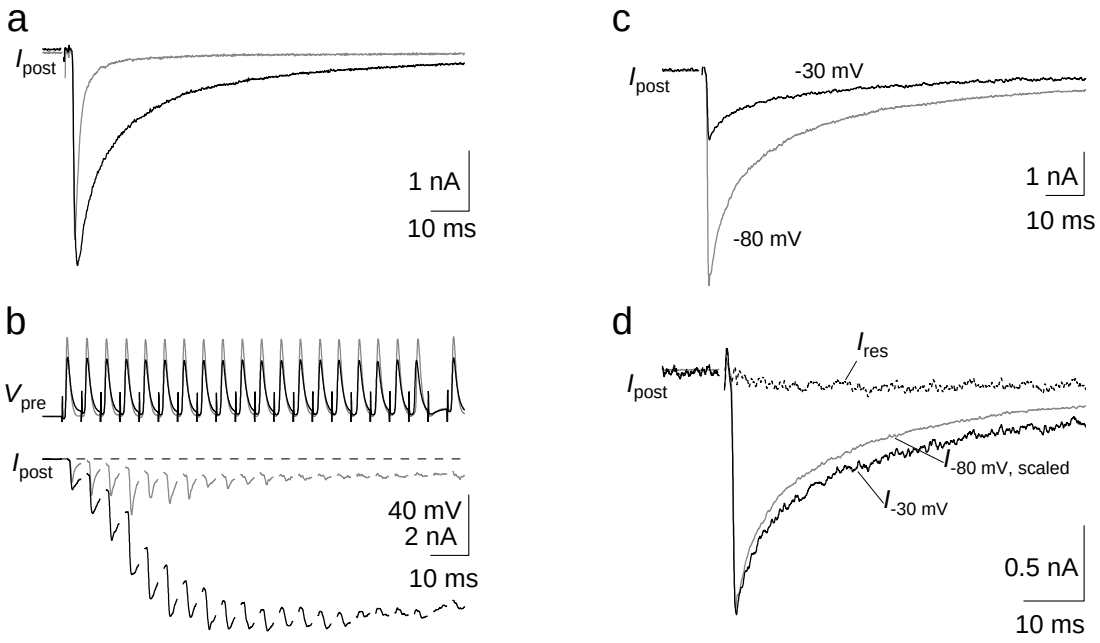

Fig. 4.4: Time course of AMPA receptor EPSCs. (**a**) EPSCs (V_{hold} = -80 mV) in the absence (*gray trace*) decay faster than in the presence of cyclothiazide (*black trace*, CTZ, 100 µM), which inhibits desensitization of AMPA receptors. (**b**) A train of presynaptic action potentials evokes a train of EPSCs of markedly increased amplitudes in the presence of CTZ. Thus, the release of glutamate is detectable also at later times in the train, whereas it is obscured in the absence of CTZ by desensitization. (**c**) Time course of AMPA EPSCs at –80 and –30 mV holding potential. (**d**) A small, slow inward current is revealed by subtraction of the scaled $EPSC_{-80\ mV,scaled}$ from the $EPSC_{-30\ mV}$ (*see text*). The time course within 100 ms of the EPSC was not significantly different for the two holding potentials. (All recordings in the presence of D-APV, 50 µM).

However, it developed very slowly compared to the AMPA EPSC and is therefore unlikely to appreciably distort the calculation of peak release rates, which are evaluated during the rapid rising phase of the AMPA current.

4.2.2 Miniature excitatory postsynaptic currents

Large compound EPSCs in the giant synapse are composed of many small quantal currents (Fatt and Katz, 1952; Borst and Sakmann, 1996). A quantal EPSC is generated by the amount of transmitter released from a single vesicle. In the absence of stimulation, miniature EPSCs (mEPSCs) are observed in the giant synapse, which most likely represent quantal EPSCs.

Spontaneous mEPSCs were measured in ten synapses, under the same conditions as the compound EPSCs (90-95% R_s compensation, 100 µM CTZ, 50 µM D-APV, 4-pole Bessel filter, f_c = 5 kHz, 50 kHz sampling frequency). The terminals were dialyzed with solutions A or B (Table 3.1), but no UV flash was applied. Therefore, the resting [Ca^{2+}] was likely below 0.5 µM, which is too low to evoke synchronous release, but may increase the probability of release of single (or sometimes two) quanta. The mEPSCs were identified by eye as rapid inward currents of ~15 pA or more amplitude. Because of the R_s compensation setting, the current noise level was relatively high (I_{rms} ≈ 9 pA), which may have prevented the detection of smaller amplitude mEPSCs. To obtain an average mEPSC for each of the 10 synapses, ca. 10 mEPSCs per synapse were consecutively aligned by maximizing their temporal overlap, and averaged (Fig. 4.5 a). Temporal overlap of any two mEPSCs was calculated by cross-correlation in an interval starting 1 ms before, and ending 4 ms after, the peak of the mEPSC. The average mEPSCs of individual synapses exhibited significant time course variability (Fig. 4.5 a), possibly because of different synaptic morphologies and recording conditions. These average mEPSCs were again aligned and averaged across synapses to obtain a 'standard' mEPSC (Fig. 4.4 b), which should approximate the size and time course of quantal EPSCs under average recording conditions. This mEPSC could be approximated with an analytical function (Eq. 3.4; Fig. 4.5 b, *top smooth line*). The fit had a peak value of –32 pA, a 20-80% rise time of 130 µs, and decayed bi-exponentially with τ_1 = 2.8 ms (54%), τ_2 = 7.5 ms. The amplitude distribution of the 102 individual mEPSCs has a mean value of -34 pA. A second, small peak at -55 pA may indicate that a minor fraction (< 20%) of the recorded mEPSCs were composed of two quanta. Despite the high R_s compensation, which was paid with an increased noise level, the rise time of the mEPSC is likely to be limited by the bandwidth of the whole-cell/headstage circuit (*see* section 3.1.2.2). Nevertheless, it is useful for reconstructing the rising phase of measured compound EPSCs, which were recorded under the same conditions. Furthermore, the amplitude of the standard mEPSC could be used to estimate the number of vesicles that can be released synchronously with a train of presynaptic action potentials. This is described in the next section.

4.2.3 Pool size estimate with EPSC trains

The absolute release rate of a synaptic terminal depends on the release kinetics of the individual vesicle *and* on the number of vesicles in a readily releasable state prior to stimulation. The size of this vesicle pool may be determined by the biochemical state

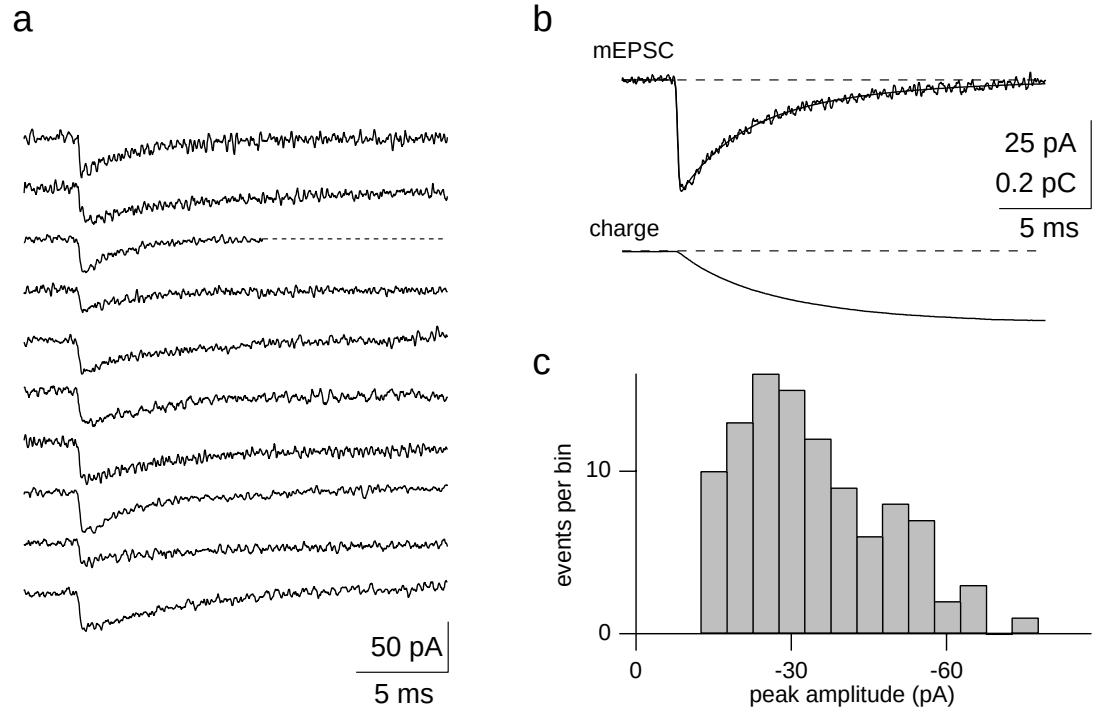

Fig. 4.5: Miniature EPSCs (mEPSCs) in the MNTB giant synapse. (**a**) mEPSCs recorded from ten different synapses (V_{hold} = -80 mV). Each trace is the average of ~10 mEPSCs, measured with 90-95% R_s compensation and aligned by temporal cross-correlation. (**b**) *Top*: Average mEPSC of the 10 mEPSCs shown in (a). Also shown, a fit with Eq. 3.4. *Bottom*:A charge of 0.16 pC is transferred by the mEPSC within 25 ms (*lower trace*). (**c**) Amplitude histogram of the 102 individual mEPSCs, which were averaged in (a),(b).

of the fusion machinery that promotes the fusion of a vesicle, but also by the spatial arrangement of vesicles relative to the sites of Ca^{2+} entry. In order to obtain an estimate of the number of vesicles in the readily releasable pool for a given synapse, the vesicle pool was first challenged with action potential-evoked Ca^{2+} influx during high frequency stimulation (afferent stimulation at 200 Hz, 200 ms, Fig. 4.6 a). The amplitudes of the EPSCs in a train (measured from the local minimum of the EPSC to the preceding local maximum, 'peak-to-peak amplitude') decreased quickly to a small steady-state value after about 10 stimuli, which is probably because the number of readily releasable vesicles was exhausted (von Gersdorff et al., 1997). The size of the readily releasable vesicle pool was evaluated by summing the peak-to-peak amplitudes of the EPSCs in a train, yielding the 'cumulative EPSC amplitude'. Since the depletion of the readily releasable pool is counteracted by a refilling process (Wu and Borst, 1999), the cumulative EPSC amplitude at the end of the train does not only reflect the number of vesicles initially available at the start of the train, but also those made available during the train. To correct for this mixture of vesicle pools, it was assumed that the refilling mechanism proceeds at a constant rate and can be

subtracted by fitting a straight line to the last 20 points of the cumulative EPSC amplitude, which is back-extrapolated to the beginning of the stimulus train. The intersection of the straight line fit with the y-axis was taken as the initial size of the releasable pool (Fig. 4.6 b) in the absence of vesicle refilling (Schneggenburger et al., 1999), specified as a current amplitude. The cumulative EPSC amplitude was -9.7 ± 0.7 nA (mean ± SEM, n = 43). To convert it to the number of vesicles available in the initial pool, it was assumed that each vesicle contributes –12 pA to the cumulative EPSC amplitude, which is the amplitude of the standard mEPSC scaled to a holding potential of –30 mV. Thus, the initial pool size was estimated to consist of 810 ± 60 vesicles, in agreement with earlier estimates (Schneggenburger et al., 1999; Wu and Borst, 1999).

The first EPSC in a train had an amplitude of 1.9 ± 0.2 nA (n = 43). This could be compared to the cumulative EPSC amplitude for the same terminal. The first EPSC amplitude in a train was 21 ± 2% (n = 43) of the cumulative EPSC amplitude. Taking the decay of the quantal EPSCs during the rising phase of the compound EPSC into account, this means that approximately 25% of the readily releasable vesicle pool is depleted during a single action potential. The first EPSC in a train was further characterized by its rise time and peak release rate. The 20-80% rise time was 424 ± 11 µs and the peak release rate (*see* section 3.2) was 337 ± 28 ms^{-1} for the whole terminal, or 0.42 ± 0.04 ms^{-1} (n = 43) when divided by the number of vesicles in the releasable pool.

Following the estimation of the pool size in the intact terminal, the terminal was dialyzed with a presynaptic solution (A or B, Table 3.1) and a UV laser pulse was applied to induce a jump in [Ca^{2+}] (Fig. 4.6 c). This evoked an EPSC of variable size and speed, depending on the [Ca^{2+}] reached after the pulse. For [Ca^{2+}] jumps to more than ~10 µM, the laser-evoked EPSC amplitude approached the cumulative EPSC amplitude measured in the same terminal (Fig. 4.6 d). This suggests that the two stimuli activated the release of the same vesicle pool.

In a different set of experiments it was analyzed whether the size of the readily releasable vesicle pool is changed under whole-cell patch clamp conditions when the intracellular solution is exchanged. Cumulative EPSC amplitudes in response to afferent stimulus trains were measured in the intact and dialyzed terminal and compared (not shown). The cumulative EPSC amplitude of the first afferent stimulation measured 3 - 11 minutes after presynaptic break-in was not significantly different from that measured in the same, intact terminal (n = 5; paired t-test, $P>0.05$), suggesting that the size of the readily releasable pool was not decreased.

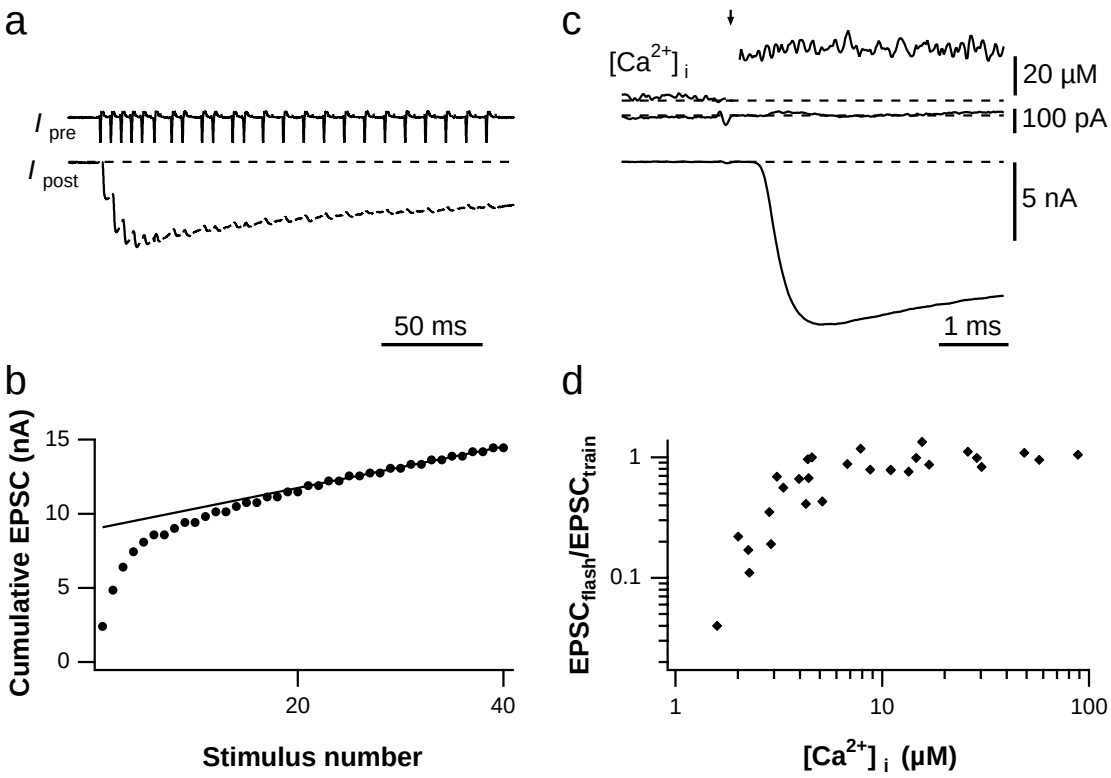

Fig. 4.6: Comparison of vesicle pools released by afferent stimulation and laser flash photolysis in the same terminals. (**a**) A train of EPSCs, evoked by afferent stimulation (200 Hz), is used to estimate the releasable vesicle pool size of the intact terminal. The presynaptic pipette is in the cell-attached mode. Stimulus artifacts were removed. (**b**) The peak-to-peak amplitude of the individual EPSCs shown in (a) was summed (cumulative EPSC) and plotted versus the stimulus number. A straight line is fit to the steady-state component of release and back-extrapolated to the beginning of the train to estimate the initial pool size. (**c**) After dialysis of the terminal with caged Ca^{2+}, a UV flash (*arrow*) induces a jump in $[Ca^{2+}]$ (*upper trace*) which evokes a rapid, large EPSC (*lower trace*). Its amplitude is close to that of the cumulative EPSC measured by afferent stimulation in the same terminal. The presynaptic current (*middle trace*) remains nearly constant. Vertical scale bars in (c) also apply to (a). (**d**) A plot of the EPSC peak amplitude evoked by $[Ca^{2+}]$ jumps normalized to the cumulative EPSC amplitude measured in the same terminals. Data of 26 experiments.

During multivesicular release, accumulation of glutamate in the synaptic cleft may lead to prolonged activation and saturation of AMPA receptors (Tang et al., 1994; Otis et al., 1996b; Silver et al., 1996; Neher and Sakaba, 2001). These mechanisms may partially account for the build-up and decay of a slow component of the EPSC train during high frequency stimulation. On the other hand, a comparison of the EPSC train and the laser-evoked EPSC (Fig. 4.6 a,c) reveals that the latter has a roughly two-fold larger peak amplitude than the maximal current amplitude during the train

(occurring at the fourth EPSC in the train). This indicates that, during the EPSC train, the decline in the peak-to-peak amplitude is probably not a result of considerable postsynaptic receptor saturation (*see* section 5.2.2.2).

Estimating the synapse-specific pool size has several advantages. Firstly, the pool size and the Ca^{2+} sensitivity of this pool determined later in the course of the experiment is measured in the same terminals. This can be used to normalize release rates to the *average* pool size, thus reducing the considerable cell-to-cell variability of the readily releasable pool (coefficient of variation ~0.5). Secondly, the pool size and the Ca^{2+} sensitivity were determined in a subset of synapses that were previously challenged by afferent stimulation at frequencies typical for the auditory pathway (Rhode and Smith, 1986; Spirou et al., 1990). It was therefore evaluated in terminals which had an intact axon and which were already capable of high frequency transmission, which is a property developing during this age (Taschenberger and von Gersdorff, 2000). On the other hand, the peak-to-peak amplitude summation does not take the more asynchronous release following the phasic release period into account. The present estimate should therefore be regarded as an estimate for the size of a vesicle pool that can be released in tight temporal synchrony with the presynaptic Ca^{2+} influx following an action potential. More vesicles may be releasable with slower kinetics, responding to the elevated $[Ca^{2+}]$ levels following the decay of the local Ca^{2+} transient. This, in fact, has been described recently by Sakaba and Neher (2001b). The present study focuses on the (ideally) homogeneous vesicle pool released phasically with an action potential.

4.3 $[Ca^{2+}]$ dependence of glutamate release

4.3.1 Glutamate release evoked by UV-induced $[Ca^{2+}]$ jumps

Laser flash photolysis of the caged Ca^{2+} compound DM-nitrophen was used to explore the dependence of the kinetics of glutamate release on the intracellular free $[Ca^{2+}]$. To this end, solutions containing a mixture of the DM-nitrophen-Ca^{2+} complex and of a low affinity Ca^{2+} indicator (Mag-Fura-2 or Fura-2-FF, *see* Table 3.1) were dialyzed into the presynaptic terminal via the patch pipette. After a loading period of four to six minutes, a UV pulse from a frequency-tripled Nd:YAG laser was applied to a region containing the terminal. This pulse evoked a rapid jump in $[Ca^{2+}]$, which elicited an EPSC of variable size and time course, depending on the $[Ca^{2+}]$ level attained after the pulse (Fig. 4.7). The rapid photodiode system permitted recording of

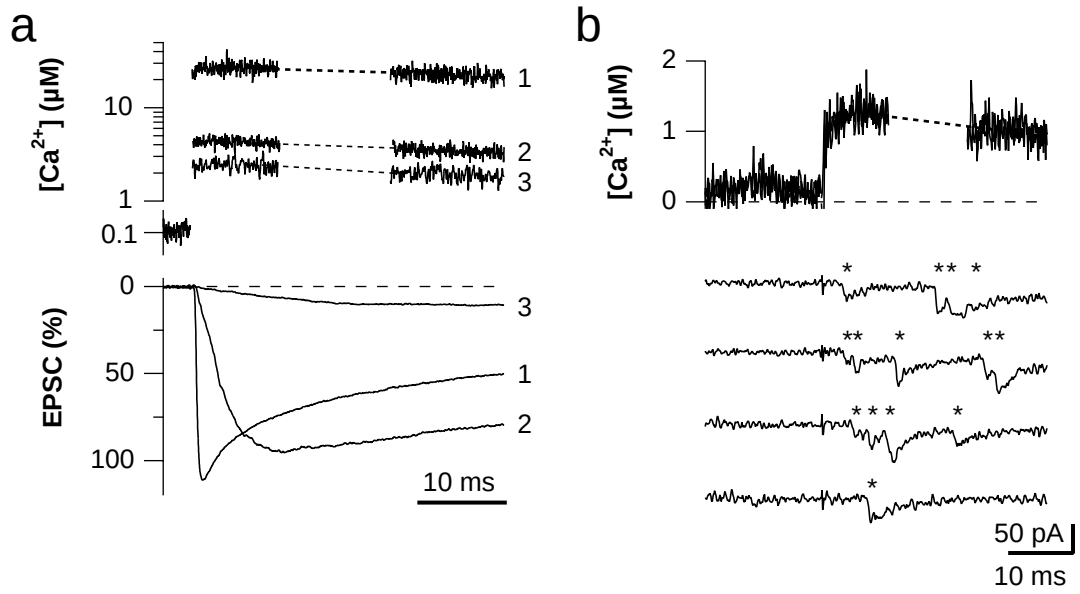

Fig. 4.7: Time course of EPSCs evoked by [Ca $^{2+}$] jumps of different amplitudes. (**a**) [Ca^{2+}] jumps between 2 and 30 µM were evoked in three different synapses (*top panel*). The evoked EPSCs, normalized to the respective cumulative EPSC amplitude, exhibited a strong dependence on the [Ca^{2+}] level between 2 and 10 µM. (**b**) Four subsequent [Ca^{2+}] jumps to around 1 µM were evoked in one terminal. The first and the last of the four [Ca^{2+}] jumps are shown (*upper panel*). They evoked a train of mEPSCs (*four lower traces*). Putative quantal release events are marked by asterisks.

the Ca^{2+}-related fluorescence before the onset of the EPSC (Fig. 4.6 c). The fluorescence record could not report the brief [Ca^{2+}] spike occuring before the steady-state concentration level, because it occurs before Ca^{2+} is bound to the indicator (*see* section 3.4.2.2). The presynaptic current recording usually exhibited only a small and slow current component, whose onset occurred after the onset of the EPSC. This indicates that the laser-evoked [Ca^{2+}] jump, rather than presynaptic Ca^{2+} channels, caused the postsynaptic current. When the [Ca^{2+}] jump exceeded ~10 µM, the rise time of the laser-evoked EPSCs was usually faster, and the amplitude larger, than that of action potential-evoked EPSCs. This indicates that action potential-driven release does not act at the maximal release rate possible. To determine the intrinsic dependence of glutamate release on presynaptic [Ca^{2+}], the UV pulse energy was varied systematically, and peak release rates and synaptic delays were calculated from the resultant EPSCs.

4.3.2 [Ca^{2+}] dependence of rates and delays of glutamate release

[Ca^{2+}] jumps were evoked in a range between 0.5 and 100 µM in presynaptic terminals (Fig. 4.7; Fig. 4.8). The measured EPSCs were normalized to the size of the

readily releasable pool measured prior to dialysis of the presynaptic terminal. Regarding their amplitude and rise time, the measured EPSCs exhibited a strong dependence on the [Ca^{2+}] in the range between 0.5 and 10 µM. The 20-80% rise time decreased from >5 ms to <0.25 ms, when the measured [Ca^{2+}] increased from 2 to 30 µM. For [Ca^{2+}] jumps larger than 30 µM, the rise time became minimal at a value of 220 ± 12 µs. This value is significantly slower than the rise time of the averaged mEPSC, and is therefore not limited by the bandwidth of the recording system (*see* section 3.1.2.2). When [Ca^{2+}] jumps between 0.5 and 1.5 µM were elicited, a train of individually resolvable mEPSCs could be detected. For compound glutamate release, usually only the first laser-evoked EPSC was taken for analysis, because the subsequent flashes evoked EPSCs of slower rise time and smaller amplitude. For quantal release events, 3 to 5 sweeps were taken for analysis.

The compound EPSCs were fit by a routine to evaluate the underlying vesicle release rates (section 3.2). The peak release rates were divided by the estimated number of vesicles in the readily releasable pool of the same synapse to express the release rate as a vesicle-inherent quantity. The resulting value was plotted versus the measured [Ca^{2+}], which was averaged in the interval between the 20% level and the 80% level of the EPSC (Fig. 4.8 a). The peak release rates exhibited a power relation on the intracellular [Ca^{2+}] which was steepest in the range 0.5 and 5 µM. A straight line fit to the release rate-[Ca^{2+}] relation after logarithmic transformation has a slope of 4.4 ± 0.3 (*not shown*). At [Ca^{2+}] greater than 30 µM, the release rates reach a maximum of 5.9 ± 0.4 ms^{-1} per vesicle.

Also, the synaptic delays were strongly dependent on the [Ca^{2+}] levels reached after the photolyzing UV pulse (Fig. 4.8 b). They were shortest for [Ca^{2+}] levels larger than 30 µM (0.27 ± 0.02 ms, corrected for an estimated filter delay of 0.1 ms, *see* section 3.1.2.2), and had a duration of several milliseconds for [Ca^{2+}] jumps to ~1 µM. This demonstrates that the glutamate release mechanism in the Calyx of Held synapse has a relatively high Ca^{2+} sensitivity, which allows it to effectively respond to [Ca^{2+}] levels between 1 and 10 µM.

For the understanding of rapid synaptic transmission, it is desirable to estimate the physiological [Ca^{2+}] transient that activates the glutamate release sensor during action potential-evoked Ca^{2+} influx. Under this condition, the [Ca^{2+}] transient is much more localized and short-lived than under the conditions of laser photolysis. To this end, a model of the reaction of Ca^{2+} binding to the release sensor and of the activation of the fusion reaction was devised, which will be described in the following section.

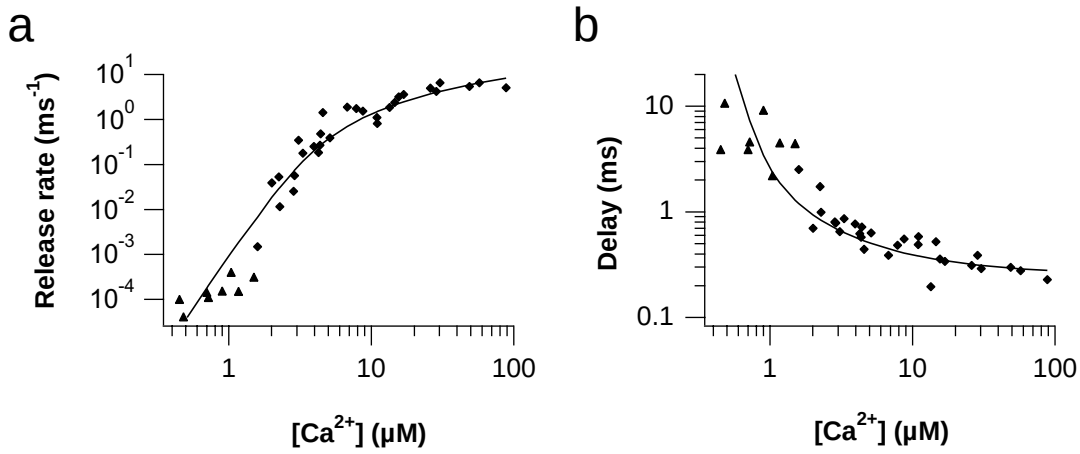

Fig. 4.8: Relation between intracellular [Ca^{2+}] and the rate of glutamate release at the Calyx of Held synapse. (**a**) Summary of the dependence of peak release rates on [Ca^{2+}], displayed on log-log coordinates. Peak release rates of compound EPSCs (*diamonds*) were corrected for the finite rise time of the average mEPSC (*see* section 3.2). For [Ca^{2+}] jumps <1.5 µM, the average mEPSC rate (*triangles*) was analyzed during the 20 ms following the mean first latency in 3-5 sweeps per experiment. The *solid line* is derived from a model that included five sequential Ca^{2+} binding steps followed by the activation of the calcium sensor (*see text*). Release rates are specified per vesicle. Pooled data of 31 synapses. (**b**) The [Ca^{2+}] dependence of the delays between the laser pulse and the onset of release. The onset of compound release (*diamonds*) was defined as the time when the EPSC intersected a threshold of -35 pA; the onset of quantal release (*triangles*) was defined as the mean first latency of the mEPSCs. The mean delay predicted by the model between the [Ca^{2+}] jump and the release of the first transmitter quantum is shown as *solid line*. 250 µs were added to the simulated delays in order to match the experimental data (*see* section 5.2.1.3).

4.3.3 Kinetic model of glutamate release

4.3.3.1 *Release promoter model with five Ca^{2+} binding steps*

The Ca^{2+} sensitivity of glutamate release was described in a kinetic model. This was done mainly for two reasons. Firstly, the model may define limits regarding the expected Ca^{2+} binding and unbinding rates of the Ca^{2+} sensor and thus its Ca^{2+} affinity. This may help in identifying possible candidates for Ca^{2+} sensor molecule(s), which play a key role in excitation-secretion coupling during rapid synaptic transmission. Secondly, a model of glutamate release is required when the expected release evoked by more complex [Ca^{2+}] time courses is to be investigated. This is the case when, for example, the amplitude of an idealized, 'typical' [Ca^{2+}] transient is to be calculated, which is assumed to be generated near releasable vesicles by the short opening of Ca^{2+} channels during presynaptic action potentials.

The data in Fig. 4.8 (a,b) could be described satisfactorily with a model featuring five identical Ca^{2+} binding steps and a final, Ca^{2+}-independent fusion step (*see* section 2.3). Our model was inspired by that of Yamada and Zucker (1992, their scheme II), in which a release-promoting molecule could switch between an active and an inactive state; in their model, the rate of release was proportional to the fraction of release promoters residing in an activated state. Five Ca^{2+} binding steps were required to model the steep slope of the release rate dependence on $[Ca^{2+}]$ in the range from 0.5 to 5 µM. It was possible to simulate the steep Ca^{2+} dependence for $[Ca^{2+}]$ lower than 10 µM and the relatively rapid saturation of release rates for $[Ca^{2+}]$ higher than 10 µM with five *identical* Ca^{2+} binding steps, if depletion of the vesicle pool was taken into account. Stated in more detail, the release of a fixed number of vesicles (readily releasable pool size) could occur with a variable rate constant; the rate constant was proportional to the occupancy of the activated release promoter. This activated state could only be reached if the release promoter had previously bound five Ca^{2+}. The Ca^{2+} binding step was modeled to have a k_{on} of 3×10^8 $M^{-1}\,s^{-1}$ and a k_{off} of 3,000 s^{-1}, corresponding to a dissociation constant of K_D = 10 µM. The rate of rise and the decay of release probability were largely determined by the Ca^{2+}-independent activation and inactivation steps of the release promoter (*see* section 5.3.1.1).

It should be noted that due to the great number of possible reaction schemes and parameters, the above model is not unique. The stated parameters were not optimized with, for example, a χ^2-minimization of the modeled and experimental data. We also simulated the experimental data with models previously used to describe the Ca^{2+} dependence of transmitter release in other synapses. For example, a sequential Ca^{2+} binding model, in which the affinity for Ca^{2+} successively increases with each additional bound Ca^{2+} ion (Heidelberger et al., 1994; Schneggenburger and Neher, 2000) was similarly successful in describing the data, when the Ca^{2+} binding and unbinding rates were adjusted appropriately (not shown). However, we preferred the model description stated above, for several reasons. Firstly, it does not require Ca^{2+} binding steps of increasing affinity, where the first step has a high dissociation rate constant and is therefore rather insensitive to modulation by the basal $[Ca^{2+}]$ levels. Secondly, the time course of release is determined by the activation and inactivation rate constants of the release promoter, rather than by the Ca^{2+} binding kinetics; it is therefore relatively independent of the size of the $[Ca^{2+}]$ domain, which is also observed experimentally (Yamada and Zucker, 1992; *see also* next section and section 5.3.1.1). Thirdly, the present model incorporates the concept of a release promoter, whose occupancy determines the release rate constant of the releasable vesicle pool. Thus, the model can principally account for the case that the fusion of a single vesicle may

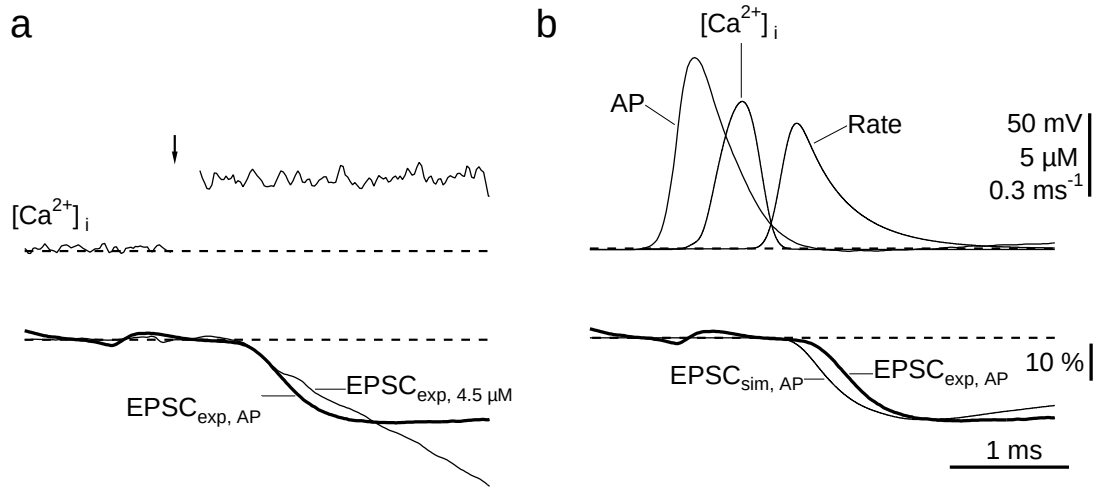

Fig. 4.9: A comparison of release rates following action potentials and $[Ca^{2+}]$ jumps. (**a**) A step elevation of $[Ca^{2+}]$ to 4.5 µM, (*top trace*) evoked an EPSC ($EPSC_{exp, 4.5\ \mu M}$, *bottom panel*) that rises almost as fast as an action potential-evoked EPSC ($EPSC_{exp, AP}$). The action potential-evoked EPSC was aligned such that the putative peak of the Ca^{2+} current coincided with the $[Ca^{2+}]$ jump (*arrow*). Calibration bars are shown in (b). (**b**) Simulation of EPSCs evoked by a brief increase in the $[Ca^{2+}]$. The time course of the $[Ca^{2+}]$ transient was assumed to be the same as that of the measured Ca^{2+} current during an action potential (*top traces*). It was scaled and used to drive the kinetic release model to produce an EPSC ($EPSC_{sim, AP}$) of the same amplitude as observed during action potential-evoked release. A peak $[Ca^{2+}]$ transient of <10 µM was sufficient to simulate action potential-driven release. The simulated EPSC was shifted to the right by 250 µs (*see* section 5.2.1.3).

be promoted by several release promoting molecules. This is an attractive hypothesis when considering the likelihood that a vesicle may contain more than one (SNARE or other) protein complexes that may function as the vesicle's release machinery.

4.3.3.2 *Estimate of* $[Ca^{2+}]$ *during presynaptic action potentials*

Next, the question was addressed how the typical $[Ca^{2+}]$ transient near releasable vesicles can be described for action potential-evoked release.

A simple comparison of release rates observed during laser-evoked $[Ca^{2+}]$ jumps and during afferent stimulation suggests that the required $[Ca^{2+}]$ during action potential-evoked release is probably much lower than the hundreds of micromolar suggested previously (Fig. 4.9 a). Since the action potential-evoked $[Ca^{2+}]$ transients have a much faster decay, they are probably less efficient in triggering release than $[Ca^{2+}]$ jumps to the same levels. Therefore, the Ca^{2+} sensor model was used to obtain an

estimate of the [Ca^{2+}] transient amplitude when the time course of the [Ca^{2+}] transient was rapidly decaying, as expected for physiological [Ca^{2+}] transients.

It is likely that a vesicle is triggered by the overlapping [Ca^{2+}] domains of several Ca^{2+} channels, because it was found previously in this synapse that a reduction in the open probability of Ca^{2+} channels leads to a supra-linear decrease of the release probability (Borst and Sakmann, 1999b). This indicates that the step-like nature of single channel currents is smoothed by the stochastic opening of several channels, and does not dominate the time course of the [Ca^{2+}] transient near the vesicle (Meinrenken and Sakmann, 2001). Therefore, it appears justified to approximate the time course of the [Ca^{2+}] transient near a synaptic vesicle by the time course of the whole-cell Ca^{2+} current, which was measured previously (Borst and Sakmann, 1998). The Ca^{2+} current time course was calculated using a Hodgkin-Huxley model, as described by Borst and Sakmann (1998). The Ca^{2+} current time course was used as a template for the local [Ca^{2+}] transient near the Ca^{2+} sensor of release. It was scaled and used to drive the vesicle release model such that the amount of release matched the quantal content experimentally observed during a single action potential (Fig. 4.9 b). Simulated EPSCs were calculated by convolution of release rates predicted by the release sensor model with the time course of the standard mEPSC.

When the Ca^{2+} sensor model was operated with a [Ca^{2+}] transient that had a peak amplitude of 9 µM, it predicted an EPSC of 20% normalized amplitude, very similar to the experimentally observed average value. This indicates that most vesicles do not experience [Ca^{2+}] transients with amplitudes of hundreds of micromolar because, in that case, the quantal content of action potential-evoked release would be much larger than that observed experimentally.

It should be noted that the distance between vesicles and Ca^{2+} entry sites is probably distributed in a certain interval, and is not the same for all releasable vesicles. This means that the typical [Ca^{2+}] transient for which the above estimate was calculated is probably not what most vesicles see during an action potential. While some vesicles located close to Ca^{2+} entry sites may indeed experience a [Ca^{2+}] transient peak of several tens or hundreds of micromolar, many other vesicles experience [Ca^{2+}] transients lower than the 9 µM stated above. It was shown recently that a hypothetical arrangement of vesicles distributed randomly over a range of distances from a distinct Ca^{2+} entry site provides a good description of many release characteristics observed experimentally at this synapse (Meinrenken and Sakmann, 2001). Based on their detailed simulations that take into account the Ca^{2+} sensitivity of release described here, the authors conclude that the [Ca^{2+}] transient amplitude seen by the majority of vesicles docked to an active zone does not exceed 10 µM.

4.3.3.3 *Dependence of EPSCs on extracellular* [Ca^{2+}]

The release model was further tested regarding its suitability to predict other experimental findings at the MNTB giant synapse. It has often been reported that the time course of release probability during action potential-evoked release is not very sensitive to the external [Ca^{2+}] (Datyner and Gage, 1980; Parnas et al., 1986; Yamada and Zucker, 1992; Borst and Sakmann, 1996). We tested the behavior of our model by varying the amplitude of the [Ca^{2+}] transients. More precisely, the amplitude was scaled according to the relationship between Ca^{2+} influx and the external [Ca^{2+}], because Ca^{2+} influx partially saturates for external [Ca^{2+}] larger 2 mM (Schneggenburger et al., 1999). The predicted release rates and modeled EPSCs are shown in Fig. 4.10 (a). A comparison of the time course of the release rate at 0.25 and 2 mM external [Ca^{2+}] shows that the time course of the release probability is almost invariant at these external [Ca^{2+}] levels (Fig. 4.10 b). In addition, it is in good agreement with the time course of release probability measured in the Calyx of Held synapse (Borst and Sakmann, 1996).

The 20-80% rise times and the delays of the modeled EPSCs exhibited a very low Ca^{2+} dependence when external [Ca^{2+}] was below 2 mM, but decreased for larger external [Ca^{2+}]. A Hill-type fit to the relation between the normalized peak amplitude of the modeled EPSCs and the normalized Ca^{2+} influx yielded a maximal potentiation factor A_{max} of 4.8, a power n of 3.8 and a half-maximal value K of 1.4 (Fig. 4.10 c), compatible with the measured relation in this synapse (A_{max} = 5.4, n = 3.5 and K = 1.5; Schneggenburger et al., 1999). Taken together, the present model is able to predict many features of glutamate release in the Calyx of Held at this developmental stage, both during action potential-evoked [Ca^{2+}] transients and during laser-evoked [Ca^{2+}] jumps. Major refinement of the model may be expected when (use-dependent) replenishment of the releasable pool size and possible inhomogeneities of the vesicles' Ca^{2+} sensitivity, which may have remained undetected to now, are taken into account. For example, cyclic AMP may facilitate presynaptic glutamate release by increasing the number of vesicles in the readily releasable pool (Sakaba and Neher, 2001a). Another possible mechanism of regulating the release probability may be the presynaptic [Ca^{2+}] levels prior to the stimulation. This will be analyzed in the next section.

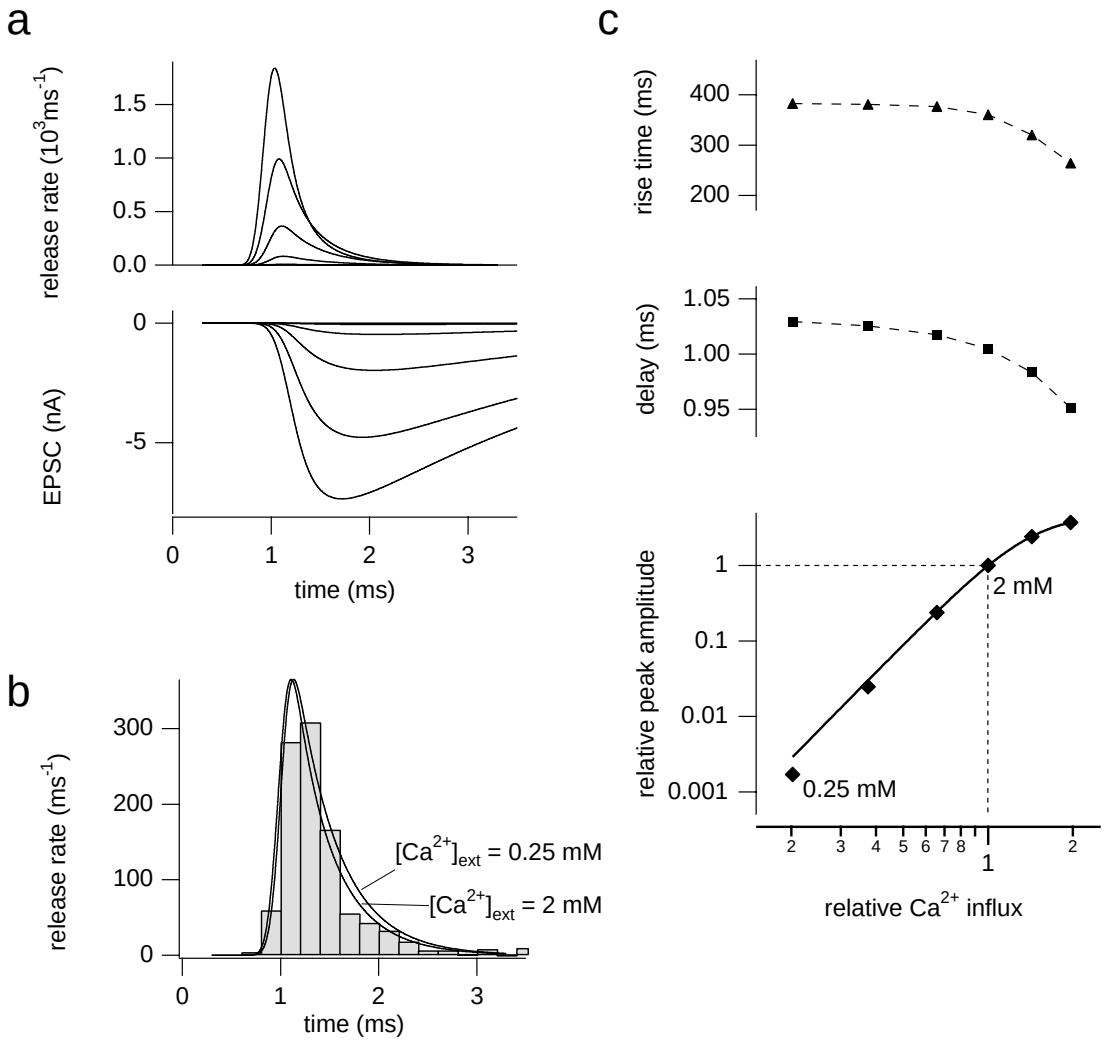

Fig 4.10: Predictions of the Ca^{2+} sensor model for varying external $[Ca^{2+}]$. (**a**) Modeled release rates, specified for the whole terminal, with different external $[Ca^{2+}]$. External $[Ca^{2+}]$ was (in mM): 10, 4, 2, 1, 0.5 and 0.25. Saturation of Ca^{2+} influx at high external $[Ca^{2+}]$ was modeled with a Michaelis-Menten relation (Schneggenburger et al., 1999, their Eq. 2). The release rates at 0.5 and 0.25 mM $[Ca^{2+}]_{ext}$ are not resolved at this scaling. (**b**) Modeled release rates at $[Ca^{2+}]_{ext}$ = 0.25 mM and 2 mM. The release rate at $[Ca^{2+}]_{ext}$ = 0.25 mM was scaled 622-fold. It exhibits a time course almost identical to that at $[Ca^{2+}]_{ext}$ = 2 mM. Also shown is a typical delay histogram constructed from miniature EPSCs evoked by afferent stimulation in $[Ca^{2+}]_{ext}$ = 0.25 mM (Borst and Sakmann, 1996). (**c**) Dependence of modeled EPSC 20-80% rise times (*triangles*), delays (*squares*) and amplitudes (*diamonds*) on relative Ca^{2+} influx, on lin-log and log-log scales, respectively. The Ca^{2+} influx at $[Ca^{2+}]_{ext}$ = 2 mM corresponds to 1. For Ca^{2+} influx below that, modeled rise times and delays are relatively constant. *Bottom*: The EPSC amplitude-Ca^{2+} influx relation was fit (*solid line*) with a Hill-equation of the form $A = A_{max}\ J_{Ca}^{n}/(J_{Ca}^{n}+K^{n})$, where A is the EPSC amplitude normalized to the value at 2 mM, A_{max} the maximal potentiation factor, J_{Ca} the Ca^{2+} influx at a given $[Ca^{2+}]_{ext}$ and n the Hill-coefficient (*compare to* Schneggenburger et al., 1999, their Fig. 3).

4.3.4 Dependence of glutamate release rates on resting [Ca^{2+}] level

When the presynaptic terminal was dialyzed with a caged Ca^{2+} solution that also contained Fura-2-FF, it was possible to estimate the presynaptic [Ca^{2+}] present before the UV laser pulse was applied. Since Fura-2-FF has a K_D for Ca^{2+} of 8.9 µM, the fraction of indicator bound to Ca^{2+} varies only little at submicromolar Ca^{2+} levels, and is therefore difficult to measure accurately. Nevertheless, the average [Ca^{2+}] in the terminal before the UV flash ([Ca^{2+}]$_{pre\text{-}flash}$), measured 15 to 5 ms before the UV pulse, was somewhat larger than zero, as indicated by a fluorescence ratio $R_{pre\text{-}flash}$ that was larger than the minimal ratio R_{min} (Fig. 4.11 a). It was not predictable from the composition of the presynaptic solution, how much the measured $R_{pre\text{-}flash}$ would deviate from R_{min}, and its variability probably originated in part from errors in the subtracted fluorescence background. Therefore, the data points obtained with Fura-2-FF were grouped according to their [Ca^{2+}]$_{pre\text{-}flash}$ into two classes, in order to detect a possible dependence of the release on [Ca^{2+}]$_{pre\text{-}flash}$ levels. First, the laser-evoked EPSC amplitudes, normalized to the cumulative EPSC amplitude, were analyzed (Fig. 4.11 b). In the 'high [Ca^{2+}]$_{pre\text{-}flash}$ group' the normalized amplitude was reduced by approximately 50%. This may indicate that the size of the releasable vesicle pool was diminished, or that a decrease in release probability led to more asynchronous release and therefore less amplitude summation of the released quanta. Next, the peak release rates per vesicle were measured as described earlier and plotted versus the amplitude of the [Ca^{2+}] jump (Fig. 4.11 c). This time, the combined set of the 'low [Ca^{2+}]$_{pre\text{-}flash}$' and the 'high [Ca^{2+}]$_{pre\text{-}flash}$' group was fit with a Hill-equation (*see legend of* Fig. 4.10 c). Thus, it was observed that the peak release rates measured in the presence of high [Ca^{2+}]$_{pre\text{-}flash}$ are also reduced compared to the 'low [Ca^{2+}]$_{pre\text{-}flash}$' experiments. The residuals of the data of both groups from the common regression curve were plotted versus the estimated [Ca^{2+}]$_{pre\text{-}flash}$ (Fig. 4.11 d). A regression analysis of the combined data revealed a negative correlation between the residuals and the basal [Ca^{2+}] level, indicating that terminals with increased [Ca^{2+}]$_{pre\text{-}flash}$ tend to release glutamate at reduced rates.

This finding may be explained by a steady-state reduction of the vesicle pool size if the spontaneous release rate before the UV pulse, which has not yet been analyzed, is increased during elevated basal [Ca^{2+}] levels. Alternatively, a regulatory mechanism such as adaptation of release-ready vesicles or accumulation of re-supplied vesicles in a reluctant state may reduce the average release probability at this synapse during increased basal [Ca^{2+}] levels (Hsu et al., 1996; Wu and Borst, 1999). While it is

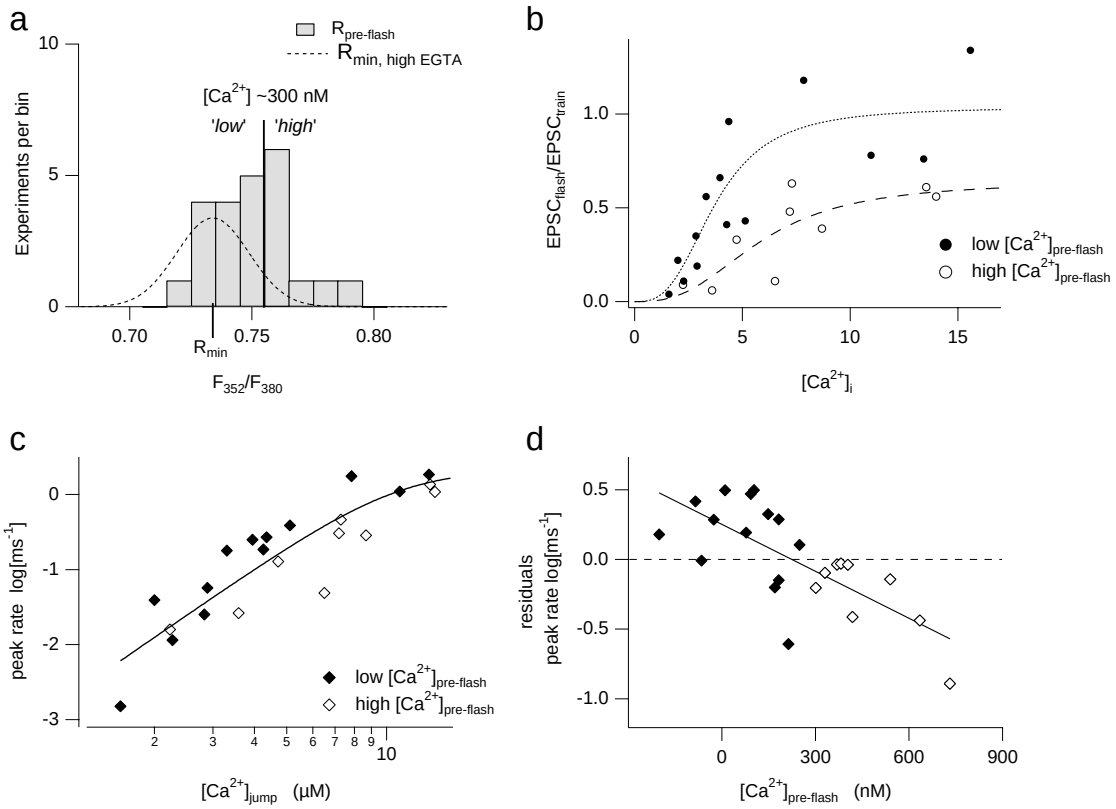

Fig. 4.11: Effect of $[Ca^{2+}]_{pre\text{-}flash}$ on peak release rates. (**a**) A histogram of pre-flash fluorescence ratios (F_{352}/F_{380}) of Fura-2-FF. The data are both from the experiments displayed in Fig. 4.8 for $[Ca^{2+}]$ jumps between 1.5 and 18 µM and from experiments discarded because of increased $[Ca^{2+}]_{pre\text{-}flash}$. The average pre-flash (F_{352}/F_{380}) deviates from the minimal ratio (R_{min}) measured with solution C. Experiments with a pre-flash (F_{352}/F_{380}) <0.755 and >0.755 (corresponding to a $[Ca^{2+}]_{pre\text{-}flash}$ <300 nM and >300 nM) were classified as 'low' and 'high' $[Ca^{2+}]_{pre\text{-}flash}$ experiments, respectively. The latter group was not included in Fig. 4.8. (**b**) The amplitude of flash-evoked EPSCs, normalized as described in the legend of Fig. 4.6, is plotted versus the $[Ca^{2+}]$ jump amplitude. The 'low' and the 'high' $[Ca^{2+}]_{pre\text{-}flash}$ groups were fit separately (*dotted and dashed curves*). The normalized EPSC amplitudes of the 'high' $[Ca^{2+}]_{pre\text{-}flash}$ group were about 50% smaller than those of the 'low' $[Ca^{2+}]_{pre\text{-}flash}$ group. (**c**) The peak release rates per vesicle of the two groups are plotted versus the $[Ca^{2+}]$ reached after the flash on log-log coordinates and fit as one data set with a Hill-type relation (K = 11 µM, n = 3.1). The peak release rates obtained in the 'high' $[Ca^{2+}]_{pre\text{-}flash}$ experiments are smaller than the release rates obtained at low $[Ca^{2+}]_{pre\text{-}flash}$. (**d**) The residuals of the fit in (c) are plotted versus the pre-flash $[Ca^{2+}]$ levels measured in the same experiments. The data are negatively correlated ($\rho_{Pearson}$ = -0.72), as indicated by the *solid line*, suggesting that peak release rates are reduced at increased basal $[Ca^{2+}]$ levels.

currently difficult to distinguish between these possibilities, an analysis of the dependence of the cumulative amount of spontaneous release on submicromolar $[Ca^{2+}]$ levels prior to the first UV pulse may be helpful to say more about the underlying mechanisms.

5. Discussion

5.1 Summary

During synaptic transmission, the presynaptic action potential couples to the biochemical release process by the opening of Ca^{2+} channels and Ca^{2+}-dependent activation of a release sensor that triggers the release of transmitter. Here, the dependence of transmitter release on intracellular [Ca^{2+}] was determined in a glutamatergic calyx-type synapse in slices of the rat brainstem. Because of the fast speed of glutamatergic synapses, an electrophysiological setup was equipped with a rapid fluorescence detection system and a short-pulsed UV laser in order to both evoke and measure uniform [Ca^{2+}] elevations on a time scale comparable to that of the release process. The frequency responses of the electrophysiological and optical recording system were analyzed with appropriate test signals. The kinetics of UV laser-induced Ca^{2+} uncaging were analyzed in microcuvettes and quantified with a numerical kinetic model.

Photolysis of caged Ca^{2+} and pre- and postsynaptic whole-cell recordings were performed to determine the Ca^{2+} sensitivity of release in the absence of sharp spatial concentration gradients, which are expected to occur during action potential-evoked release (Ca^{2+} *microdomains*). Prior to UV-induced [Ca^{2+}] jumps, the size of the readily releasable vesicle pool and the release rate evoked by presynaptic action potentials were measured using afferent stimulation of the intact terminal, indicating a pool size of ca. 800 vesicles. Following this, the terminal was dialyzed and the releasable vesicle pool was challenged with [Ca^{2+}] jumps. A homogeneous rise in the presynaptic [Ca^{2+}] to 1 µM resulted in a clearly measurable increase in release. The peak release rates depended on presynaptic [Ca^{2+}] with more than the fourth power. A [Ca^{2+}] jump to 30 µM or more depleted the releasable vesicle pool in less than 0.5 ms. A kinetic model was devised to quantify the release rate-[Ca^{2+}] relation measured in this synapse type. The model was used to estimate the [Ca^{2+}] transient during action potential-evoked release, suggesting that a brief elevation of [Ca^{2+}] to less than 10 µM would be sufficient to reproduce the physiological release pattern. Furthermore, the model predictions were consistent with earlier experimental results at this synapse with respect to the dependence of EPSC size and time course on external [Ca^{2+}]. Finally, increases in the presynaptic [Ca^{2+}] measured before the [Ca^{2+}] jump were observed to reduce the release rates.

5.2 Methodological aspects

5.2.1 Optically controlled [Ca^{2+}] elevations in small volumes

5.2.1.1 *Homogeneity of the evoked* [Ca^{2+}] *jump*

The analysis of the Ca^{2+} sensitivity of release rests on the assumption that the UV pulses evoked uniform [Ca^{2+}] elevations throughout the presynaptic terminal. To assess whether this assumption holds in the lateral directions, the distribution of uncaged fluorescein was recorded briefly after a laser pulse. It was verified that the pulse energy was distributed homogeneously over the region of interest, which circumscribed the presynaptic terminal (Fig. 3.4). In the axial direction, one might expect that the pulse intensity would rapidly decrease because of absorption by the Ca^{2+} cage and indicator. Therefore, the extent to which the accumulation of absorbing molecules in the presynaptic terminal leads to a reduction in the pulse intensity was estimated. The molar extinction coefficient of DM-nitrophen is 4,300 $M^{-1} cm^{-1}$ (Kaplan and Ellis-Davies, 1988) and 22,000 $M^{-1} cm^{-1}$ for Mag-Fura-2 or 33,000 $M^{-1} cm^{-1}$ for Fura-2-FF (Molecular Probes, TefLabs, specification). The calyx-shaped terminal has a thickness of ~1-2 µm and a diameter of ~17 µm (unpublished observation). Therefore, the cumulative thickness of presynaptic structures filled with DM-nitrophen (9 mM) and Ca^{2+} indicator (1 mM) parallel to the optical axis is well below 10 µm. Using these numbers as a conservative estimate, Lambert-Beer's law (Eq. 2.29) predicts that after passage through the test volume the pulse energy will be attenuated by, at most, 15% compared to the incident energy. This indicates that the assumption of homogeneous [Ca^{2+}] elevations throughout the presynaptic terminal is reasonable.

5.2.1.2 *Estimate of error for ratiometric* [Ca^{2+}] *measurements*

The quality of the present estimate for the Ca^{2+} sensitivity of glutamate release critically depends on the ratiometric measurement of [Ca^{2+}]. Therefore, some of the possible sources of error will be considered.

The measurement of fluorescence ratios with ratiometric dyes is a common tool to measure intracellular [Ca^{2+}] levels. Errors may be introduced if the recorded background fluorescence does not correspond to the true background fluorescence that adds to the indicator signal. Because the use of a small photodiode did not allow for simultaneous background measurement in an adjacent region during the sweep, background fluorescence was measured from several neighboring regions after the

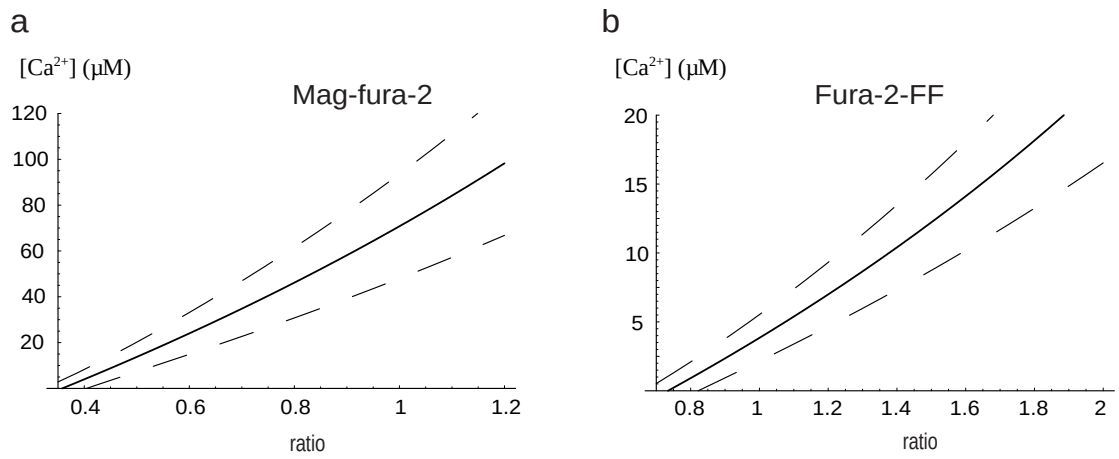

Fig. 5.1: Error estimate of the ratiometric $[Ca^{2+}]$ measurement. (**a**) The conversion from fluorescence ratios measured with Mag-Fura-2 to $[Ca^{2+}]$ is shown in the relevant range of the experiments (*solid line*). The $\pm 1\sigma$ levels are also indicated (*dashed lines*). (**b**) Same as in (a), but for Fura-2-FF.

experiment and averaged. Since most background signal is expected to arise from spilled indicator during the approach of the open patch pipette, the deviation would be most severe if fluorescent measurements were performed immediately after the cell-attached configuration had been established. Photolysis sweeps were usually recorded ~10 minutes or more after the presynaptic pipette had been attached to the terminal. Therefore, spilled indicator has probably been washed out, unless it was immobilized in some other way. Still, variations in slice autofluorescence are likely to contribute to the variability in fluorescence measurements of the $[Ca^{2+}]$.

The conversion of fluorescence ratios to $[Ca^{2+}]$ requires the knowledge of the dissociation constant of the Ca^{2+} indicator. It should be noted that a systematic error in the K_D measurement propagates directly into the measured $[Ca^{2+}]$ levels. It is known that the indicator affinity for Ca^{2+} may vary depending on, for example, the ionic environment, pH and temperature. Therefore, the K_D and R_{min} and R_{max} were measured directly in presynaptic terminals, under similar ionic conditions and with a highly buffered $[Ca^{2+}]$. The measurement of the K_D relies on the assumption that the $[Ca^{2+}]$ does not change when the solution is introduced into the terminal. The equilibrium of the Ca^{2+} buffering, however, may be perturbed by the Ca^{2+} transport mechanisms in the terminal membrane. Therefore, external $[Ca^{2+}]$ was reduced and the internal $[Na^+]$ was increased to minimize the $[Na^+]$ and $[Ca^{2+}]$ gradients that drive the Na^+/Ca^{2+}-exchanger (Table 3.1, Solution E).

The measured mean values of the dissociation constants fell into a range that has been measured previously in other preparations ($K_{D,\ Mag\text{-}Fura\text{-}2}$: 20 – 100 µM, Thomas et al., 1993; Baylor and Hollingworth, 1998; Golovina and Blaustein, 1997; Naraghi, 1997);

($K_{D,\ Fura\text{-}2\text{-}FF}$: 5 – 30 µM, London et al., 1994; Golovina and Blaustein, 1997; Xu-Friedman and Regehr, 1999; Schneggenburger and Neher, 2000).

The random error in the [Ca^{2+}] measurement was estimated using standard error propagation. Since the background fluorescence was typically 5-10% of the indicator signal recorded from the synapse, it was estimated that the error in the fluorescence ratio was 10%. Using the errors in the measured calibration constants K_D, R_{min} and R_{max}, the 1σ-levels for the conversion of fluorescence ratios into [Ca^{2+}] levels were calculated (Fig. 5.1). The 1σ-error in the estimated [Ca^{2+}] was <50%, when [Ca^{2+}] measured with Mag-Fura-2 exceeded 12 µM, and when [Ca^{2+}] measured with Fura-2-FF exceeded 3 µM. It should be noted that data measured with these two dyes fell into the same region in the peak release rate-[Ca^{2+}] plot (Fig. 4.8) in the range between 5 and 15 µM.

5.2.1.3 *Comparison of predicted release rates with* **[Ca^{2+}]** *steps and* **[Ca^{2+}]** *spikes*

It is known that Ca^{2+} uncaging with short laser pulses does not produce step-like jumps in the [Ca^{2+}], but leads to a rapid rise in [Ca^{2+}], dominated by the decay rate of the DM-nitrophen intermediates and the Ca^{2+} dissociation rates of the photoproducts (Ellis-Davies et al., 1996; Escobar et al., 1997). The decay of this Ca^{2+} spike is governed by the Ca^{2+} association rates of the buffers present, which comprise the Ca^{2+} indicator, unphotolyzed DM-nitrophen and, if applicable, ATP, in the solutions used in this study. Since the kinetic model of the Ca^{2+} sensor for glutamate release was first adjusted with rectangular [Ca^{2+}] steps, it was important to test whether the derived Ca^{2+} sensor model also predicts the measured release rates, when it is driven with more realistic Ca^{2+} spike waveforms. Therefore, the [Ca^{2+}] time course for a given measured [Ca^{2+}] level was calculated with the Ca^{2+} buffers known to be present in the solution, and release rates and delays were calculated with the Ca^{2+} sensor model (Fig. 5.2), with the same kinetic constants used earlier to calculate rates and delays with [Ca^{2+}] steps (Fig. 4.8). Because the duration of the modeled [Ca^{2+}] spike with Fura-2-FF was systematically shorter than that modeled with Mag-Fura-2 (Fig. 5.2 a,b), the experimental data were re-grouped with respect to the indicator used in the experiment. When the Ca^{2+} sensor model was driven with Ca^{2+} spike waveforms, it predicted peak release rates very similar to the measured ones for both indicator conditions (Fig. 5.2 (a,b), *and* (c,d) *upper panels*). The model predicts slightly higher release rates in the case of Mag-Fura-2 than in the case of Fura-2-FF in the range from 2 to 15 µM. This may be because Fura-2-FF has a ~3-fold lower K_D for Ca^{2+} than Mag-Fura-2, and thus, the fraction (α) of DM-nitrophen photolyzed must be ~3-fold larger in the

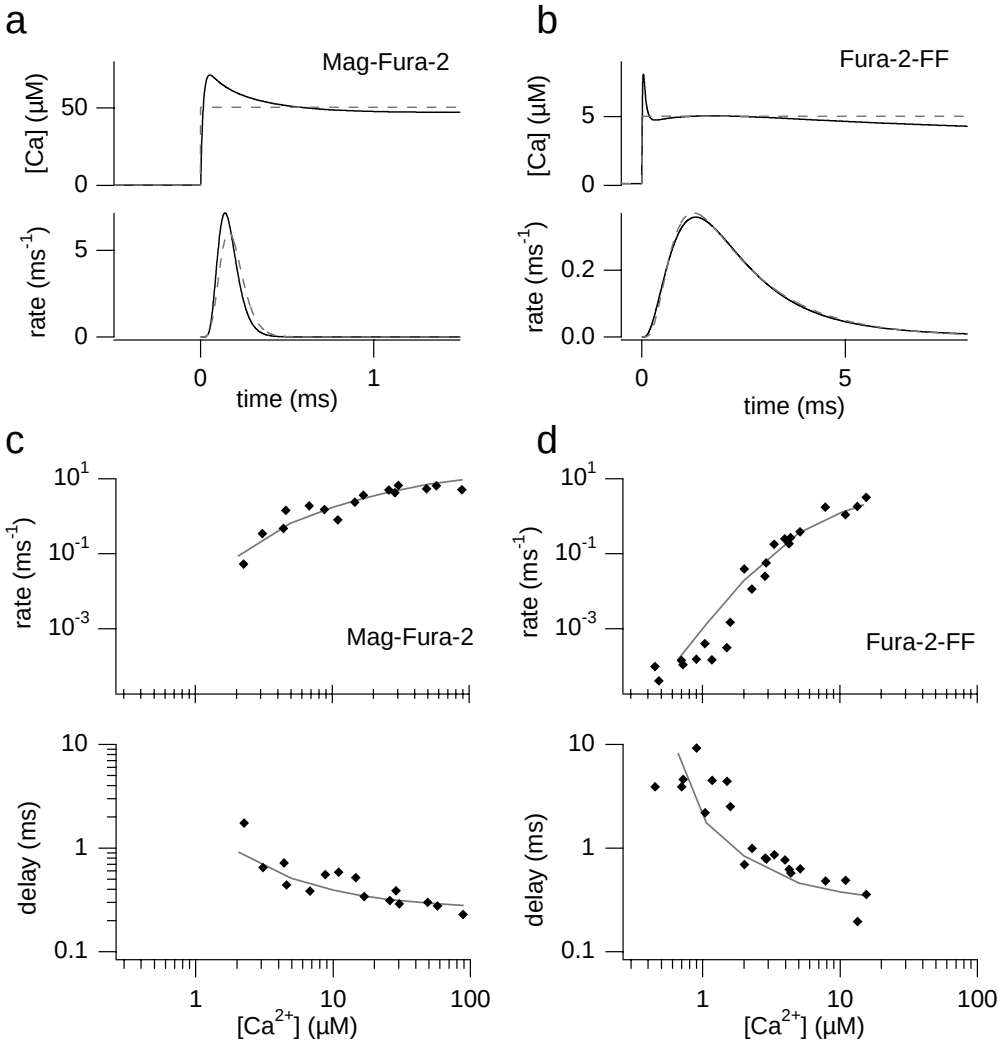

Fig. 5.2: Effect of the Ca^{2+} uncaging time course on modeled release rates. (**a**) Comparison of modeled release rates, specified per vesicle, calculated with a rectangular $[Ca^{2+}]$ jump (*dashed lines*), and with the Ca^{2+} spike time course predicted by the photolysis reaction scheme (*solid lines*). Average $[Ca^{2+}]$ between 0.4 and 0.8 ms is 50 µM, measured and modeled with Mag-Fura-2 and solution A1. (**b**) Same as in (a), but with an average $[Ca^{2+}]$ of 5.02 µM in the interval [0.8, 2.7] ms. Measured and modeled with Fura-2-FF and solution B. (**c**) and (**d**) Experimentally measured peak release rates and delays (*diamonds*), grouped with respect to the used dye. Same experimental data as in Fig. 4.8. Solid lines indicate the peak release rates and delays predicted by the kinetic Ca^{2+} sensor model, when the more realistic Ca^{2+} spike waveforms were used to simulate the release time course. Experimental $[Ca^{2+}]$ values were obtained by averaging the $[Ca^{2+}]$ measured during the rising phase of the EPSC (e.g. [0.5,1.0] ms for a $[Ca^{2+}]$ jump to 25 µM). $[Ca^{2+}]$ values used to plot simulated peak release rates and delays were obtained by averaging the simulated $[Ca^{2+}]$ in the same intervals as the experimentally measured $[Ca^{2+}]$ records for a given $[Ca^{2+}]$ level.

presence of Fura-2-FF than with Mag-Fura-2 to obtain similar measured $[Ca^{2+}]$ levels. This, in turn, means that after a small $[Ca^{2+}]$ jump in the case of Mag-Fura-2, a larger

fraction of unphotolyzed DM-nitrophen is present to buffer the briefly increased [Ca^{2+}] than with Fura-2-FF, resulting in a more strongly decaying predicted [Ca^{2+}] and a lower measured [Ca^{2+}] in the presence of Mag-Fura-2. Interestingly, this difference in peak release rates in the presence of different indicators is also observed in the experimental data (Fig. 5.2 c,d).

The modeled delays between the laser pulse and the onset of release were more sensitive to the presence of Ca^{2+} spikes (Fig. 5.2 c,d, *lower panels*), but a considerable discrepancy between modeled and measured values was not observed. It should be stressed again that the Ca^{2+} dependence of modeled and measured delays agreed well only in relative terms; when comparing the absolute values, the experimental delays were about 250 µs larger than the modeled delays. This shift was added to all modeled delay values in the Fig. 4.8, 4.9 and 5.2. What might be the reason for this discrepancy? The Ca^{2+} sensor model features a fast Ca^{2+} association rate constant (3×10^8 M^{-1} s^{-1}), which was chosen to model the steep increase in release rates over roughly four orders of magnitude when [Ca^{2+}] varied between 0.5 and 15 µM. If the chosen association rate was smaller, the modeled delays became larger, but it became difficult to model the strong Ca^{2+} dependence of release rates with Ca^{2+} association rate constants below 1×10^8 M^{-1} s^{-1}. Other factors may contribute to the discrepancy in delays. First, it is difficult to obtain a measure to compare modeled and experimental delays. We chose an amplitude threshold of -35 pA for the experimental values, whereas the modeled delays were calculated as the time when the release rate integral equaled one vesicle. Probably, an amplitude of –35 pA during compound release at a holding potential of –30 mV requires the release of more than one vesicle, so that the experimental delays would be biased towards larger values. Second, the model does not include biochemical steps that should occur between the activation of the release promoter molecule and the opening of postsynaptic AMPA receptors. These steps, which comprise conformational changes of the release machinery, the fusion of vesicles with the presynaptic membrane, the discharge and diffusion of glutamate from the presynaptic membrane across the synaptic cleft, and the activation reaction of the AMPA receptors, may further contribute to the delay observed in our experiments. For example, the time constant for transmitter discharge through the putative fusion pore of a synaptic vesicle was estimated to be 100 µs (Almers and Tse, 1990), illustrating that the order of magnitude of the observed discrepancy is not unexpected. The biochemical steps following Ca^{2+} binding to the release sensor are, however, difficult to estimate quantitatively, because many parameters, for example regarding the time scale of the fusion reaction, are not known.

The previous analysis of the impact of Ca^{2+} spikes on the release rate model depends on the kinetic parameters chosen to model the Ca^{2+} spikes. The Ca^{2+} spike time course was modeled using rate constants previously published, if available (Ellis-Davies et al., 1996; Escobar et al., 1997; Ayer and Zucker, 1999). In our modeling, the Ca^{2+} spike ratio depended to a large degree on the decay rate of the DM-nitrophen intermediates and on the Ca^{2+} dissociation rate constant of the photoproduct. If these constants were much larger than given in the studies mentioned above, larger Ca^{2+} spike ratios would be encountered. While the intermediate decay rate was measured directly (Ellis-Davies et al., 1996), the photoproduct's Ca^{2+} dissociation rate was deduced as ($k_{on} \times K_D$) from Ca^{2+} association rate measurements. Probably the best measurement of the Ca^{2+} uncaging rate is given by Ellis-Davies et al. (1996, Fig. 4) in which the Ca^{2+}-sensitive indicator fluorescence reaches a half-maximal value after ~20-25 µs. Although our model of Ca^{2+} uncaging kinetics features two decay pathways of DM-nitrophen and uses a photoproduct Ca^{2+} dissociation rate constant of 90×10^3 M^{-1} s^{-1}, similar to that published in Escobar et al. (1997) and Xu et al. (1997) but ~2.7-fold smaller than that of Ellis-Davies et al. (1996), it is compatible with the fast rising phase of the $[Ca^{2+}]$ described by the latter authors.

Nevertheless, the Ca^{2+} spike model is influenced by quantities difficult to measure or not known. For example, endogenous buffers, which are present in the presynaptic terminal (Helmchen et al., 1997) but not in the cuvette experiments, cannot be taken into account quantitatively, because their binding rates have not been determined in the Calyx of Held synapse. They are expected to further damp the initial Ca^{2+} spike, if the association rate constant is as fast as that estimated in chromaffin cells (1×10^8 M^{-1} s^{-1}, Xu et al., 1997). Finally, it should be noted that, in the present study, the experimentally observed glutamate release rates were similar for similar measured $[Ca^{2+}]$ under different Ca^{2+} buffer conditions (solutions A1-3 and B), in which the Ca^{2+} spike ratio is predicted to differ considerably. This suggests that the release rates are mostly controlled by the sustained measured $[Ca^{2+}]$ levels and not by the variable and brief overshoot in $[Ca^{2+}]$.

An alternative approach to evoke UV-induced $[Ca^{2+}]$ jumps would be the use of light sources with a longer pulse duration than that of the nanosecond Nd:YAG laser. For example, UV flash lamps have been used extensively to uncage Ca^{2+} in muscle (Rapp, 1998), in endocrine cells (Neher and Zucker, 1993), and in presynaptic terminals (Delaney and Zucker, 1990; Heidelberger et al., 1994). Typically, the flash lamp provides a high intensity UV flash of 1-2 ms duration. This has the advantage that a higher fraction of the Ca^{2+} cage can be photolyzed, because the pulse duration is much longer than the lifetime of the excited state of the chelator molecule (~10^{-8} s), allowing

for multiple excitation cycles (McCray et al., 1992). In addition, the rising phase of the [Ca^{2+}] is predicted to be slower than the [Ca^{2+}] rising phase with nanosecond laser pulses, because the photolysis energy is distributed over the time window of the flash duration, and therefore not determined by the intrinsic dissociation kinetics of the Ca^{2+} cage. Early experiments with a xenon flash lamp (Rapp optoelectronics, Germany, measured pulse duration: ~1.5 ms) revealed, however, that the EPSCs had often already started in the interval of the UV flash delivery. This prevented the fluorometric measurement of [Ca^{2+}] levels before and during the EPSCs, and made it difficult to estimate the [Ca^{2+}] that underlay the observed release rates, because the onset of release apparently coincided with the rising phase of the [Ca^{2+}]. The recent development of a UV flash lamp with a short pulse width (<100 µs, FlashMic, Rapp optoelectronics) may improve this situation. It will be interesting to compare release rates measured with this system with the release rates obtained with short UV laser pulses.

5.2.2 Methods for measuring exocytosis

5.2.2.1 *Postsynaptic currents, other methods*

In the present study, the activation of postsynaptic glutamate receptor channels of the AMPA type was used to quantify the release of glutamate from presynaptic vesicles. In principle, this is a useful measure for presynaptic release rates because AMPA receptor channels exhibit rapid activation kinetics in response to fast glutamate application (Jonas and Spruston, 1994). Furthermore, their location at the postsynaptic soma permits recording of glutamate-evoked AMPA currents with little low pass filtering by the postsynaptic membrane compared to dendritic synapses in other preparations. In the latter case, the electrical filtering of synaptic currents introduced by the larger electrotonic distance between the input and the recording site is much more severe. Other methods to measure rapid exocytosis have been developed (*reviewed by* Angleson and Betz, 1997). They comprise time-resolved measurements of presynaptic capacitance changes using a lock-in amplifier (Lindau and Neher, 1988; Heidelberger et al., 1994). In this method, net changes in capacitance of the terminal membrane are measured while simultaneously stimulating exocytosis. The rapid increases of terminal capacitance can be associated with the insertion of vesicle membrane into the plasma membrane and the release of glutamate (von Gersdorff et al., 1998). However, only net capacitance changes are reported by this method. It has been found that, in endocrine cells, non-specific capacitance increases, which are not accompanied by transmitter release, may contribute to the signal (Oberhauser et al., 1996). Furthermore, the capacitance increase due to vesicle fusion may be

counteracted by a concurrent decrease in capacitance due to endocytosis, making the derivation of release rates from capacitance measurements more complicated. Another method to measure transmitter release is the amperometric detection of oxidizable transmitters such as serotonine or catecholamine (Wightman et al., 1991). In this method, a carbon fiber electrode is brought into close proximity of the releasing cell. A release event is then detected as a small current in the electrode, originating from the oxidization of transmitter, which has diffused to the electrode surface. This method has the advantage that transmitter release is detected directly, with high spatial resolution because of the rapid dissipation of the transmitter cloud from more distal release sites. However, it is not applicable to glutamate, which does not give rise to an oxidization current, and is probably difficult to implement in the MNTB giant synapse because the pre- and postsynaptic compartments are tightly coupled by stabilizing contact zones (*puncta adherentia*), preventing the easy isolation of the presynaptic release face. Finally, optical tools have been used to measure presynaptic vesicle fusion, using styryl membrane dyes such as FM1-43 or FM2-10 (Betz et al., 1992; Klingauf et al., 1998). There, the releasable pool of vesicles is stained with the indicator, which accumulates in the membrane of endocytosed vesicles during a loading period. After wash-out of the extracellularly applied indicator, the fluorescence at putative release sites decreases in a stimulus-dependent fashion. This is interpreted as the fusion of stained vesicles and the subsequent wash out of the membrane dye during stimulated exocytosis. This method has been used extensively to characterize synaptic vesicle cycling (Cochilla et al., 1999) and was also employed to perform optical quantal analysis in which the release probability of vesicles at single boutons was estimated (Ryan et al., 1997; Murthy et al., 1997). For the measurement of the kinetics of release it is of limited use, because the optical signal is governed by the departition rate of the indicator from the fused membrane, which is much lower than the release rate encountered during rapid synaptic exocytosis.

In summary, the MNTB giant synapse offers a favorable situation in which the fusion of synaptic vesicles and subsequent glutamate release can be measured with high temporal resolution by measuring postsynaptic, AMPA receptor-mediated EPSCs.

5.2.2.2 *Saturation of postsynaptic receptors*

Vesicle release rates were calculated from compound EPSCs using the average time course of the miniature EPSC generated by the release of a single transmitter packet. This analysis is based on the assumption that during compound release, the miniature EPSC waveform is not altered by the synchronous release of many transmitter quanta. To prevent a change of the mEPSC waveform because of desensitization, cyclothiazide was added to the external solution, which slowed the decay of EPSCs

(*compare* Fig. 4.4). Nevertheless, the assumption of constant mEPSC waveforms may be inadequate if the glutamate concentration during multivesicular release accumulates in the synaptic cleft, such that the postsynaptic receptors become saturated with transmitter. If a transmitter packet is released onto an ensemble of receptors partially saturated by previously released glutamate, the resultant mEPSC will probably have a similar rise time but a reduced amplitude. Evidence from other synapses suggests that multivesicular release may lead to accumulation of transmitter in the synaptic cleft, conditioning a high channel open probability and saturating the postsynaptic release detector (Tong and Jahr, 1994; Otis et al., 1996b; Silver et al., 1996). To get an estimate for the degree of saturation under our experimental conditions, experiments were performed in which a rapidly dissociating competitive antagonist (kynurenic acid, KYN) was used to partially inhibit the binding of transmitter to the receptors (Clements et al., 1992; Diamond and Jahr, 1997). In the presence of KYN (1 mM), cumulative EPSC amplitudes were reduced to 58 ± 4 % (n = 3). The similarity of the time course of EPSC trains in the presence and absence of KYN suggests that the considerable decrease in EPSC amplitude during the first ~10 action potentials is most likely mediated by the exhaustion of a presynaptic vesicle pool, and less by postsynaptic receptor saturation (Fig. 5.3 a). When EPSCs were elicited by large $[Ca^{2+}]$ jumps to ~40 µM in the presence of KYN, they exhibited a similar rise time and a faster decay than those measured under control conditions in earlier experiments (Fig. 5.3 b,c). Their peak amplitude was (1.32 ± 0.19)-fold (n = 3) larger than the cumulative EPSC amplitude in the presence of KYN in the same experiment, whereas in the control experiments, the peak amplitude of EPSCs evoked by $[Ca^{2+}]$ jumps >15 µM was (1.03 ± 0.06)-fold (n = 8) larger than the respective cumulative EPSC amplitude, both measured in the absence of KYN (Fig. 5.3 d). This indicates that postsynaptic receptors are unlikely to be saturated dramatically during large EPSCs, because in that case the laser-evoked EPSC in the presence of KYN should exceed the cumulative EPSC amplitude to a larger degree than observed here, since more receptors would become available by the rapid dissociation of KYN (k_{off} = 6000 s^{-1}, Diamond and Jahr, 1997).

On the other hand, recent studies suggested that at the MNTB giant synapse, the estimated size of the mEPSC amplitude may be reduced by 50% or more in the presence of cyclothiazide during glutamate release evoked by voltage steps. This led to much larger estimates of 2000 – 5000 for the number of vesicles in the releasable pool (Neher and Sakaba, 2001; Sakaba and Neher, 2001b; Sun and Wu, 2001). It was

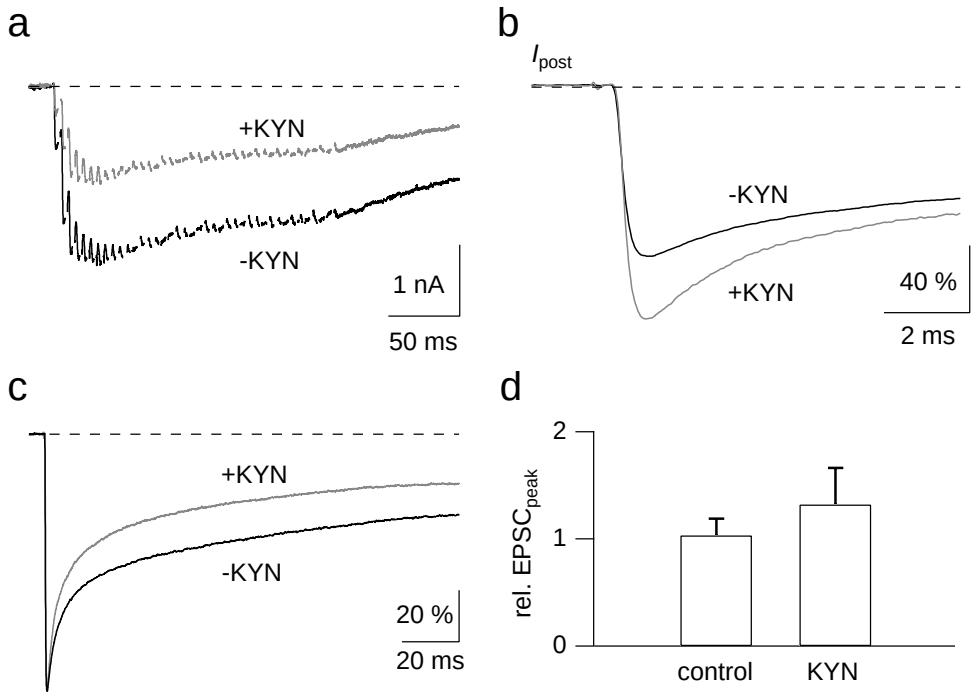

Fig. 5.3: Absence of profound saturation of postsynaptic glutamate receptors. (**a**) Trains of EPSCs evoked by afferent stimulation (200 Hz) in the absence and presence of the rapidly dissociating antagonist kynurenic acid (KYN, 1mM). The time course of the EPSC train is similar under both conditions, while the amplitudes are reduced to ~50 % in the presence of KYN. (**b**) EPSCs evoked by $[Ca^{2+}]$ jumps to 40-50 µM, from two different experiments. The EPSCs were scaled to the cumulative EPSC amplitude measured under the same pharmacological conditions as the laser-evoked EPSCs, i.e. in the presence and absence of KYN, respectively. The rise time is very similar, but the peak is slightly larger in the presence of KYN. (**c**) Average of EPSCs evoked by $[Ca^{2+}]$ jumps >40 µM in the absence (n = 3) and presence of KYN (n = 2). EPSCs were scaled to the peak current. KYN accelerates the decay of the EPSC. (**d**) Comparison of the ratio between laser-evoked EPSC peak amplitudes and the cumulative EPSC amplitude, both measured in the absence (control, n = 8) and presence of KYN (n = 3), respectively, for $[Ca^{2+}]$ jumps >15 µM. The increase in the presence of KYN is not significant (two-tailed t-test, P>0.05). All experiments were done in the presence of CTZ (100 µM) to inhibit receptor desensitization.

furthermore reported that this pool may comprise vesicles with heterogeneous release probabilities when challenged with voltage steps (Sakaba and Neher, 2001b). Thus, the phasic release observed during action potential trains may preferentially draw from the more sensitive component of this pool, which may partially explain the difference between our pool size estimate and those of the later studies.

How would a reduction in quantal size during compound release to, for example, 50% of the isolated mEPSC amplitude affect our estimate for the Ca^{2+} sensitivity of the release sensor and for the $[Ca^{2+}]$ transient? In a simplified picture, in which all quanta experienced the same reduction of mEPSC amplitude during compound EPSCs, the number of vesicles in the releasable pool would be underestimated by a factor of two

by the method described in section 4.2.3. Also, the peak release rates during EPSCs would be underestimated by the same factor, because they are inversely proportional to the mEPSC amplitude used for the deconvolution method. Therefore, the error would cancel out by dividing the calculated peak release rate by the estimated number of vesicles in the releasable pool, which was done to obtain the release rate per vesicle specified in (Fig. 4.8). Also, the Ca^{2+} sensor model would remain unaffected because the predicted peak release rates are directly proportional to the initial number of releasable vesicles by virtue of Eq. 2.34. If the same amount of saturation is assumed for the release evoked during an action potential, the peak release rates would be underestimated correspondingly, but the simultaneous underestimate in the number of releasable vesicles would compensate for that error such that one would expect a similar [Ca^{2+}] transient of around 10 µM to be required for the release rates obtained with a reduced mEPSC amplitude.

Although this picture shows that, if postsynaptic receptors were moderately saturated, some of the introduced errors still counteract each other favorably for the present analysis, it is probably oversimplified, since different degrees of saturation would likely occur at the start and the end of the release period. Therefore, it is necessary to further investigate the contribution of saturation and to consider the role of heterogeneous sub-pools in shaping the EPSC time course, in particular during later phases of the EPSC. Alternatively, it would be desirable to obtain an independent measure of release rates that is not affected by postsynaptic receptor properties. A promising route is the optical detection of synaptic vesicle release, which has been demonstrated recently in retinal bipolar cells, using evanescent wave microscopy (Zenisek et al., 2000). However, as discussed above, optical methods are still too slow because of the limiting biochemical properties of the fluorescent vesicle dyes. On the other hand, genetic vesicle markers such as green fluorescent protein-(GFP)-synaptobrevin constructs may be used to follow the functional state of a vesicle optically with improved temporal resolution (Miesenböck et al., 1998; Sankaranarayanan and Ryan, 2001). For example, GFPs can be used as a pH sensor that reports the acidification state of a vesicle. If the vesicle releases its contents into the extracellular space, its lumen will be simultaneously neutralized, which can be used to detect release events. It is expected that the underlying optical signal is dominated by the deprotonation reaction of the fluorophore, which should be considerably faster than the departitioning time constant of styryl dyes from lipid bilayers. Thus, optical tools should complement electrophysiological approaches to elucidate rapid release processes at this and other synapses.

5.3 Physiology

5.3.1 The model of glutamate release

5.3.1.1 *General remarks*

The experimental study of the Ca^{2+} sensitivity of glutamate release at the MNTB giant synapse was complemented by a kinetic model of the Ca^{2+} sensor that triggers the fusion of the presynaptic vesicle. This model was useful in describing the experimental data in quantitative terms, and in particular in obtaining an estimate of the typical [Ca^{2+}] that is reached at most of the release sites during a presynaptic action potential. The model yielded an estimate of the Ca^{2+} affinity of the individual binding site of ~10 µM. Regarding the Ca^{2+} binding reaction, the model is similar to previous release models, which required the sequential binding of three to four Ca^{2+} ions before vesicle fusion is triggered (Heidelberger et al., 1994; Heinemann et al., 1994). However, because the experimentally obtained release rates increased with a power dependence on [Ca^{2+}] larger than four, the fit to the data was clearly improved when the model comprised another, fifth sequential Ca^{2+} binding step. The present model also differed from previous models, because it featured Ca^{2+}-independent activation and inactivation steps, which may be interpreted as transition time constants for the sensor to change its conformation, thus catalyzing the fusion of a vesicle. Different time courses of Ca^{2+} binding and of a subsequent conformational change have been reported previously, for example for troponin C (Hazard et al., 1998). The actual depletion of the releasable vesicle pool was then modeled in a second scheme, in which the maximal release rate constant (ρ_{max}) was scaled with the occupancy of the Ca^{2+} sensor residing in the activated, release-promoting state. This modification was mainly introduced because many experimental data suggest that the time course of the release probability is quite insensitive to the external [Ca^{2+}], and therefore to the intracellular [Ca^{2+}] reached during action potential-evoked release (Datyner and Gage, 1980; Parnas et al., 1986; Yamada and Zucker, 1992; Borst and Sakmann, 1996). This suggests that the release time course is controlled not by the Ca^{2+} binding kinetics of the Ca^{2+} sensor, but rather by Ca^{2+}-independent processes. This experimental observation could be emulated by introducing Ca^{2+}-independent reaction steps, as was previously suggested by Yamada and Zucker (1992), and also employed in the present study (Fig. 4.10). It should be noted, however, that the predicted release rates were not very sensitive to the absolute values of the activation and inactivation constants (γ, δ). The time course of release was instead defined by

the ratio of these rate constants, and was similar if both constants were scaled up by a factor of 10-20.

It is noteworthy that the model offers room for the interesting interpretation that multiple Ca^{2+} sensors may promote the fusion of a single vesicle, because the final release rate is proportional to the occupancy of the activated state of the Ca^{2+} sensor. Thus, the individual release probability of the vesicle increases with the number of release sensors on its surface which reside in the activated state. The occupancy of the activated state, however, was small, even during larger [Ca^{2+}] jumps (steady-state occupancy 0.33 for a [Ca^{2+}] of 20 µM). This indicates that only a small fraction of sensors become activated. If the number of Ca^{2+} sensors per vesicle is in the order of a few tens of units, this would mean that less than ten sensors activate, which may indicate that a continuous solution of the system of differential equations is no longer applicable. In that case, it would be interesting to extend the simulation to a discrete, Monte Carlo-type model, in which the influence of a small set of Ca^{2+} sensors on the release probability of a single vesicle is explored. For the present study, the model was mostly used as a tool to quantitatively describe the release rate-[Ca^{2+}] relation and to estimate [Ca^{2+}] levels reached during action potential-evoked release. However, it is probably too simplistic to allow for a detailed interpretation of the molecular steps that underlie the measurable data.

In the following section, the model of the Ca^{2+} sensor will be analyzed as to what extent it can reproduce other characteristics of fast central synapses, related to short term plasticity.

5.3.1.2 *Asynchronous release and facilitation*

Action potential-evoked transmitter release often exhibits two phases, synchronous (phasic) and asynchronous (delayed) release (Barrett and Stevens, 1972; Goda and Stevens, 1994). While the synchronous release period typically lasts a few milliseconds, in which release rates are increased above resting levels by several orders of magnitude, the asynchronous release period is characterized by an elevated frequency of mEPSCs and decays on a time scale of some tens to hundreds milliseconds. Previous estimates of the Ca^{2+} sensitivity of the sensor for phasic release suggested that intracellular [Ca^{2+}] levels of more than 100 µM are required to trigger release with the rates observed during action potentials (Augustine et al., 1991; Südhof and Rizo, 1996; Neher, 1998). On the other hand, fluorometric measurements demonstrated that the volume-averaged presynaptic [Ca^{2+}] following an action potential peaks at less than 1 µM, and decays on a time scale of 100 ms (Regehr and

Atluri, 1995; Helmchen et al., 1997; Koester and Sakmann, 2000; *but see* DiGregorio et al., 1999). Because of the absence of high [Ca^{2+}] during the asynchronous release period, it was suggested that two distinct release sensors, having low and high Ca^{2+} affinity respectively, are responsible for either period of release (Geppert et al., 1994; Goda and Stevens, 1994). The present results, however, indicate that at least at some synapses the phasic release sensor may be sufficiently sensitive to bind Ca^{2+} also during the slowly decaying [Ca^{2+}] after the collapse of the local [Ca^{2+}] transient, and to trigger release at much reduced rates. The dependence of asynchronous release rates on intracellular [Ca^{2+}] levels has not yet been determined in mammalian synapses, making it difficult to quantitatively compare our model with experimental values. However, at single boutons of the crayfish neuromuscular junction, Ravin et al. (1997) measured asynchronous release rates simultaneously with presynaptic [Ca^{2+}], and observed a cooperativity of four, somewhat lower than the prediction of our model of around five for submicromolar [Ca^{2+}] levels. Nevertheless, the release rates predicted by our Ca^{2+} sensor model agreed within a factor of four with the experimental values. The release rates measured by Ravin et al. (1997) and those predicted by our model are (at steady-state, [Ca^{2+}] given in parentheses): 1.2 s^{-1} and 0.3 s^{-1} (0.67 µM), 4.2 s^{-1} and 2.4 s^{-1} (1 µM), 23 s^{-1} and 37 s^{-1} (2 µM), respectively. Here, release rates, predicted by our model for a single release-ready vesicle (Fig. 5.4 a), were multiplied by a factor of 2, because the number of statistical release sites is approximately two in boutons of the crayfish neuromuscular junction (Dudel, 1981).

In the Calyx of Held, the volume-averaged presynaptic [Ca^{2+}] following an action potential peaks at ~0.5 µM and decays with a time constant of ~100 ms (Helmchen et al., 1997). If the rate of asynchronous release was solely dependent on the instantaneous residual [Ca^{2+}], the phasic release sensor model predicts a decay of asynchronous release approximately four-fold faster (Fig. 5.4 c,d). This is because at submicromolar level, the dependence of release rates on [Ca^{2+}] is determined by a power of >4. It is noteworthy that measurements of the time course of presynaptic [Ca^{2+}] and asynchronous release in cerebellar synapses revealed a similar acceleration of the decay of release rate compared to that of the [Ca^{2+}] (Atluri and Regehr, 1998). In the same study, however, it is also reported that delayed release rates cannot properly be described by a model that responds only to instantaneous [Ca^{2+}] levels, indicating that other processes may contribute to shaping the time course of delayed release.

Another phenomenon dependent on the volume-averaged [Ca^{2+}] following an action potential is the enhancement of release evoked by a second stimulus shortly after the first pulse. This paired-pulse facilitation (PPF, *see* section 1.1.3), often decays on the same time scale as the presynaptic [Ca^{2+}] and is also inhibited by the injection of

exogenous Ca^{2+} buffers, which speed the decay of residual [Ca^{2+}] (Kamiya and Zucker, 1994; Atluri and Regehr, 1996; Zucker, 1999). According to the residual Ca^{2+} hypothesis, facilitation may be generated by the linear summation of local [Ca^{2+}] transients and residual [Ca^{2+}] from previous Ca^{2+} influx (Katz and Miledi, 1968; Zucker, 1989). This, however, is in conflict with the common view that a low affinity Ca^{2+} sensor requires >100 µM of [Ca^{2+}], making it insensitive to the residual [Ca^{2+}] levels of at most a few micromolar. Alternatively, a second Ca^{2+} sensor with increased affinity and slow unbinding kinetics was suggested to explain the "memory effect" of the nerve terminal to previous stimulation (Zucker, 1996). Since the Calyx of Held exhibited a much higher affinity of the phasic release sensor compared to the previous estimates, the effect of residual [Ca^{2+}] on paired-pulse facilitation was analyzed (Fig. 5.4 b-d). Paired-pulse facilitation is often measured as the relative change of the EPSC amplitude of a second (test) pulse compared to the first (control) pulse. Here, residual [Ca^{2+}] and the local [Ca^{2+}] transient were summed and the resultant [Ca^{2+}] waveforms expected for different external [Ca^{2+}] levels were used to drive the Ca^{2+} sensor model (Fig. 5.4 b). Assuming a rapid refilling process of the vesicle pool with a time constant of 200 ms (Wu and Borst, 1999), PPF and partial vesicle pool depletion largely balanced each other at $[Ca^{2+}]_{ext}$ = 2 mM (Fig. 5.4 c). If the quantal content during the first pulse was reduced by lowering the external [Ca^{2+}], PPF, calculated as the ratio of the peak amplitude of the second EPSC over that of the first EPSC, had a value of 131% at an interpulse interval of 5 ms, and decayed with 86 ms, similar to the residual [Ca^{2+}]. The slower decay of facilitation compared to asynchronous release is not unexpected, because the second response in PPF profits from the residual [Ca^{2+}] two-fold; first, the Ca^{2+} sensor is pre-equilibrated to the increased basal [Ca^{2+}], and second, the summation of residual [Ca^{2+}] and the local [Ca^{2+}] transient results in a peak [Ca^{2+}] transient increased to ~105% compared to control. Both effects lead to a higher occupancy of the release-promoting state during the peak of the [Ca^{2+}] transient and hence an increased release probability.

The predicted low PPF ratio at a $[Ca^{2+}]_{ext}$ of 2 mM is consistent with the experimentally observed PPF at that $[Ca^{2+}]_{ext}$ in response to afferent stimulation at 200 Hz in the present study. In nine cells, in which the fraction of the vesicle pool released during the first EPSC was within ±3% relative to the mean value obtained in all synapses (21%, *see* section 4.2.3), the PPF ratio was 112% ± 5% (not shown). It should be noted that the MNTB giant synapse exhibits little facilitation compared to other synapses (Zucker, 1989; Atluri and Regehr, 1996; Dobrunz et al., 1997). It is likely that facilitation is also controlled by other mechanisms. Possible explanations are the local saturation of Ca^{2+} buffers by residual Ca^{2+} (Neher, 1998), differences in

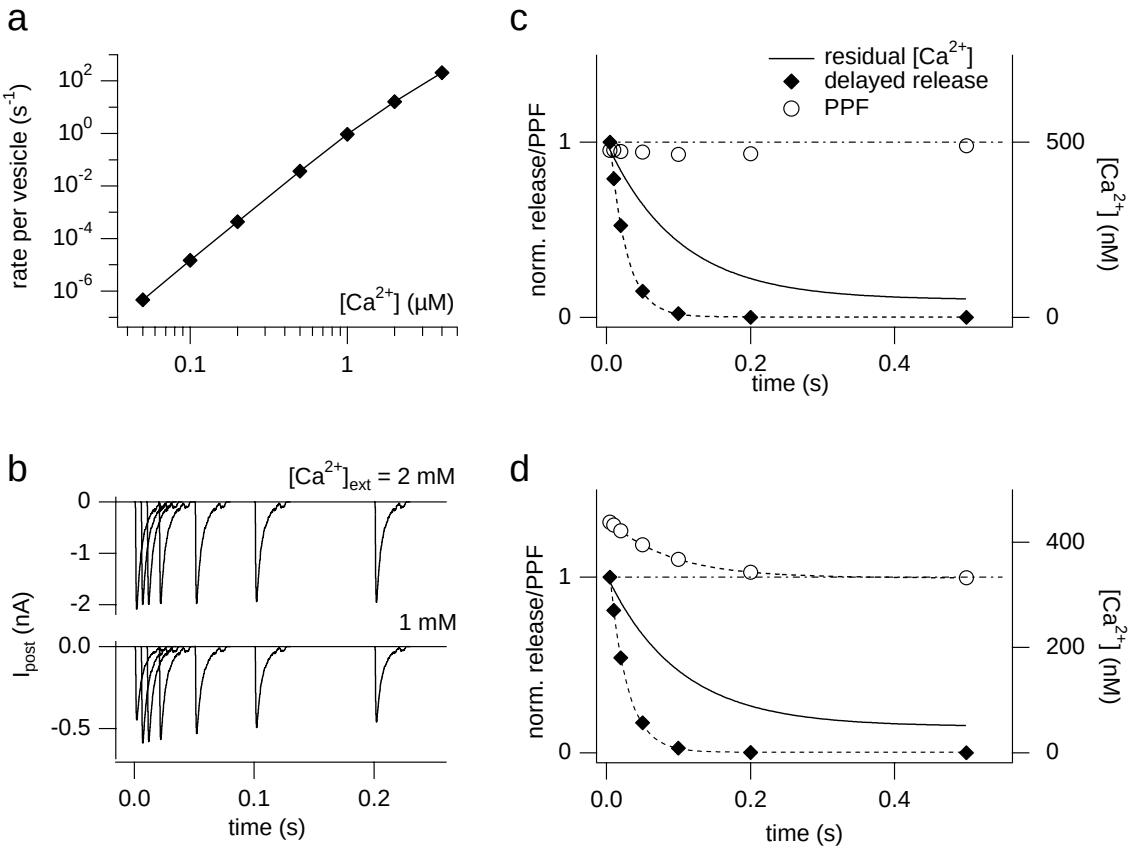

Fig. 5.4: Asynchronous release and facilitation predicted by the Ca^{2+} sensor model. (**a**) Model predictions of asynchronous release rates for low presynaptic $[Ca^{2+}]$. (**b**) Paired-pulse facilitation (PPF) predicted by the Ca^{2+} sensor model at $[Ca^{2+}]_{ext}$ = 2 mM (*upper panel*) and 1 mM (*lower panel*), caused by residual $[Ca^{2+}]$. PPF was calculated as the ratio of the peak amplitudes A_2 and A_1 of the test pulse and the first pulse, respectively. Test pulses for different PPF intervals are shown in the same panels. (**c**) Time course of delayed release, PPF and residual $[Ca^{2+}]$ for 2 mM external $[Ca^{2+}]$. Residual $[Ca^{2+}]$ decay constant is 100 ms, a fit to the delayed release time course yields an exponential decay time constant of 23 ms. Delayed release rates were normalized, the maximum corresponds to 0.03 s^{-1} per vesicle, 5 ms after the stimulation. No PPF is observed, because the predicted increase in release probability during the 2nd pulse is counteracted by partial pool depletion evoked by the 1st pulse. Pool recovery was modeled with a mono-exponential time course (τ = 200 ms) (Wu and Borst, 1999). (**d**) At 1 mM external $[Ca^{2+}]$, PPF is predicted due to residual $[Ca^{2+}]$ activating the Ca^{2+} sensor of phasic release. The local $[Ca^{2+}]$ transient and residual $[Ca^{2+}]$ were scaled by 0.64 compared to those at 2 mM, because of Ca^{2+} influx saturation (Schneggenburger et al., 1999). Delayed release decays with a τ of 25 ms, whereas PPF decays with a τ of 86 ms, similar to the residual $[Ca^{2+}]$ (τ = 100 ms). Peak delayed release is 0.005 s^{-1} per vesicle, 5 ms after stimulation.

the local uptake and extrusion of $[Ca^{2+}]$ near the release site, which should be sensitive to the surface-volume ratio of the synaptic terminal (Regehr and Atluri, 1995), stimulus-induced Ca^{2+} release from internal stores (Emptage et al., 2001), and

the involvement of a second, high affinity Ca^{2+} sensor that enhances release when activated by residual [Ca^{2+}] (*reviewed by* Zucker, 1999). The different time courses of asynchronous release and facilitation led to the interpretation that the two phenomena are controlled by different mechanisms (Zucker, 1996; Atluri and Regehr, 1998). Since the present Ca^{2+} sensor readily predicts a slower decay time for facilitation than for asynchronous release, different mechanisms are not necessarily required to explain the experimental data. Taken together, the present release model suggests that residual [Ca^{2+}] levels can influence the release probability during delayed release and facilitation at least in part by activating the Ca^{2+} sensor for phasic release.

5.3.2 Molecular candidates for the neuronal Ca^{2+} sensor

The key role of Ca^{2+} in triggering the release of neurotransmitter has long been established (Katz, 1969), but the molecular basis for the coupling of Ca^{2+} influx to secretion is still not resolved. Many Ca^{2+}-binding proteins have been found to exist in secretory systems. The present, quantitative description of presynaptic glutamate release imposes constraints on the Ca^{2+} binding properties of a putative Ca^{2+} sensor, which may be helpful for its molecular identification. Our Ca^{2+} sensor model indicates that several Ca^{2+} ions have to bind simultaneously to a sensor molecule in order to promote the fusion of a vesicle, as suggested previously (Dodge Jr. and Rahamimoff, 1967; *reviewed by* Wu and Saggau, 1997). The observed strong dependence of release rates on [Ca^{2+}] in the range from 1 to 10 µM suggests that the sensor can bind Ca^{2+} rapidly with a rate constant > 10^8 M^{-1} s^{-1}. Since the release rate-[Ca^{2+}] relation became much weaker for [Ca^{2+}] levels greater than 10 µM, the model predicted the experimental data best when the individual Ca^{2+} binding site had an affinity of ~10 µM. Furthermore, when the equilibrium occupancy of the activated state of the Ca^{2+} sensor is calculated, one obtains a saturation curve with a half-maximal concentration of 26 µM and a Hill coefficient of 1.7 (Fig. 5.5).

A prominent candidate as a neuronal Ca^{2+} sensor is synaptotagmin I, which is a membrane-integral protein of synaptic and large dense-cored vesicles (Südhof and Rizo, 1996; Burgoyne and Morgan, 1998). It can bind several Ca^{2+} ions via its two C2 domains and binds in a Ca^{2+}-dependent manner to phospholipids and syntaxin, a member of the SNARE complex, which is thought to be involved in vesicle docking and fusion (*see* section 1.2.2.1). Several studies have aimed to elucidate the role of synaptotagmin I in vesicle fusion by mutagenesis or deletion of expression

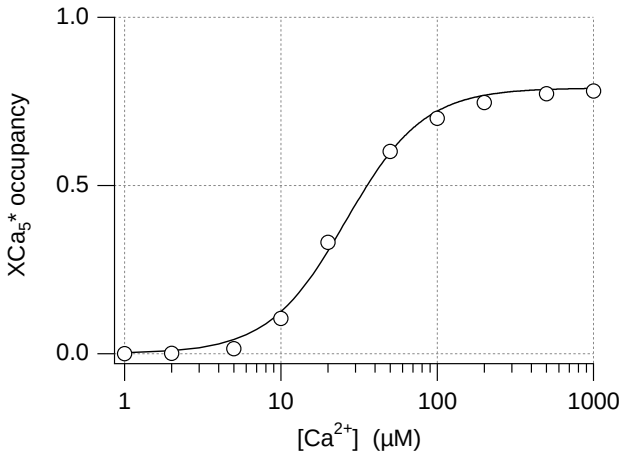

Fig. 5.5: Equilibrium occupancy of the activated Ca^{2+} sensor. The fraction of the Ca^{2+} sensors residing in the activated state XCa_5^*, when equilibrated with the indicated $[Ca^{2+}]$ levels (*open circles*). The solid line is a fit with the equation $0.79 \times [Ca^{2+}]^n / ([Ca^{2+}]^n + K^n)$, where n = 1.7 and K = 26 µM. The maximal occupancy of 0.79 of the activated sensor state is determined by the Ca^{2+} independent activation and inactivation constants γ = 30,000 s^{-1} and δ = 8,000 s^{-1}.

in *C. Elegans*, *Drosophila*, and mouse (Nonet et al., 1993; Broadie et al., 1994; Geppert et al., 1994; Fernández-Chacón et al., 2001). Since the applied manipulations all resulted in a dramatic impairment of synchronous transmitter release, synaptotagmin I is likely to play a significant role in the modulation of evoked transmitter release. Recent biochemical studies reported that the equilibrium binding of synaptotagmin to phospholipids is half-maximal at $[Ca^{2+}]$ levels of 10-75 µM (Davis et al., 1999; Fernández-Chacón et al., 2001). The activated state (XCa_5^*) of our Ca^{2+} sensor model could be interpreted as the state in which the sensor molecule forms a complex with another molecule to promote release. One possible reaction, besides a multitude of other schemes, is the binding of synaptotagmin to phospholipids, which exhibits a similar equilibrium Ca^{2+} dependence as the equilibrium occupancy of the XCa_5^* state (Fig. 5.5). The Ca^{2+} association rate constant was estimated to be larger than 10^8 M^{-1} s^{-1} (Davis et al., 1999). These properties are principally in line with the constraints suggested by our Ca^{2+} sensor model. The binding of synaptotagmin with syntaxin requires $[Ca^{2+}]$ levels of hundreds of micromolar (Südhof and Rizo, 1996), too high to be involved in the triggering of vesicle fusion in the Calyx of Held. Very recent evidence, however, suggests that the Ca^{2+} requirement of synaptotagmin-syntaxin binding may be considerably lower (Fernández-Chacón et al., 2001). In summary, synaptotagmin has many properties that make it a prominent candidate for a neuronal Ca^{2+} sensor of transmitter release. It

remains, however, unclear how synaptotagmin can mediate the fusion of the vesicle and terminal membrane.

Other molecules have been reported to modulate transmitter release at endocrine cells and nerve terminals, and have been investigated less extensively than synaptotagmin (*reviewed by* Burgoyne and Morgan, 1998). They bind Ca^{2+} via different binding domains such as C2 domains (Rabphilin 3A, protein kinase C, Rim, Munc-13, Doc 2), the EF-hand motif (Calcyclin, Calmodulin, Frequenin) or other binding domains (Annexin, CAPS, Scinderin). These proteins may also contribute to control of evoked transmitter release in a Ca^{2+}-dependent manner. It remains to be investigated at which stage of evoked exocytosis these proteins possibly exert a regulatory function.

5.3.3 Exocytosis in other synaptic and endocrine preparations

The fusion of intracellular vesicles with the plasma membrane and the subsequent release of their messenger molecules is the fundamental mechanism by which cells communicate with each other. Dependent on the cell function, the transmitters released can range from classical neurotransmitters, such as acetylcholine, glutamate, γ-amino butyric acid (GABA) or glycine, through peptides and monoamines, to globally-acting hormones. The speed of exocytosis varies over a wide range on the time scale from less than 1 millisecond to tens of seconds, demarcated by synaptic transmitter release at the faster, and slow hormone release at the lower end (*reviewed by* Kasai, 1999). On the other hand, a large body of evidence suggests that the fundamental mechanism which mediates biological membrane fusion is principally conserved among species and different cell types (Jahn and Südhof, 1999; Chen and Scheller, 2001).

In the MNTB giant synapse, relatively low $[Ca^{2+}]$ levels were sufficient to drive exocytosis. In the following, this high Ca^{2+} sensitivity will be compared to that of other fast synaptic and slower endocrine release systems.

5.3.3.1 *Other synaptic preparations*

- **Ribbon-type synapses**

Several neuronal cell types found in sensory pathways have specialized synaptic structures, in which vesicles are tethered to ribbon-like structures, which are thought to play a role in the rapid transport of reserve vesicles to the release site (von Gersdorff, 2001). In one type of ribbon-containing synapses, those of the retinal bipolar cells of the goldfish, the speed of exocytosis was observed by measuring the rate of capacitance change of the terminal membrane, which is related to glutamate

release from small vesicles. The Ca^{2+} dependence of capacitance change has been determined directly using flash photolysis, which revealed a Ca^{2+} sensitivity of release approximately one order of magnitude lower than glutamate release in the Calyx of Held (Heidelberger et al., 1994). In addition, this cell type was reported to sustain continuous exocytosis and compensatory endocytosis at $[Ca^{2+}]$ levels of around 1 µM, suggesting that at least a fraction of the releasable vesicles is more sensitive to small $[Ca^{2+}]$ elevations (Lagnado et al., 1996). Retinal bipolar cells do not fire fast sodium action potentials and appear to release transmitter on a time scale of ≥100 ms (Matthews, 1999), suggesting that they may possess release mechanisms somewhat different to those of fast releasing central synapses. This idea is supported by the special morphology of the release sites in ribbon-type synapses (von Gersdorff, 2001). The capacitance technique has also been applied to saccular and cochlear inner hair cells in frog and mouse, respectively, which are other members of the family of sensory cells containing ribbons (Parsons et al., 1994; Moser and Beutner, 2000). Very recently, the Ca^{2+} sensitivity of release from cochlear inner hair cells was shown to be relatively high compared to that in retinal bipolar cells in goldfish, indicating that the distinction between low and high Ca^{2+} sensitivity does not correlate with the presence or absence of ribbons in a presynaptic terminal (Beutner et al., 2001; Heidelberger et al., 1994).

- **Neuromuscular junction**

Because of their peripheral location in the central nervous system, neuromuscular junctions have become easily accessible and therefore very useful to study pre- and postsynaptic aspects of rapid chemical transmission with electrophysiological tools. Two types of neuromuscular junctions will be considered here, in which direct or indirect information on the Ca^{2+} sensitivity of the release process and the underlying $[Ca^{2+}]$ signal has been collected. Firstly, the current through presynaptic, Ca^{2+}-activated potassium channels ($I_{K\text{-}Ca}$) in cultured neuromuscular junctions from *Xenopus laevis* and *Rana pipiens* (frogs) was compared to the activation of simultaneously recorded EPSCs or EPSPs. In *Xenopus*, the local $[Ca^{2+}]$ transient was estimated to peak at 100 µM only within 10-20 nm from the Ca^{2+} channel (Yazejian et al., 2000). Based on high resolution measurements of Ca^{2+}-dependent fluorescence in the same preparation, it was estimated that in most regions of a Ca^{2+} entry site, $[Ca^{2+}]$ transients evoked by action potentials peak in the 10 to 20 micromolar range (DiGregorio et al., 1999). In a related preparation in *R. pipiens*, the slow Ca^{2+} chelator EGTA did not block the Ca^{2+}-activated potassium channels, consistent with the concept that they are co-localized closely enough with Ca^{2+} channels to 'sense' high $[Ca^{2+}]$ peak levels (Robitaille et al., 1993). In contrast, transmitter release was reduced in the presence of EGTA, indicating that most release sensors are further away from

the Ca^{2+} channels than Ca^{2+}-activated potassium channels. Apart from differences in the Ca^{2+} binding and activation properties, a likely explanation is that most Ca^{2+} sensors are located outside the narrow region where hundreds of micromolar [Ca^{2+}] can be expected.

In the neuromuscular junction of the crayfish opener muscle, the dependence of transmitter release on intracellular [Ca^{2+}] has been estimated more directly. It was found that asynchronous release is activated by [Ca^{2+}] levels of around 1 µM (*see* section 5.3.1.2) (Ravin et al., 1997). In addition, the same authors measured the sensitivity of synchronous release to volume-averaged [Ca^{2+}] (Ravin et al., 1999). They concluded from the relatively strong dependence of quantal content on residual [Ca^{2+}] that the Ca^{2+} affinity of the responsible release sensor is in the micromolar range.

- **Squid giant synapse**

At the giant synapse in the stellate ganglion of squid, the addition of the slow Ca^{2+} buffer EGTA, in contrast to the faster BAPTA, had little or no effect on evoked release (Adler et al., 1991). Because of this and because of the graded inhibition of release by other BAPTA derivatives with lower affinity, it was estimated that the [Ca^{2+}] signal triggering release exceeds 100 µM at this synapse. Furthermore, the Ca^{2+} domains generated during action potentials by Ca^{2+} influx through single Ca^{2+} channels probably do not overlap (*summarized by* Augustine et al., 1991). The concept of Ca^{2+} domains reaching high [Ca^{2+}] levels of several hundred micromolar was corroborated by the detection of highly localized fluorescence dots, using a very low affinity fluorescent protein (Llinás et al., 1992). Substantial release, however, can already be detected when [Ca^{2+}] is raised to 10 - 20 µM by flash photolysis (Hsu et al., 1996).

- **Small central synapses**

Rapid transmission at most neuronal synapses occurs at small structures of micrometer size, often located at large distances from the soma in the dendritic and axonal trees. Therefore, it is difficult to measure the Ca^{2+} dependence of transmitter release directly at the synaptic contacts. Most information on Ca^{2+} sensitivity has been gained by experiments of the ‘added Ca^{2+} buffer’ type. As used previously in squid and other more accessible preparations, slow and fast exogenous Ca^{2+} buffers such as EGTA and BAPTA are dialyzed into the presynaptic cell and tested for their capacity to inhibit action potential-evoked release. The inhibitory action of EGTA differed between various cortical and cerebellar preparations. In cortical neurons in layer 2/3 and 5 of young rats, EGTA blocked release by approximately 50% when present at

concentrations between 1 and 10 mM (Ohana and Sakmann, 1998; Rozov et al., 2001). This is quite similar to the Calyx of Held, where EGTA blocked release by ~40% and ~50%, when present at 1 and 10 mM, respectively (Borst and Sakmann, 1996). Also, in the granule cell to stellate cell synapse in the cerebellum of young rats, application of EGTA reduced phasic release to a similar degree (Chen and Regehr, 1999). In contrast, in cultured hippocampal neurons, EGTA abolished asynchronous release, but did not change the amount of action potential-evoked phasic release (Cummings et al., 1996).

When comparing the above compilation of synaptic properties with that of the MNTB giant synapse, the squid giant synapse appears most distinct from the MNTB giant synapse, because, at the MNTB giant synapse, lower [Ca^{2+}] levels were sufficient to explain action potential-evoked release. Furthermore, it was shown that Ca^{2+} domains of multiple channels overlap and cooperate in the triggering of a vesicle during action potential-evoked release (Borst and Sakmann, 1999b). Finally, the slow Ca^{2+} buffer EGTA considerably inhibited release in the MNTB giant synapse, suggesting that most of the vesicles are not in close vicinity with Ca^{2+} channels and therefore not in the range of the sharp peak of a Ca^{2+} domain (Borst and Sakmann, 1996). These findings do not contrast with the hypothesis that local [Ca^{2+}] levels may reach hundreds of micromolar, which is supported by many experimental and theoretical arguments (*reviewed by* Neher, 1998). The present results, however, strongly support the view that most of the vesicles do not experience these peak [Ca^{2+}] levels, because release would be expected to occur at higher rates if the majority of vesicles experienced Ca^{2+} domains peaking at [Ca^{2+}] levels larger 100 µM. Regarding the other synapses described above, release in the MNTB giant synapse exhibits many similarities with release detected at those synapses (apart from the vesicle pool of low Ca^{2+} sensitivity in ribbon-containing synapses).

When comparing aspects of neurotransmission, it should be considered that differences may not only be found between species and cell type, but also during development of the nervous system. Recordings from the Calyx of Held during different developmental stages (postnatal day 5 and 12-14) indicate that the size of the releasable vesicle pool increases, whereas the fraction released during an action potential is reduced (Taschenberger and von Gersdorff, 2000). One possible explanation is that the intrinsic Ca^{2+} sensitivity may decrease during maturation of the synapse. Nevertheless, based on the large body of evidence discussed above, it may be concluded that the observed high Ca^{2+} sensitivity of transmitter release is a property of many synapses and not a unique property of the Calyx of Held.

5.3.3.2 *Slow exocytosis in endocrine cells and neurons*

Many cell types are specialized to release hormonal substances (e.g. adrenaline, insuline) and neuromodulators (e.g. dopamine**,** neuropeptides), that act more globally and therefore do not need to be released with the precise timing of fast neurotransmitters. These cells typically store the transmitter substance in large, dense-cored vesicles (LDCVs) as opposed to the small, clear vesicles (SVs) found in presynaptic terminals, which contain fast neurotransmitters. Exocytosis in endocrine cell types has been measured in real time using for example the capacitance technique, amperometric detection of oxidizable messenger substances, and fluorometric measurements using membrane dyes to stain vesicles. Exocytosis in these systems is expected to be triggered by $[Ca^{2+}]$ levels in the range from one to several tens of micromolar, because transmitter release is strongly dependent on $[Ca^{2+}]$ in this range (Thomas et al., 1993; Chow et al., 1994; Heinemann et al., 1994; Proks et al., 1996) and, furthermore, because Ca^{2+} entry is less tightly regulated (Neher, 1998). In that respect, the Ca^{2+} sensitivity of exocytosis in slow release systems resembles that measured in the fast transmitting MNTB giant synapse. This may suggest that the release of SVs and LDCVs is triggered by similar Ca^{2+} binding mechanisms. A marked difference, however, lies in the different kinetics of release in these two systems. For example, in melanotrophs of the pituitary gland, the onset of release does not occur with delays shorter than a few milliseconds, even if $[Ca^{2+}]$ is raised to several hundreds of micromolar (Thomas et al., 1993). One explanation of this disparity may be a significant difference in the Ca^{2+} association rate of the LDCV Ca^{2+} and the SV Ca^{2+} sensor, implying two distinct release sensor molecules for the two types of release. Alternatively, the difference in release kinetics can be explained if processes downstream of Ca^{2+} binding to the sensor occur on different time scales for LDCV or SV release. Thus, the delay predicted by our Ca^{2+} sensor model can be drastically prolonged, if the Ca^{2+} independent activation and inactivation rate constants (γ, δ) are increased by two to three orders of magnitude, but the Ca^{2+} binding and unbinding rates are left unchanged. At present, it is difficult to distinguish between these two possibilities. However, experiments with toxins or genetic alterations that selectively affect the Ca^{2+} binding reaction or the fusion reaction are promising approaches to resolve this question (Xu et al., 1999; Fernández-Chacón et al., 2001).

5.4 Outlook

The quantitative description of the Ca^{2+} sensitivity of neuronal transmitter release presented here is only a first step towards understanding the molecular basis of excitation-secretion coupling in the Calyx of Held. The model of the Ca^{2+} sensor provides predictions for situations of repetitive synaptic activity, which should be compared to the results of future experiments. It would be interesting to investigate in a next step, to what extent asynchronous release and short term synaptic plasticity such as facilitation can be explained with the properties of the present Ca^{2+} sensor model. However, such experiments would be affected by the initially stated problem that the highly localized Ca^{2+} regulation during action potentials complicates measuring the relevant Ca^{2+} signal. An alternative approach would be to extend the uniform 'Ca^{2+} test functions' evoked by photolysis to more complex waveforms; this could be done, for example, by the combination of slow Ca^{2+} uncaging with a steady-state UV illumination and a brief UV pulse. Furthermore, by using appropriate combinations of a fast releasing Ca^{2+} cage and a slowly binding Ca^{2+} buffer in the presynaptic solution, one could possibly influence the decay rate of the presynaptic $[Ca^{2+}]$ after photolysis. This could be useful in determining the off-kinetics of the Ca^{2+} sensing and fusion mechanism.

The comparison with other synaptic preparations suggests that the Ca^{2+} dependence of release varies between synapses and species. Furthermore, it has been observed in the Calyx of Held that the release probability decreases during early development (Taschenberger and von Gersdorff, 2000). For a possible generalization of the present Ca^{2+} sensor model it would therefore be necessary to do similar experiments both in the Calyx of Held synapse at older stages and in other, for example cortical synapses. At present, the latter may be problematic because loading the presynaptic terminal is only possible by somatic whole-cell recordings. It is not unlikely that the initially nearly saturated Ca^{2+} cage would be unloaded during diffusional transport via the axon by Ca^{2+} extrusion mechanisms. Recent progress in patch-clamping small terminals in the hippocampus formation may greatly facilitate Ca^{2+} uncaging studies also in smaller synapses (Geiger and Jonas, 2000).

On the other hand, the Calyx of Held synapse provides unique opportunities to introduce reagents to a presynaptic terminal such as peptides and antibodies that can selectively interfere with a biochemical reaction and interrupt the vesicle cycle at a defined stage (Augustine et al., 1999). These approaches and other, genetic techniques designed to manipulate individual steps in the Ca^{2+} sensing and fusion reaction may give further insight into the interplay between synaptic proteins involved in rapid chemical transmission.

Finally, optical tools have now been developed to observe vesicle(s) traveling through different stages of the vesicle cycle, in part by staining with membrane specific dyes and in part by genetically engineered fluorescent vesicle proteins (Miesenböck et al., 1998; Richards et al., 2000; Zenisek et al., 2000, Sankaranarayanan and Ryan, 2001). If different types of synaptic proteins can be labeled by chromophores with distinct spectral signatures, it may be possible not only to localize these proteins in the synaptic terminal but also to obtain information about their relative position during different functional states of a vesicle. Aside from the readily used method of fluorescent resonance energy transfer, promising optical tools currently being developed are 4π- and θ-microscopy (Lindek et al., 1995) spectral precision distance microscopy (SPDM, Cremer et al., 1999), spatially modulated excitation fluorescence microscopy (SMI, Schneider et al., 1998) and stimulated emission depletion microscopy (STED, Klar et al., 2000). The most significant advances in elucidating the molecular basis of chemical transmission and exocytosis may be expected when optical and electrophysiological techniques are combined with biochemical and genetic approaches.

References

Adler, E. M., Augustine, G. J., Duffy, S. N., and Charlton, M. P. 1991. **Alien intracellular calcium chelators attenuate neurotransmitter release at the squid giant synapse**. *J. Neurosci.* 11:1496-1507.

Almers, W., and Tse, F. W. 1990. **Transmitter release from synapses: does a preassembled fusion pore initiate exocytosis?** *Neuron.* 4:813-818.

Angleson, J. K., and Betz, W. J. 1997. **Monitoring secretion in real time: capacitance, amperometry and fluorescence compared**. *Trends Neurosci.* 20:281-287.

Artalejo, C. R., Elhamdani, A., and Palfrey, H. C. 1996. **Calmodulin is the divalent cation receptor for rapid endocytosis, but not exocytosis, in adrenal chromaffin cells**. *Neuron.* 16:195-205.

Atkins, P. W. 1990. **Physikalische Chemie**. VCH Verlagsgesellschaft, Weinheim.

Atluri, P. P., and Regehr, W. G. 1996. **Determinants of the time course of facilitation at the granule cell to Purkinje cell synapse**. *J. Neurosci.* 16:5661-5671.

Atluri, P. P., and Regehr, W. G. 1998. **Delayed release of neurotransmitter from cerebellar granule cells**. *J. Neurosci.* 18:8214-8227.

Augustine, G. J., Adler, E. M., and Charlton, M. P. 1991. **The calcium signal for transmitter secretion from presynaptic nerve terminals**. *Annals of the New York Academy of Sciences.* 635:365-381.

Augustine, G. J., Burns, M. E., DeBello, W. M., Hilfiker, S., Morgan, J. R., Schweizer, F. E., Tokumaru, H., and Umayahara, K. 1999. **Proteins involved in synaptic vesicle trafficking**. *J. Physiol. (Lond.).* 520 Pt 1:33-41.

Ayer, R. K., Jr., and Zucker, R. S. 1999. **Magnesium binding to DM-nitrophen and its effect on the photorelease of calcium**. *Biophys. J.* 77:3384-3393.

Barnes-Davies, M., and Forsythe, I. D. 1995. **Pre- and postsynaptic glutamate receptors at a giant excitatory synapse in rat auditory brainstem slices**. *J. Physiol. (Lond.).* 488:387-406.

Barrett, E. F., and Stevens, C. F. 1972. **The kinetics of transmitter release at the frog neuromuscular junction**. *J. Physiol. (Lond.).* 227:691-708.

Baylor, S. M., and Hollingworth, S. 1998. **Model of sarcomeric Ca^{2+} movements, including ATP Ca^{2+} binding and diffusion, during activation of frog skeletal muscle**. *J. Gen. Physiol.* 112:297-316.

Bear, M. F. 1995. **Mechanism for a sliding synaptic modification threshold**. *Neuron.* 15:1-4.

Betz, W. J., Mao, F., and Bewick, G. S. 1992. **Activity-dependent fluorescent staining and destaining of living vertebrate motor nerve terminals**. *J. Neurosci.* 12:363-375.

Beutner, D., Voets, T., Neher, E., and Moser, T. 2001. **Calcium dependence of exocytosis and endocytosis at the cochlear inner hair cell afferent synapse**. *Neuron.* 29:681-690.

Blaustein, M. P. 1988. **Calcium transport and buffering in neurons**. *Trends Neurosci.* 11:438-443.

Bliss, T. V., and Collingridge, G. L. 1993. **A synaptic model of memory: long-term potentiation in the hippocampus**. *Nature.* 361:31-39.

Bollmann, J. H., Helmchen, F., Borst, J. G. G., and Sakmann, B. 1998. **Postsynaptic Ca^{2+} influx mediated by three different pathways during synaptic transmission at a calyx-type synapse**. *J. Neurosci.* 18:10409-10419.

Bollmann, J. H., Sakmann, B., and Borst, J. G. 2000. **Calcium sensitivity of glutamate release in a calyx-type terminal**. *Science.* 289:953-957.

Borst, J. G., and Sakmann, B. 1998. **Calcium current during a single action potential in a large presynaptic terminal of the rat brainstem**. *J. Physiol. (Lond.).* 506:143-157.

Borst, J. G. G., Helmchen, F., and Sakmann, B. 1995. **Pre- and postsynaptic whole-cell recordings in the medial nucleus of the trapezoid body of the rat**. *J. Physiol. (Lond.).* 489:825-840.

Borst, J. G. G., and Sakmann, B. 1996. **Calcium influx and transmitter release in a fast CNS synapse**. *Nature.* 383:431-434.

Borst, J. G. G., and Sakmann, B. 1999a. **Depletion of calcium in the synaptic cleft of a calyx-type synapse in the rat brainstem**. *J. Physiol. (Lond.).* 521:123-133.

Borst, J. G. G., and Sakmann, B. 1999b. **Effect of changes in action potential shape on calcium currents and transmitter release in a calyx-type synapse of the rat auditory brainstem**. *Philos. Trans. R. Soc. Lond. B. Biol. Sci.* 354:347-355.

Broadie, K., Bellen, H. J., DiAntonio, A., Littleton, J. T., and Schwarz, T. L. 1994. **Absence of synaptotagmin disrupts excitation-secretion coupling during synaptic transmission**. *Proc. Natl. Acad. Sci. USA.* 91:10727-10731.

Burgoyne, R. D., and Morgan, A. 1998. **Calcium sensors in regulated exocytosis**. *Cell Calcium.* 24:367-376.

Byrne, J. H., and Kandel, E. R. 1996. **Presynaptic facilitation revisited: state and time dependence**. *J. Neurosci.* 16:425-435.

Ceccarelli, B., Hurlbut, W. P., and Mauro, A. 1973. **Turnover of transmitter and synaptic vesicles at the frog neuromuscular junction**. *J. Cell Biol.* 57:499-524.

Chad, J. E., and Eckert, R. 1984. **Calcium domains associated with individual channels can account for anomalous voltage relations of Ca-dependent responses**. *Biophys. J.* 45:993-999.

Chen, C., and Regehr, W. G. 1999. **Contributions of residual calcium to fast synaptic transmission**. *J. Neurosci.* 19:6257-6266.

Chen, Y. A., and Scheller, R. H. 2001. **SNARE-mediated membrane fusion**. *Nat. Rev. Mol. Cell Biol.* 2:98-106.

Chow, R. H., Klingauf, J., and Neher, E. 1994. **Time course of Ca^{2+} concentration triggering exocytosis in neuroendocrine cells**. *Proc. Natl. Acad. Sci. USA.* 91:12765-12769.

Clapham, D. E. 1995. **Calcium signaling**. *Cell.* 80:259-268.

Clements, J. D., Lester, R. A., Tong, G., Jahr, C. E., and Westbrook, G. L. 1992. **The time course of glutamate in the synaptic cleft**. *Science.* 258:1498-1501.

Cochilla, A. J., Angleson, J. K., and Betz, W. J. 1999. **Monitoring secretory membrane with FM1-43 fluorescence**. *Annu. Rev. Neurosci.* 22:1-10.

Crank, J. 1975. **The Mathematics of Diffusion**. University Press, Oxford.

Cremer, C., Edelmann, P., Bornfleth, H., Kreth, G., Muench, H., Luz, H., and Hausmann, M. 1999. **Principles of Spectral Precision Distance Confocal Microscopy for the Analysis of Molecular Nuclear Structure**. *In* Handbook of Computer Vision and Applications. B. Jähne, H. Haußecker, and P. Geißler, editors. Academic Press, San Diego. 839-857.

Cummings, D. D., Wilcox, K. S., and Dichter, M. A. 1996. **Calcium-dependent paired-pulse facilitation of miniature EPSC frequency accompanies depression of EPSCs at hippocampal synapses in culture**. *J. Neurosci.* 16:5312-5323.

Datyner, N. B., and Gage, P. W. 1980. **Phasic secretion of acetylcholine at a mammalian neuromuscular junction**. *J. Physiol. (Lond.).* 303:299-314.

Davis, A. F., Bai, J., Fasshauer, D., Wolowick, M. J., Lewis, J. L., and Chapman, E. R. 1999. **Kinetics of synaptotagmin responses to Ca^{2+} and assembly with the core SNARE complex onto membranes**. *Neuron.* 24:363-376.

Delaney, K. R., and Zucker, R. S. 1990. **Calcium released by photolysis of DM-nitrophen stimulates transmitter release at squid giant synapse**. *J. Physiol. (Lond.).* 426:473-498.

del Castillo, J., and Katz, B. 1954. **Quantal components of the end-plate potential**. *J. Physiol. (Lond.).* 124:560-573.

Diamond, J. S., and Jahr, C. E. 1997. **Transporters buffer synaptically released glutamate on a submillisecond time scale**. *J. Neurosci.* 17:4672-4687.

DiGregorio, D. A., Peskoff, A., and Vergara, J. L. 1999. **Measurement of action potential-induced presynaptic calcium domains at a cultured neuromuscular junction**. *J. Neurosci.* 19:7846-7859.

Dobrunz, L. E., Huang, E. P., and Stevens, C. F. 1997. **Very short-term plasticity in hippocampal synapses**. *Proc. Natl. Acad. Sci. USA.* 94:14843-14847.

Dodge Jr., F. A., and Rahamimoff, R. 1967. **Co-operative action of calcium ions in transmitter release at the neuromuscular junction**. *J. Physiol. (Lond.).* 193:419-432.

Dodt, H., Eder, M., Frick, A., and Zieglgansberger, W. 1999. **Precisely localized LTD in the neocortex revealed by infrared-guided laser stimulation**. *Science.* 286:110-113.

Draguhn, A., Traub, R. D., Schmitz, D., and Jefferys, J. G. 1998. **Electrical coupling underlies high-frequency oscillations in the hippocampus in vitro**. *Nature.* 394:189-192.

Dudel, J. 1981. **The effect of reduced calcium on quantal unit current and release at the crayfish neuromuscular junction**. *Pflügers Archiv.* 391:35-40.

Dudel, J., Menzel, R., and Schmidt, R. F. 1996. **Neurowissenschaft**. Springer Verlag, Berlin.

Edwards, F. A., Konnerth, A., Sakmann, B., and Takahashi, T. 1989. **A thin slice preparation for patch clamp recordings from neurones of the mammalian central nervous system**. *Pflügers Archiv.* 414:600-612.

Eigen, M., and Wilkins, R. G. 1965. **The kinetics and mechanism of formation of metal complexes**. *In* Mechanisms of Inorganic reactions. Advanced Chemistry series.

Ellis-Davies, G. C., and Kaplan, J. H. 1994. **Nitrophenyl-EGTA, a photolabile chelator that selectively binds Ca^{2+} with high affinity and releases it rapidly upon photolysis**. *Proc. Natl. Acad. Sci. USA.* 91:187-191.

Ellis-Davies, G. C., Kaplan, J. H., and Barsotti, R. J. 1996. **Laser photolysis of caged calcium: rates of calcium release by nitrophenyl-EGTA and DM-nitrophen**. *Biophys. J.* 70:1006-1016.

Emptage, N. J., Reid, C. A., and Fine, A. 2001. **Calcium stores in hippocampal synaptic boutons mediate short-term plasticity, store-operated Ca^{2+} entry, and spontaneous transmitter release**. *Neuron.* 29:197-208.

Escobar, A. L., Velez, P., Kim, A. M., Cifuentes, F., Fill, M., and Vergara, J. L. 1997. **Kinetic properties of DM-nitrophen and calcium indicators: rapid transient response to flash photolysis**. *Pflügers Archiv.* 434:615-631.

Fabiato, A., and Fabiato, F. 1979. **Calculator programs for computing the composition of the solutions containing multiple metals and ligands used for experiments in skinned muscle cells**. *J. Physiol. (Lond.).* 75:463-505.

Fatt, P., and Katz, B. 1952. **Spontaneous subthreshold potentials at motor nerve endings**. *J. Physiol. (Lond.).* 117:109-128.

Fernández-Chacón, R., Konigstorfer, A., Gerber, S. H., Garcia, J., Matos, M. F., Stevens, C. F., Brose, N., Rizo, J., Rosenmund, C., and Südhof, T. C. 2001. **Synaptotagmin I functions as a calcium regulator of release probability**. *Nature.* 410:41-49.

Fesce, R., Grohovaz, F., Valtorta, F., and Meldolesi, J. 1994. **Neurotransmitter release: Fusion or 'Kiss-and-Run'?** *Trends Cell. Biol.* 4:1-4.

Forsythe, I. D. 1994. **Direct patch recording from identified presynaptic terminals mediating glutamatergic EPSCs in the rat CNS, in vitro**. *J. Physiol. (Lond.).* 479:381-387.

Geiger, J. R., and Jonas, P. 2000. **Dynamic control of presynaptic Ca^{2+} inflow by fast-inactivating K^+ channels in hippocampal mossy fiber boutons**. *Neuron.* 28:927-939.

Geppert, M., Goda, Y., Hammer, R. E., Li, C., Rosahl, T. W., Stevens, C. F., and Südhof, T. C. 1994. **Synaptotagmin I: a major Ca^{2+} sensor for transmitter release at a central synapse**. *Cell.* 79:717-727.

Goda, Y., and Stevens, C. F. 1994. **Two components of transmitter release at a central synapse**. *Proc. Natl. Acad. Sci. USA.* 91:12942-12946.

Golovina, V. A., and Blaustein, M. P. 1997. **Spatially and functionally distinct Ca2+ stores in sarcoplasmic and endoplasmic reticulum**. *Science.* 275:1643-1648.

Greengard, P., Valtorta, F., Czernik, A. J., and Benfenati, F. 1993. **Synaptic vesicle phosphoproteins and regulation of synaptic function**. *Science.* 259:780-785.

Hamill, O. P., Marty, A., Neher, E., Sakmann, B., and Sigworth, F. J. 1981. **Improved patch-clamp techniques for high-resolution current recording from cells and cell-free membrane patches**. *Pflügers Archiv.* 391:85-100.

Harlow, M. L., Ress, D., Stoschek, A., Marshall, R. M., and McMahan, U. J. 2001. **The architecture of active zone material at the frog's neuromuscular junction**. *Nature.* 409:479-484.

Hartmann, J., and Lindau, M. 1995. **A novel Ca^{2+}-dependent step in exocytosis subsequent to vesicle fusion**. *FEBS Lett.* 363:217-220.

Hazard, A. L., Kohout, S. C., Stricker, N. L., Putkey, J. A., and Falke, J. J. 1998. **The kinetic cycle of cardiac troponin C: calcium binding and dissociation at site II trigger slow conformational rearrangements**. *Protein Sci.* 7:2451-2459.

Hebb, D. O. 1949. **The Organization of Behaviour**. Wiley, New York.

Heidelberger, R. 1998. **Adenosine triphosphate and the late steps in calcium-dependent exocytosis at a ribbon synapse**. *J. Gen. Physiol.* 111:225-241.

Heidelberger, R., Heinemann, C., Neher, E., and Matthews, G. 1994. **Calcium dependence of the rate of exocytosis in a synaptic terminal**. *Nature.* 371:513-515.

Heinemann, C., Chow, R. H., Neher, E., and Zucker, R. S. 1994. **Kinetics of the secretory response in bovine chromaffin cells following flash photolysis of caged Ca^{2+}**. *Biophys. J.* 67:2546-2557.

Helfert, R. H., and Aschoff, A. 1997. **Superior olivary complex and nuclei of the lateral lemniscus**. *In* The central auditory system. G. Ehret and R. Romand, editors. Oxford University Press, New York. 193-258.

Helmchen, F., Borst, J. G. G., and Sakmann, B. 1997. **Calcium dynamics associated with a single action potential in a CNS presynaptic terminal**. *Biophys. J.* 72:1458-1471.

Henkel, A. W., and Almers, W. 1996. **Fast steps in exocytosis and endocytosis studied by capacitance measurements in endocrine cells**. *Curr. Opin. Neurobiol.* 6:350-357.

Herrington, J., Newton, K. R., and Bookman, R. J. 1995. **PULSE CONTROL V4.7: IGOR XOPs for Patch Clamp Data Acquisition and Capacitance Measurements**. University of Miami, Miami, FL.

Heuser, J. E., and Reese, T. S. 1973. **Evidence for recycling of synaptic vesicle membrane during transmitter release at the frog neuromuscular junction**. *J. Cell Biol.* 57:315-344.

Hodgkin, A. L., Huxley, A. F., and Katz, B. 1952. **Measurement of current-voltage relations in the membrane of the giant axon of Loligo**. *J. Physiol. (Lond.)*. 116:424-448.

Hsu, S.-F., Augustine, G. J., and Jackson, M. B. 1996. **Adaptation of Ca^{2+}-triggered exocytosis in presynaptic terminals**. *Neuron.* 17:501-512.

Jahn, R., and Sudhof, T. C. 1999. **Membrane fusion and exocytosis**. *Annu. Rev. Biochem.* 68:863-911.

Jonas, P., and Spruston, N. 1994. **Mechanisms shaping glutamate-mediated excitatory postsynaptic currents in the CNS**. *Curr. Opin. Neurobiol.* 4:366-372.

Kamiya, H., and Zucker, R. S. 1994. **Residual Ca^{2+} and short-term synaptic plasticity**. *Nature.* 371:603-606.

Kaplan, J. H., and Ellis-Davies, G. C. 1988. **Photolabile chelators for the rapid photorelease of divalent cations**. *Proc. Natl. Acad. Sci. USA.* 85:6571-6575.

Kaplan, J. H., and Somlyo, A. P. 1989. **Flash photolysis of caged compounds: new tools for cellular physiology**. *Trends Neurosci.* 12:54-59.

Kasai, H. 1999. **Comparative biology of Ca^{2+}-dependent exocytosis: implications of kinetic diversity for secretory function**. *Trends Neurosci.* 22:88-93.

Katz, B. 1969. **The release of neural transmitter substances**. Thomas, C., Springfield, IL.

Katz, B., and Miledi, R. 1968. **The role of calcium in neuromuscular facilitation**. *J. Physiol. (Lond.).* 195:481-492.

Klar, T. A., Jakobs, S., Dyba, M., Egner, A., and Hell, S. W. 2000. **Fluorescence microscopy with diffraction resolution barrier broken by stimulated emission**. *Proc. Natl. Acad. Sci. USA.* 97:8206-8210.

Klingauf, J., Kavalali, E. T., and Tsien, R. W. 1998. **Kinetics and regulation of fast endocytosis at hippocampal synapses**. *Nature.* 394:581-585.

Koester, H. J., and Sakmann, B. 2000. **Calcium dynamics associated with action potentials in single nerve terminals of pyramidal cells in layer 2/3 of the young rat neocortex**. *J. Physiol. (Lond.).* 529 Pt 3:625-646.

Lagnado, L., Gomis, A., and Job, C. 1996. **Continuous vesicle cycling in the synaptic terminal of retinal bipolar cells**. *Neuron.* 17:957-967.

Larkum, M. E., Zhu, J. J., and Sakmann, B. 1999. **A new cellular mechanism for coupling inputs arriving at different cortical layers**. *Nature.* 398:338-341.

Lindau, M., and Neher, E. 1988. **Patch-clamp techniques for time-resolved capacitance measurements in single cells**. *Pflügers Archiv.* 411:137-146.

Lindek, S., Stelzer, E. H. K., and Hell, S. W. 1995. **Two new high-resolution confocal fluorescence microscopies (4Pi, Theta) with one- and two-photon excitation**. *In* Handbook of Biological Confocal Microscopy. J. B. Pawley, editor. Plenum Press, New York. 417-430.

Llinás, R., Sugimori, M., and Silver, R. B. 1992. **Microdomains of high calcium concentration in a presynaptic terminal**. *Science.* 256:677-679.

London, R. E., Rhee, C. K., Murphy, E., Gabel, S., and Levy, L. A. 1994. **NMR-sensitive fluorinated and fluorescent intracellular calcium ion indicators with high dissociation constants**. *Am. J. Physiol.* 266:C1313-1322.

Magee, J. C., and Johnston, D. 1997. **A synaptically controlled, associative signal for Hebbian plasticity in hippocampal neurons**. *Science.* 275:209-213.

Markram, H., Lubke, J., Frotscher, M., and Sakmann, B. 1997. **Regulation of synaptic efficacy by coincidence of postsynaptic APs and EPSPs**. *Science.* 275:213-215.

Matthews, G. 1999. **Synaptic mechanisms of bipolar cell terminals**. *Vision Res.* 39:2469-2476.

Mayer, M. L., Westbrook, G. L., and Guthrie, P. B. 1984. **Voltage-dependent block by Mg^{2+} of NMDA responses in spinal cord neurones**. *Nature.* 309:261-263.

McCray, J. A., Fidler-Lim, N., Ellis-Davies, G. C., and Kaplan, J. H. 1992. **Rate of release of Ca^{2+} following laser photolysis of the DM-nitrophen- Ca^{2+} complex**. *Biochemistry.* 31:8856-8861.

Meinrenken, C. J., and Sakmann, B. 2001. **Heterogeneous release probability of a fast central synapse is mediated by a non-uniform topography of its release sites**. *in preparation*.

Miesenböck, G., Deangelis, D. A., and Rothman, J. E. 1998. **Visualizing secretion and synaptic transmission with pH-sensitive Green Fluorescent Proteins**. *Nature.* 394:192-195.

Moser, T., and Beutner, D. 2000. **Kinetics of exocytosis and endocytosis at the cochlear inner hair cell afferent synapse of the mouse**. *Proc. Natl. Acad. Sci. USA.* 97:883-888.

Murthy, V. N., Sejnowski, T. J., and Stevens, C. F. 1997. **Heterogeneous release properties of visualized individual hippocampal synapses**. *Neuron.* 18:599-612.

Nakanishi, S. 1994. **Metabotropic glutamate receptors: synaptic transmission, modulation, and plasticity**. *Neuron.* 13:1031-1037.

Naraghi, M. 1997. **T-jump study of calcium binding kinetics of calcium chelators**. *Cell Calcium.* 22:255-268.

Naraghi, M., and Neher, E. 1997. **Linearized buffered Ca^{2+} diffusion in microdomains and its implications for calculation of [Ca^{2+}] at the mouth of a calcium channel**. *J. Neurosci.* 17:6961-6973.

Neher, E. 1986. **Concentration profiles of intracellular calcium in the presence of a diffusible chelator**. *Exp. Brain Res.* 14:80-96.

Neher, E. 1998. **Vesicle pools and Ca^{2+} microdomains: new tools for understanding their roles in neurotransmitter release**. *Neuron.* 20:389-399.

Neher, E., and Sakaba, T. 2001. **Combining deconvolution and noise analysis for the estimation of transmitter release rates at the calyx of held**. *J. Neurosci.* 21:444-461.

Neher, E., and Sakmann, B. 1976. **Single-channel currents recorded from membrane of denervated frog muscle fibres**. *Nature.* 260:799-802.

Neher, E., and Zucker, R. S. 1993. **Multiple calcium-dependent processes related to secretion in bovine chromaffin cells**. *Neuron.* 10:21-30.

Nonet, M. L., Grundahl, K., Meyer, B. J., and Rand, J. B. 1993. **Synaptic function is impaired but not eliminated in C. elegans mutants lacking synaptotagmin**. *Cell.* 73:1291-1305.

Nowak, L., Bregestovski, P., Ascher, P., Herbet, A., and Prochiantz, A. 1984. **Magnesium gates glutamate-activated channels in mouse central neurones**. *Nature.* 307:462-465.

Oberhauser, A. F., Robinson, I. M., and Fernandez, J. M. 1996. **Simultaneous capacitance and amperometric measurements of exocytosis: a comparison**. *Biophys. J.* 71:1131-1139.

Ohana, O., and Sakmann, B. 1998. **Transmitter release modulation in nerve terminals of rat neocortical pyramidal cells by intracellular calcium buffers**. *J. Physiol. (Lond.).* 513:135-148.

Otis, T., Zhang, S., and Trussell, L. O. 1996a. **Direct measurement of AMPA receptor desensitization induced by glutamatergic synaptic transmission**. *J. Neurosci.* 16:7496-7504.

Otis, T. S., Wu, Y. C., and Trussell, L. O. 1996b. **Delayed clearance of transmitter and the role of glutamate transporters at synapses with multiple release sites**. *J. Neurosci.* 16:1634-1644.

Pape, P. C., Jong, D.-S., and Chandler, W. K. 1995. **Calcium release and its voltage dependence in frog cut muscle fibers equilibrated with 20 mM EGTA**. *J. Gen. Physiol.* 106:259-336.

Parnas, H., Dudel, J., and Parnas, I. 1986. **Neurotransmitter release and its facilitation in crayfish. VII. Another voltage dependent process beside Ca entry controls the time course of phasic release**. *Pflügers Archiv.* 406:121-130.

Parsons, T. D., Lenzi, D., Almers, W., and Roberts, W. M. 1994. **Calcium-triggered exocytosis and endocytosis in an isolated presynaptic cell: capacitance measurements in saccular hair cells**. *Neuron.* 13:875-883.

Pearse, B. M., Smith, C. J., and Owen, D. J. 2000. **Clathrin coat construction in endocytosis**. *Curr. Opin. Struct. Biol.* 10:220-228.

Peters, C., Bayer, M. J., Buhler, S., Andersen, J. S., Mann, M., and Mayer, A. 2001. **Trans-complex formation by proteolipid channels in the terminal phase of membrane fusion**. *Nature.* 409:581-588.

Pieribone, V. A., Shupliakov, O., Brodin, L., Hilfiker-Rothenfluh, S., Czernik, A. J., and Greengard, P. 1995. **Distinct pools of synaptic vesicles in neurotransmitter release**. *Nature.* 375:493-497.

Proks, P., Eliasson, L., Ammala, C., Rorsman, P., and Ashcroft, F. M. 1996. **Ca^{2+}- and GTP-dependent exocytosis in mouse pancreatic beta-cells involves both common and distinct steps**. *J. Physiol. (Lond.).* 496:255-264.

Pyle, J. L., Kavalali, E. T., Piedras-Renteria, E. S., and Tsien, R. W. 2000. **Rapid reuse of readily releasable pool vesicles at hippocampal synapses**. *Neuron.* 28:221-231.

Rapp, G. 1998. **Flash lamp-based irradiation of caged compounds**. *Methods Enzymol.* 291:202-222.

Ravin, R., Parnas, H., Spira, M. E., Volfovsky, N., and Parnas, I. 1999. **Simultaneous measurement of evoked release and $[Ca^{2+}]_i$ in a crayfish release bouton reveals high affinity of release to Ca^{2+}**. *J. Neurophysiol.* 81:634-642.

Ravin, R., Spira, M. E., Parnas, H., and Parnas, I. 1997. **Simultaneous measurement of intracellular Ca^{2+} and asynchronous transmitter release from the same crayfish bouton**. *J. Physiol. (Lond.).* 501:251-262.

Regehr, W. G. 1997. **Interplay between sodium and calcium dynamics in granule cell presynaptic terminals**. *Biophys. J.* 73:2476-2488.

Regehr, W. G., and Atluri, P. P. 1995. **Calcium transients in cerebellar granule cell presynaptic terminals**. *Biophys. J.* 68:2156-2170.

Rhode, W. S., and Smith, P. H. 1986. **Encoding timing and intensity in the ventral cochlear nucleus of the cat**. *J Neurophysiol.* 56:261-286.

Richards, D. A., Guatimosim, C., and Betz, W. J. 2000. **Two endocytic recycling routes selectively fill two vesicle pools in frog motor nerve terminals**. *Neuron.* 27:551-559.

Roberts, W. M. 1994. **Localization of calcium signals by a mobile calcium buffer in frog saccular hair cells**. *J. Neurosci.* 14:3246-3262.

Robitaille, R., Garcia, M. L., Kaczorowski, G. J., and Charlton, M. P. 1993. **Functional colocalization of calcium and calcium-gated potassium channels in control of transmitter release**. *Neuron.* 11:645-655.

Rozov, A., Burnashev, N., Sakmann, B., and Neher, E. 2001. **Transmitter release modulation by intracellular Ca^{2+} buffers in facilitating and depressing nerve terminals of pyramidal cells in layer 2/3 of the rat neocortex indicates a target cell-specific difference in presynaptic calcium dynamics**. *J. Physiol. (Lond.).* 531:807-826.

Ryan, T. A., Reuter, H., and Smith, S. J. 1997. **Optical detection of a quantal presynaptic membrane turnover**. *Nature.* 388:478-482.

Sakaba, T., and Neher, E. 2001a. **Preferential potentiation of fast-releasing synaptic vesicles by cAMP at the calyx of Held**. *Proc. Natl. Acad. Sci. USA.* 98:331-336.

Sakaba, T., and Neher, E. 2001b. **Quantitative relationship between transmitter release and calcium current at the calyx of held synapse**. *J. Neurosci.* 21:462-476.

Sankaranarayanan, S., and Ryan, T. A. 2001. **Calcium accelerates endocytosis of vSNAREs at hippocampal synapses**. *Nat. Neurosci.* 4:129-136.

Sätzler, K. 2000. **3D Rekonstruktion von elektronenmikroskopischen Serienschnitten**. PhD. Ruprecht-Karls-Universität, Heidelberg.

Schneggenburger, R., Meyer, A. C., and Neher, E. 1999. **Released fraction and total size of a pool of immediately available transmitter quanta at a calyx synapse**. *Neuron.* 23:399-409.

Schneggenburger, R., and Neher, E. 2000. **Intracellular calcium dependence of transmitter release rates at a fast central synapse**. *Nature.* 406:889-893.

Schneider, B., Bradl, J., Kirsten, I., Hausmann, M., and Cremer, C. 1998. **High precision localization of fluorescent targets in the nanometer range by spatially modulated excitation fluorescence microscopy**. *In* Fluorescence Microscopy and Fluorescent Probes. j. Slavik, editor. Plenum Press. 71-76.

Sherman, A. J., Shrier, A., and Cooper, E. 1999. **Series resistance compensation for whole-cell patch-clamp studies using a membrane state estimator**. *Biophys. J.* 77:2590-2601.

Silver, R. A., Cull-Candy, S. G., and Takahashi, T. 1996. **Non-NMDA glutamate receptor occupancy and open probability at a rat cerebellar synapse with single and multiple release sites**. *J. Physiol. (Lond.).* 494:231-250.

Simon, S. M., and Llinás, R. R. 1985. **Compartmentalization of the submembrane calcium activity during calcium influx and its significance in transmitter release**. *Biophys. J.* 48:485-498.

Smith, G. D. 1996. **Analytical steady-state solution to the rapid buffering approximation near an open Ca^{2+} channel**. *Biophys. J.* 71:3064-3072.

Spirou, G. A., Brownell, W. E., and Zidanic, M. 1990. **Recordings from cat trapezoid body and HRP labeling of globular bushy cell axons**. *J. Neurophysiol.* 63:1169-1190.

Stevens, C. F., and Williams, J. H. 2000. **"Kiss and run" exocytosis at hippocampal synapses**. *Proc. Natl. Acad. Sci. USA.* 97:12828-12833.

Stuart, G. J., and Sakmann, B. 1994. **Active propagation of somatic action potentials into neocortical pyramidal cell dendrites**. *Nature.* 367:69-72.

Südhof, T. C. 1995. **The synaptic vesicle cycle: a cascade of protein-protein interactions**. *Nature.* 375:645-653.

Südhof, T. C., and Rizo, J. 1996. **Synaptotagmins: C_2-domain proteins that regulate membrane traffic**. *Neuron.* 17:379-388.

Sun, J.-Y., and Wu, L.-G. 2001. **Fast kinetics of exocytosis revealed by simultaneous measurements of presynaptic capacitance and postsynaptic currents at a central synapse**. *Neuron.* 30:171-182.

Tang, C. M., Margulis, M., Shi, Q. Y., and Fielding, A. 1994. **Saturation of postsynaptic glutamate receptors after quantal release of transmitter**. *Neuron.* 13:1385-1393.

Tang, Y. P., Shimizu, E., Dube, G. R., Rampon, C., Kerchner, G. A., Zhuo, M., Liu, G., and Tsien, J. Z. 1999. **Genetic enhancement of learning and memory in mice**. *Nature.* 401:63-69.

Taschenberger, H., and von Gersdorff, H. 2000. **Fine-tuning an auditory synapse for speed and fidelity: developmental changes in presynaptic waveform, EPSC kinetics, and synaptic plasticity**. *J. Neurosci.* 20:9162-9173.

Thomas, P., Wong, J. G., Lee, A. K., and Almers, W. 1993. **A low affinity Ca^{2+} receptor controls the final steps in peptide secretion from pituitary melanotrophs**. *Neuron.* 11:93-104.

Tietze, U., and Schenck, C. 1978. **Halbleiter-Schaltungstechnik**. Springer-Verlag, Berlin.

Tong, G., and Jahr, C. E. 1994. **Multivesicular release from excitatory synapses of cultured hippocampal neurons**. *Neuron.* 12:51-59.

Traynelis, S. F. 1998. **Software-based correction of single compartment series resistance errors**. *J. Neurosci. Methods.* 86:25-34.

Trussell, L. O., and Fischbach, G. D. 1989. **Glutamate receptor desensitization and its role in synaptic transmission**. *Neuron.* 3:209-218.

Trussell, L. O., Zhang, S., and Raman, I. M. 1993. **Desensitization of AMPA receptors upon multiquantal neurotransmitter release**. *Neuron.* 10:1185-1196.

Van der Kloot, W. 1988. **Estimating the timing of quantal releases during end-plate currents at the frog neuromuscular junction**. *J. Physiol. (Lond.).* 402:595-603.

von Gersdorff, H. 2001. **Synaptic ribbons: versatile signal transducers**. *Neuron.* 29:7-10.

von Gersdorff, H., and Matthews, G. 1994. **Inhibition of endocytosis by elevated internal calcium in a synaptic terminal**. *Nature.* 370:652-655.

von Gersdorff, H., Sakaba, T., Berglund, K., and Tachibana, M. 1998. **Submillisecond kinetics of glutamate release from a sensory synapse**. *Neuron.* 21:1177-1188.

von Gersdorff, H., Schneggenburger, R., Weis, S., and Neher, E. 1997. **Presynaptic depression at a calyx synapse: the small contribution of metabotropic glutamate receptors**. *J. Neurosci.* 17:8137-8146.

Wightman, R. M., Jankowski, J. A., Kennedy, R. T., Kawagoe, K. T., Schroeder, T. J., Leszczyszyn, D. J., Near, J. A., Diliberto, E. J., Jr., and Viveros, O. H. 1991. **Temporally resolved catecholamine spikes correspond to single vesicle release from individual chromaffin cells**. *Proc. Natl. Acad. Sci. USA.* 88:10754-10758.

Wilkinson, R. S., and Cole, J. C. 2001. **Resolving the Heuser-Ceccarelli debate**. *Trends Neurosci.* 24:195-197.

Wu, L.-G., and Borst, J. G. G. 1999. **The reduced release probability of releasable vesicles during recovery from short-term synaptic depression**. *Neuron.* 23:821-832.

Wu, L.-G., and Saggau, P. 1997. **Presynaptic inhibition of elicited neurotransmitter release**. *Trends Neurosci.* 20:204-212.

Xu, T., Naraghi, M., Kang, H., and Neher, E. 1997. **Kinetic studies of Ca^{2+} binding and Ca^{2+} clearance in the cytosol of adrenal chromaffin cells**. *Biophys. J.* 73:532-545.

Xu, T., Rammner, B., Margittai, M., Artalejo, A. R., Neher, E., and Jahn, R. 1999. **Inhibition of SNARE complex assembly differentially affects kinetic components of exocytosis**. *Cell.* 99:713-722.

Xu-Friedman, M. A., and Regehr, W. G. 1999. **Presynaptic strontium dynamics and synaptic transmission**. *Biophys. J.* 76:2029-2042.

Yamada, K. A., and Tang, C.-M. 1993. **Benzothiadiazides inhibit rapid glutamate receptor desensitization and enhance glutamatergic synaptic currents**. *J. Neurosci.* 13:3904-3915.

Yamada, W. M., and Zucker, R. S. 1992. **Time course of transmitter release calculated from simulations of a calcium diffusion model**. *Biophys. J.* 61:671-682.

Yazejian, B., Sun, X. P., and Grinnell, A. D. 2000. **Tracking presynaptic Ca^{2+} dynamics during neurotransmitter release with Ca^{2+}-activated K^+ channels**. *Nat. Neurosci.* 3:566-571.

Young, M. 2000. **Optics and Lasers**. Springer-Verlag, Berlin.

Yuste, R., and Denk, W. 1995. **Dendritic spines as basic functional units of neuronal integration**. *Nature.* 375:682-684.

Zamanillo, D., Sprengel, R., Hvalby, O., Jensen, V., Burnashev, N., Rozov, A., Kaiser, K. M., Koster, H. J., Borchardt, T., Worley, P., Lubke, J., Frotscher, M., Kelly, P. H., Sommer, B., Andersen, P., Seeburg, P. H., and Sakmann, B. 1999. **Importance of AMPA receptors for hippocampal synaptic plasticity but not for spatial learning**. *Science.* 284:1805-1811.

Zenisek, D., Steyer, J. A., and Almers, W. 2000. **Transport, capture and exocytosis of single synaptic vesicles at active zones**. *Nature.* 406:849-854.

Zucker, R. S. 1989. **Short-term synaptic plasticity**. *Annu. Rev. Neurosci.* 12:13-31.

Zucker, R. S. 1992. **Effects of photolabile calcium chelators on fluorescent calcium indicators**. *Cell Calcium.* 13:29-40.

Zucker, R. S. 1993. **The calcium concentration clamp: spikes and reversible pulses using the photolabile chelator DM-nitrophen**. *Cell Calcium.* 14:87-100.

Zucker, R. S. 1996. **Exocytosis: a molecular and physiological perspective**. *Neuron.* 17:1049-1055.

Zucker, R. S. 1999. **Calcium- and activity-dependent synaptic plasticity**. *Curr. Opin. Neurobiol.* 9:305-313.

Danksagung

Herrn Prof. Sakmann verdanke ich die Möglichkeit, die vorliegende Arbeit in der Abteilung Zellphysiologie am Max-Planck-Institut für medizinische Forschung realisieren zu können. Von ihm erhielt ich zahlreiche Anregungen zum wissenschaftlichen Denken sowie viele Beispiele der Freude am Forschen. Ich danke ihm für die Unterstützung, Motivation und Unabhängigkeit, die ich in dieser Zeit genießen durfte.

Sehr gedankt sei Gerard Borst für die Aufgabenstellung, die der vorliegenden Arbeit zu Grunde liegt. Zahlreiche Anregungen, konkrete Verbesserungsvorschläge und konstruktive Kritik haben das Gelingen dieser Arbeit erst möglich gemacht. Ferner danke ich ihm für die kritische Durchsicht des Manuskripts. Beste Groeten!

Ich danke Herrn Prof. Cremer für die freundliche Betreuung seitens der Fakultät für Physik und Astronomie und für das Interesse, das er meiner Arbeit entgegengebracht hat.

Herrn Prof. Neher danke ich für hilfreiche Anregungen und lehrreiche Diskussionen über zelluläre Ca^{2+}-Signale und Mechanismen der synaptischen Übertragung.

Herzlich danken möchte ich Christoph Meinrenken, Helmut Köster, Ora Ohana und Arnd Roth für zahlreiche Diskussionen und Anregungen, die zur Erweiterung der vorliegenden Arbeit und meines Verständnisses derselben beigetragen haben. Arnd Roth danke ich für die Hilfe beim Einstieg in 'Mathematica' und für Programmstrukturen, die in das Ca^{2+}-Sensormodell eingegangen sind.

Ich danke Hans Engler, Valentin Nägerl und David DiGregorio für Anregungen zur Messung schneller Fluoreszenzsignale und Diskussionen über Ca^{2+}-Dynamik.

Marlies Kaiser möchte ich für die labortechnische Unterstützung danken, aber auch für ihre Übersicht. Klaus Bauer danke ich für Rat und Unterstützung bei Computerfragen. Ramon Granadillo sei gedankt für die bibliographische Hilfe. Frau Dücker, Frau Spiegel und Frau Matthies danke ich für organisatorische Hilfe.

Für die große Hilfe beim Lösen technischer Probleme sei besonders Herrn Schmidt und Rolf Rödel sowie Herrn Maier und Herrn Müller aus der Feinmechanik-Werkstatt und dem Elektroniklabor gedankt.

Suzanne Farley, Troy Margrie, Nathan Urban und Jack Waters haben freundlicherweise die Durchsicht jeweils verschiedener Teile des Manuskripts auf sprachliche Richtigkeit hin übernommen. Dafür sei ihnen gedankt.

Allen Mitarbeitern in der Abteilung danke ich für anregende Gespräche und Diskussionen, für die Bereitschaft, ihr Wissen zu teilen, und für die freundliche (nicht nur Arbeits-)Atmosphäre.

Bernd, Carsten, Nils und Rüdiger danke ich für freundschaftliche Unterstützung in den vergangenen Jahren.

Ich danke Josephine, u.a. für ihre Neugier und ihren Esprit.

Besonderer Dank gilt meinen Eltern für ihre Unterstützung und ihr Vertrauen.